UC Berkeley
UC Berkeley Electronic Theses and Dissertations

Title
Tail-Augmented Self-Righting and Turning of a Dynamic Legged Millirobot

Permalink
https://escholarship.org/uc/item/5sq4r40k

Author
Casarez, Carlos Sebastian

Publication Date
2018

Peer reviewed|Thesis/dissertation

eScholarship.org Powered by the California Digital Library
University of California

Tail-Augmented Self-Righting and Turning of a Dynamic Legged Millirobot

by

Carlos Sebastian Casarez

A dissertation submitted in partial satisfaction of the

requirements for the degree of

Doctor of Philosophy

in

Engineering – Mechanical Engineering

in the

Graduate Division

of the

University of California, Berkeley

Committee in charge:

Professor Ronald S. Fearing, Co-chair
Professor Oliver M. O'Reilly, Co-chair
Professor Mark W. Mueller
Professor Robert J. Full

Summer 2018

Tail-Augmented Self-Righting and Turning of a Dynamic Legged Millirobot

Copyright 2018
by
Carlos Sebastian Casarez

Abstract

Tail-Augmented Self-Righting and Turning of a Dynamic Legged Millirobot

by

Carlos Sebastian Casarez

Doctor of Philosophy in Engineering – Mechanical Engineering

University of California, Berkeley

Professor Ronald S. Fearing, Co-chair

Professor Oliver M. O'Reilly, Co-chair

Small-scale folded legged robots have demonstrated exceptional mobility in laboratory environments. However, in real-world applications, these robots require added robustness. This thesis introduces LoadRoACH, a 54.8 g palm-sized folded legged robot that carries a protective shell and an active tail (totaling 27.2 g). These added components enable LoadRoACH to survive high drops, rapidly self-right, and turn with enhanced maneuverability. First, a thermoforming manufacturing process is developed for integrated shells that protect folded legged robots from impacts and water/granular media. Next, design details are presented for LoadRoACH that enable dynamic running while carrying significantly larger payloads than previous folded legged robots. Then, dynamic self-righting with tail/terrain pushing is analyzed and tested using a modified VelociRoACH robot, which is a precursor to LoadRoACH. VelociRoACH can dynamically self-right on low-friction, high-friction, and granular terrain in as little time as 256 ms. In an autonomous self-righting experiment, VelociRoACH detects inversion and rapidly self-rights while walking over an obstacle with multiple step drops. Finally, two novel turning strategies that leverage tail/terrain contact during forward running are analyzed and implemented using LoadRoACH. The first strategy drags the tail against high-friction terrain to produce sustained turns with comparable maneuverability to differential drive turns. The second strategy impacts the tail against low-friction, high-friction, and granular terrain to produce rapid point turns with a heading change of up to 90° in 0.8 s. In an aggressive corner steering maneuver, a combination of tail drag and tail impact turning on a carpet surface enable the robot to advance further along the desired heading when compared to differential drive turning.

To my lovely wife Bethany

And to Mom and Dad for their love and support from across the country

Contents

Contents **ii**

List of Figures **v**

List of Tables **viii**

1 Introduction **1**
1.1 Outline . . . 2
1.2 Contributions . . . 3

2 Background **5**
2.1 Previous Capabilities of Folded Robots . . . 5
2.2 Protective Structures of Robots . . . 9
2.3 Self-Righting Strategies of Animals and Robots . . . 11
2.4 Turning Strategies of Legged Animals and Robots . . . 15
2.5 Locomotion with Terrain Contact of a Tail . . . 19

3 Exoskeletal Shells for Folded Millirobots **21**
3.1 Thermoforming for Integrated Robot Shells . . . 21
3.2 Flexible Shell for Environmental Protection . . . 23
3.2.1 Design . . . 23
3.2.2 Manufacturing . . . 24
3.2.3 Characterization . . . 24
3.3 Structural Shell for Impact Protection . . . 26
3.3.1 Design . . . 27
3.3.2 Manufacturing . . . 29
3.3.3 Assembly and Integration With Flexible Shell . . . 32
3.3.4 Characterization . . . 32
3.4 Performance Trade-Offs of Exoskeletal Shell . . . 33

4 Design of a High-Payload Folded Legged Millirobot **34**
4.1 Limitations of Prior Folded Legged Millirobots . . . 34
4.1.1 Scaling of Flexure Peel Loading . . . 35

4.1.2 Scaling of Flexure Mechanism Load Transmission 36
4.1.3 Scaling of Terminal Velocity Impact Force 37
4.1.4 Payload Carrying Comparison of Folded Legged Robots 40
4.2 Design Details of LoadRoACH 41
4.2.1 Initial Design for Self-Righting 42
4.2.2 Folded Robot Material and Process Improvements 43
4.2.3 Leg Transmission Module Design 49
4.2.4 Shell Design 50
4.2.5 Tail Module Design 51
4.2.6 Multi-Material Leg Design 52
4.2.7 Power, Communication, and Control Electronics 54
4.2.8 Low-Level Leg and Tail Control 54
4.3 Running with High Payload 59

5 Tailed Self-Righting with Terrain Contact 60
5.1 Terrestrial Tailed Self-Righting Analysis 60
5.1.1 Model Parameters 60
5.1.2 Newtonian Dynamics Formulation 60
5.1.3 Quasi-Static Design Considerations 65
5.1.4 Dynamic Righting Time Predictions 66
5.2 Terrestrial Tailed Self-Righting Experiments 68
5.2.1 Open-Loop Self-Righting Performance Tests 68
5.2.2 Autonomous Self-Righting Reflex on Unstructured Terrain 72
5.3 Self-Righting Performance Comparison 74

6 Tailed Turning with Terrain Contact 76
6.1 Tail Drag Turning Analysis 76
6.1.1 Formulation of Steady-State Turning Equilibria 76
6.1.2 Steady-State Turning Performance 80
6.2 Tail Impact Turning Analysis 82
6.2.1 Impulse-Momentum Applied to Maneuver 82
6.2.2 Experimental Analysis 83
6.3 Comparative Turning Experiments 83
6.3.1 Open-Loop Turning Performance 83
6.3.2 Closed-Loop Steering 89

7 Conclusions 94
7.1 Discussion 94
7.2 Future Directions 96
7.2.1 Shell Manufacturing 96
7.2.2 Tailed Self-Righting with Terrain Contact 96
7.2.3 Tailed Turning with Terrain Contact 97

7.2.4 Deploying LoadRoACH in Search and Rescue Applications 97

A LoadRoACH Transmission Details **99**

Bibliography **102**

List of Figures

2.1 Cross-section view of the process flow for Smart Composite Microstructures (SCM) manufacturing. 6
2.2 Pictures of robots capable of self-righting. 12

3.1 Schematic of the thermoforming process. 22
3.2 Top: molds constructed using (a) clay modeling, (b) slice forms, (c) 3D printing, and (d) laser cutting. Bottom: exoskeletal shells made from these molds by thermoforming using (a,b) 750 μm polystyrene, (c) 250 μm polycarbonate, and (d) 50 μm polyethylene. 23
3.3 Sealed flexible shell manufacturing process. 25
3.4 Leg mounts that clip through the flexible shell. 26
3.5 (a) Side view and (b) underside view of solid model renderings of VelociRoACH assembled in the structural shell. The structural shell clears the leg motion of the robot. 27
3.6 (a) Top view and (b) side section view of the thermoformed structural top shell over a 3D printed mold. (i) 3D printed PLA plastic ellipsoidal form with a 3 mm hull and 30% fill. (ii) Outwardly protruding lip at the base. 30
3.7 Bottom structural shell manufacturing process. 31
3.8 Images of the bottom shell mold, thermoformed bottom structural shell, and finished bottom shell after release cuts. 32
3.9 Assembly process for adding exoskeletal shell to the robot. 33

4.1 LoadRoACH with single degree of freedom tail for tail-assisted self-righting and dynamic turning. 42
4.2 VelociRoACH with protective shell and tail for dynamic self-righting. 43
4.3 Side-view schematic of adhesive strength tests of flexural material (cyan) bonded to structural material (grey) using a thermally activated adhesive (red). 44
4.4 Annotated images of LoadRoACH with improved flexure technology and transmission. 48
4.5 Conceptual sagittal plane drawing of robot leg positions as a function of crank angle φ. 50
4.6 Tail module for LoadRoACH. 51

4.7 Multi-material leg manufacturing process flow. 53
4.8 PID leg controller block diagram. 56
4.9 PID tail controller block diagram. 58
4.10 Average forward velocity for alternating tripod gaits with varying stride frequency on different surfaces. 59

5.1 (a) Back view diagram showing mass and geometry parameters of a VelociRoACH robot with shell and active tail. (b) Overlaid video frames of VelociRoACH swinging its tail. 61
5.2 Roll plane diagrams of the forces and moments that act on a tailed robot during a dynamic self-righting maneuver. 62
5.3 Tail torque required for quasi-static self-righting of a robot with an elliptical shell on flat terrain. 65
5.4 Tail-assisted self-righting dynamic simulation results on flat ground with Coulomb friction at the shell and tail contacts. 67
5.5 Comparison of the time to perform a 180° roll reorientation of a robot body for (a) aerial self-righting with an inertial tail of varying mass and length and (b) terrestrial righting with a low-mass tail of varying length on surfaces with varying coefficient of friction $\mu = \mu_b = \mu_t$. 68
5.6 High-speed camera frame sequence of a VelociRoACH robot with shell and active tail performing a dynamic self-righting maneuver on wood. 69
5.7 Robot telemetry for ten repeated trials of open-loop tail-assisted self-righting on wood. 70
5.8 Surfaces used in open-loop tail-assisted self-righting experiments. 71
5.9 High-speed camera frame sequence of a VelociRoACH robot with shell and active tail failing to self-right after a single tail swing on loose rocks. 72
5.10 Autonomous tailed self-righting reflex control block diagram. 72
5.11 VelociRoACH robot telemetry for an autonomous tailed self-righting reflex while walking down a step obstacle with a stride frequency of 4 Hz. 73
5.12 Camera frame sequence of an autonomous tailed self-righting reflex after VelociRoACH walks off an obstacle with steep drop-offs. 74

6.1 Free body diagrams of (a) overhead, (b) back, and (c) side views of a legged robot performing a sustained turn while dragging a tail. 78
6.2 Geometric parameters for tail drag turning with (a) side, (b) overhead motor frame, and (c) back motor frame views. 79
6.3 Steady-state turning equilibria from the dynamic analysis of dragging a tail with frictional contact. 81
6.4 Free body diagram of a transient tail impact maneuver causing 3D rigid body rotation of a legged robot. 82
6.5 Motion tracking and robot telemetry data during a transient tail impact turn on carpet. 84

6.6 Video frame sequences of LoadRoACH implementing different turn methods while running on carpet. 85
6.7 Forward speed v_{Gx} (measured from motion tracking) and angular rate $\dot{\psi}$ (measured from the robot's gyroscope) of LoadRoACH turning with sustained control effort through (a) differential drive and (b) tail drag turning methods. 86
6.8 Experimental center of mass trajectories (measured from motion tracking) for sustained turns with the highest average maneuverability. 87
6.9 (a) Turn time Δt and turn angle $\Delta\psi$ over a single impact of the tail against the ground with varying tail rotation rate. The stars mark the highest performance turn with regard to average angular velocity over the turn event $\Delta\psi/\Delta t$. (b) Center of mass trajectories for select tail impact turn trials with the highest performance. 88
6.10 Closed-loop steering block diagram for differential drive leg control. 90
6.11 Closed-loop steering block diagram for tail drag control. 91
6.12 Closed-loop steering block diagram for tail impact control. 91
6.13 Closed-loop corner turn steering trajectories using gyroscope feedback. 92
6.14 Closed-loop steering performance for an aggressive corner turn maneuver. 93

A.1 Engineering drawing of the LoadRoACH transmission module with annotations of components from the bill of materials. Dimension units are millimeters. . . . 101

List of Tables

2.1 Comparison of folded legged robots 9

4.1 Comparison of folded legged robots with payload 41
4.2 Peel strength of *GBC Octiva* hot-mount adhesive bonds [40] 44
4.3 Cantilever delamination strength of SCM composites 45
4.4 Properties of candidate SCM structural materials 46
4.5 Leg controller parameters 57
4.6 Tail controller parameters 58

5.1 VelociRoACH with shell and tail parameters 61
5.2 Tail-assisted righting performance on various surfaces 71
5.3 Comparison of robots with tail-like appendages that can rapidly reorient 75

6.1 LoadRoACH with shell and tail parameters. 77
6.2 Maximum sustained turning maneuverability 87
6.3 Angular velocities achieved with tail impact turning 89

A.1 Bill of materials for LoadRoACH transmission module 100

Acknowledgments

The research presented in this dissertation was supported by a National Science Foundation Graduate Research Fellowship (NSF GRFP), the NSF Integrative Graduate Education and Research Traineeship (IGERT) grant no. DGE-0903711 (PI Robert Full, Co-PIs Mimi Koehl, Ronald Fearing, and Robert Dudley) facilitated by the Center for interdisciplinary Biological-inspiration in Education fand Research (CiBER), the NSF National Robotics Initiative (NRI) grant no. CMMI-1427096 (PI Ronald Fearing, Co-PI Avideh Zakhor), and the United States Army Research Laboratory (ARL) under the Micro Autonomous Science and Technology Collaborative Technology Alliance (MAST CTA, PI Ronald Fearing).

Thanks to my advisor Ron Fearing for his steadfast support and weekly discussions over the past five years driving my exploration of the field of experimental robotics. Thanks to Professor Full and others involved in coordinating the CiBER-IGERT traineeship for supporting my development early on as a graduate student through enlightening seminars, engaging coursework, and valuable opportunities to share my research with an interdisciplinary community. Thank you also to all the members of my dissertation committee for providing helpful comments and feedback over the course of preparing this dissertation. Thanks to the members of the Biomimetic Millisystems Lab, especially my cubicle mates over the years Jessica Lee, Ethan Schaler, Cameron Rose, Justin Yim, and Jane Esterline for sharing the excitement and frustrations of robotics research, as well as the welcome distractions from it. Thanks to Tom Libby, Mark Plecnik, Evan Chang-Siu, and TaeWon Seo for their valuable mentorship and advice that guided me through to the finish of my dissertation.

Special thanks to my good friend John Welsh, my wife Bethany, and my family who kept me sane and grounded throughout my graduate school journey.

Chapter 1

Introduction

Small, rapidly-manufactured legged robots have the potential to expand mobile sensing capabilities in real-world environments. Diverse terrain with variable friction, inclination, roughness scale, and sparsity of footholds can be overcome with legged mobility, as demonstrated extensively by larger scale robots such as RHex [115], BigDog [113], HyQ2Max [119], ANYmal [60], and the MIT Cheetah 2 [107]. However, it is costly to deploy complex individual robots with many actuators to gather information in applications such as inspecting engineered structures, monitoring natural environments, and searching disaster sites after nuclear meltdowns, earthquakes, or hurricanes. An application of particular interest for the robot system developed in this dissertation is searching for and rescuing survivors in a collapsed building after an earthquake.

An alternative paradigm in search and rescue robotics is to utilize small underactuated robots with legged mobility over terrain and through tight spaces, at the cost of reduced payload capacity. These simpler, lower-computation units are inexpensive and expendable, allowing them to be deployed in large numbers to distribute search efforts. Moreover, losing many robots in the rubble of a collapsed building is an acceptable loss so long as a portion of the robots can collect information to help localize survivors. This class of robots is enabled by the scaled Smart Composite Microstructures (SCM) process [56], which allows for rigid links with mechanical pins to be replaced by selectively placed flexures in a lightweight composite material structure. In addition, joints driven by individual motors that are coordinated to follow a running gait can be replaced by passive kinematic linkages driven by fewer motors, which achieve similar leg motions with greater mass-specific power density. Legged SCM robots such as CLASH with a single motor [7] [8] and VelociRoACH with two motors [43] have demonstrated high mobility in vertical climbing and fast forward running tasks, respectively. However, these robots have only been tested in laboratory environments, and are susceptible to failure modes such as inversion, damage from impacts, and drive mechanism failure after extended running. To reach the ultimate goal of reliably deploying small scale legged SCM robots in search and rescue environments, this class of robots needs to be able to carry additional payloads that improve their field robustness.

Because legged SCM robots are driven by mechanically tuned compliant mechanisms, any

significant payload compared to the baseline mass poses a considerable negative impact on legged locomotion performance. Therefore, lightweight and minimal components are required for protecting these robots against impacts and for self-righting after inversion. In addition, achieving multiple functions with a single component is highly beneficial. In particular, this dissertation focuses on expanding the capability of legged SCM robots by leveraging multi-functional payloads including thermoformed shells and tail-like appendages driven by a single motor. Thermoformed shells provide protection from impacts and water/granular media, and also have a streamlined shape to promote self-righting and traversal of cluttered terrain. A single motor driving a lightweight tail enables dynamic self-righting and turning maneuvers that leverage tail/terrain contact. At the millirobot scale (with masses of 15–45 grams and length scales of 10–20 centimeters), existing legged SCM robots are not able to support the additional payload of shell and tail components (totaling 20–30 grams) while maintaining dynamic locomotion performance. To address this limitation, this dissertation introduces LoadRoACH (high payLoad Robotic Autonomous Crawling Hexapod), a novel legged SCM robot design with increased load-carrying capacity.

1.1 Outline

Chapter 2 provides background establishing the context of this dissertation in the field of robotics. First, the breadth of literature regarding the manufacturing and mobility of folded robots is reviewed. Then, various approaches are described for protecting swimming, jumping, wheeled, and legged robots against impacts and water. Lastly, the locomotion capabilities of robots and animals that provide biological inspiration for roboticists are covered in detail, including passive and actuated self-righting strategies, legged and tailed turning strategies, and locomotion maneuvers that involve terrain contact of a tail appendage.

Chapter 3 presents a multi-material thermoforming manufacturing process for creating exoskeletal shells for folded millirobots.[1] Flexible shells protect electronics and gearboxes against water and granular media. Structural shells protect against impact damage from high falls. These two shell components are integrated into VelociRoACH, a prior folded legged millirobot, and the shell's protection capabilities and impact on legged locomotion are characterized.

Chapter 4 details the design of LoadRoACH, a novel high-payload folded legged millirobot. This chapter also presents design details for shell and tail components added to LoadRoACH, multi-material legs that provide high traction on smooth and rough terrain, and electronics and controllers used to implement leg and tail motions in experiments.

Chapter 5 reports analytical and experimental results for self-righting by pushing against

[1]This chapter is adapted from content published in "Integrated manufacture of exoskeletons and sensing structures for folded millirobots," *J. Mech. Robot.* 2015 [40]. C. Casarez was the primary author of this content, with D. Haldane, C. Li, and A. Pullin providing supporting roles.

terrain with a single degree of freedom tail.[2] Quasi-static analysis gives tail motor torque requirements for self-righting a robot with a shell and tail based on shell geometry, tail geometry, and friction properties of the contacts. Dynamic simulation of tailed righting predicts the time required to self-right on terrain with varying friction. Experiments using a modified VelociRoACH robot with shell and tail demonstrate rapid and repeatable self-righting on low-friction, high-friction, and granular terrain using an open-loop overhead tail swing. In an autonomous self-righting reflex behavior, periodic overhead swinging of the tail upon detecting inversion enables the robot to maintain leg contact with the ground as it walks on and tumbles over terrain with multiple step drops.

Chapter 6 develops two novel legged turning methods that leverage terrain contact with an active tail and provides experimental results for tailed turning using LoadRoACH.[3] Steady-state turning equilibrium analysis of a dynamic model with simplified robot drive and a compliant tail dragging against the ground predicts the achievable forward speed and angular rate of turns sustained by the friction moment of a dragging tail. Experimental analysis of the tail impacting the ground at high velocity during forward locomotion reveals a rapid rigid body reorientation effect resulting in a net yaw heading change. In open-loop performance characterization experiments, the achievable forward and angular velocities of tail drag turning and tail impact turning on various surfaces are determined and compared to differential drive turning. Finally, tailed and differential drive turning strategies are implemented in closed-loop steering controllers to track an aggressive corner steering trajectory while LoadRoACH runs with maximum forward velocity.

Chapter 7 summarizes the contributions of this dissertation and provides insight into future directions that can be pursued to build on the presented results.

1.2 Contributions

This work makes the following contributions:

- **Manufacturing process for protective shells compatible with folded legged millirobots**—The developed thermoforming process leverages rapid prototyping for inexpensive production and quick design iteration of shell molds. Thermoformed materials of varying elastic modulus and thickness can be used to create shells tailored to impact absorption or lightweight, flexible protection against water and granular media. The shells are easily integrated into the chassis of folded legged robots with minimal restriction to driving mechanisms. The process is scalable in both size and number of robots, subject to the size of thermoforming tooling.

[2]This chapter was originally published as part of "Dynamic terrestrial self-righting with a minimal tail," *IEEE/RSJ Int. Conf. on Intelligent Robots and Systems* 2017 [17].

[3]This chapter to appear as "Steering of an underactuated legged robot through terrain contact with an active tail," *IEEE/RSJ Int. Conf. on Intelligent Robots and Systems* 2018 [18].

- **LoadRoACH - A high-payload folded legged millirobot**—High payload capacity is enabled by material and process improvements to folded robot fabrication and a novel leg transmission module with increased mechanical robustness. LoadRoACH can carry 50% of its body mass in payload while dynamically running at comparable velocities to the prior state of the art folded legged millirobot running at an intermediate stride frequency. Compared to previous folded legged robots with added payload, LoadRoACH carries 82% of the previous robots' baseline mass in payload and can run 29% faster than a robot that carries a similar magnitude payload.

- **Dynamic tailed self-righting with terrain contact**—Using a single tail actuator with simple control to push against terrain, the capability to self-right is added to palm-sized folded legged millirobots, which were previously rendered immobile after inversion. The self-righting method is reliable across tested terrain types and can be implemented with tails that are 1% of the robot mass, compared to massive tails for inertial righting that provide similar righting times with masses of 2–10% of the robot mass. The tested robot platform can self-right faster than previous robots with inertial or ground-pushing tails.

- **Development of two novel tailed turning strategies with terrain contact**–Tail drag turning and tail impact turning enhance the maneuverability of legged robots. Tail drag turning produces higher forward speeds and comparable turning maneuverability to differential drive turns. Tail impact turning produces rapid reorientation about a point. These two tailed turning methods are combined while following a high-speed running gait for improved steering performance compared to differential drive with continuously varying leg velocities.

Chapter 2

Background

2.1 Previous Capabilities of Folded Robots

With the advent of the Smart Composite Microstructures (SCM) manufacturing process, folded robotic structures can be produced cheaply and repeatably. From planar laser micromachining of sheet material, kinematic joints and assembly features can be integrated into a robot part set to provide complex motion for legged and aerial robots, but without traditional mechanical components such as pins, rigid links, fasteners, and bearings. A process flow overview of SCM manufacturing is shown in Figure 2.1.

SCM originated as an alternative to standard silicon micro-electromechanical systems (MEMS) processes for creating robots with overall dimensions of a few centimeters, with joint and feature dimensions on the order of hundreds of microns. The first major success of this process came from design iterations by Wood et al. of the Micromechanical Flying Insect [139], in which the multi-material composite laminate process was first presented. The original process combines structural layers of a carbon fiber composite with a flexural middle layer of polyimide film. In a 2D layout, the carbon fiber layup (pre-impregnated with epoxy) are first machined using a ultraviolet (UV) laser to cut away material where flexural joints are to be placed. Then, the sheets are aligned and a layer of flexible polyimide is bonded between them. Finally, a UV laser is used again to cut out robot pieces with integrated joints, which can either be used for fold-up assembly or as kinematic linkages for robot appendages. Design considerations were developed for SCM robots at the MEMS scale and the integration of joint strain sensing and piezoelectric actuation was demonstrated for flapping wing and crawling robot concepts in [140]. A version of this process with an S2-Glass fiber structural layer, polyethylene terephthalate (PET) flexural layer, and shape memory alloy (SMA) actuation was used to fabricate RoACH, an autonomous 2.4 g legged robot [57]. With similar fabrication methods and the same actuation mechanism, Kohut et al. designed and built the 5.5 g, 5 cm long MEDIC legged robot for navigating circuit boards [81]. This process eventually enabled the first controlled takeoff, hover, and steering of an 80 mg insect-scale flapping-wing robot [96]. Legged robots with enhanced movement capabilities

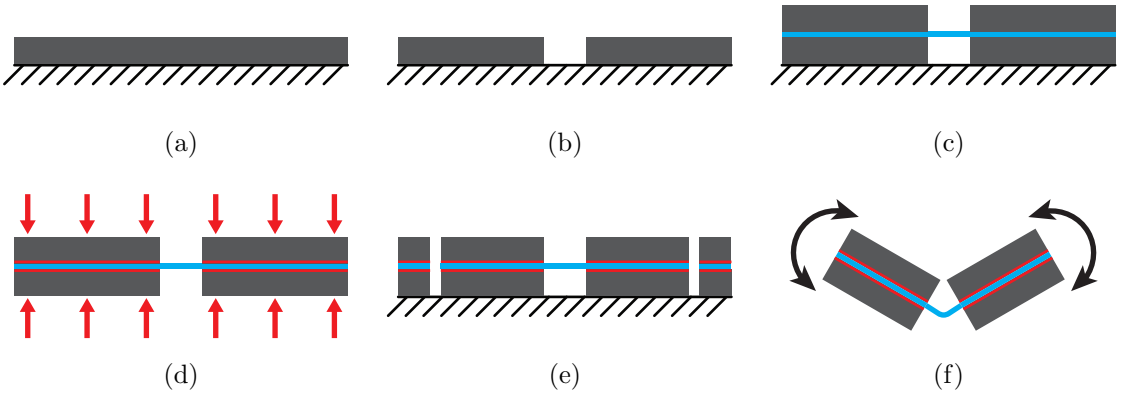


Figure 2.1: Cross-section view of the process flow for Smart Composite Microstructures (SCM) manufacturing. (a) A sheet of structural material (grey) is aligned and fixed to a laser cutter bed. (b) The laser cutter selectively removes structural material at flexural joint locations. (c) After repeating the first two steps for a second sheet of structural material, a sheet of flexural material (cyan) is placed between the two structural layers, with structural cuts aligned. (d) Heat and pressure is applied to bond the structural layers to the flexural layer with previously-applied adhesives. (e) After aligning the composite sheet to the same reference point in the laser cutter bed, the laser makes outline cuts that release the composite mechanism from the rest of the sheet. (f) The released mechanism is free to bend about flexural joints.

have also been built using the micro-scale SCM process. The 1.27 g robot HAMR-VP has piezoelectric actuation, carbon fiber structures, and polyimide flexures, and runs up to 10 body lengths per second with tethered power and control [5]. An earlier version of this robot platform, HAMR3, operated autonomously with onboard power and control (with a total mass of 1.7 g), but could only run forward at less than a body length per second [4]. Recent advances in power and control electronics for microrobots driven by high-voltage piezoelectric actuators enabled the development of HAMR-F, a 2.8 g autonomous legged robot of similar length scale that can run forward at 3.8 body lengths per second [34]. The 750 mg myriapod robot by Hoffman and Wood uses the same actuation and SCM layup, and can coordinate the phasing between modular leg segments to produce undulatory gaits [52]. To more easily assemble robots at the overall scale of a few centimeters, they can be fabricated with several attached layers that are then unfolded with a single degree of freedom to produce the final robot structure, in a process termed "pop-up book MEMS" [137] or "PC-MEMS" [124].

The original SCM process can clearly be used to create highly mobile robots at smaller scales than possible before without external actuation, but there are several considerations that limit their practicality. Although shrinking robots down to the insect scale improves their resilience to structural loading that arises from locomotion and collisions with the envi-

ronment, there is limited power, computation, and sensing that is available in an insect-scale footprint. All of the previously described SCM robot platforms have limited battery charge durations (a couple minutes) or require external power tethers. Furthermore, manufacturing is more difficult in the small-scale SCM process. A high-power UV laser is required to cut carbon fiber. In addition, a high-temperature curing step under a vacuum bag is required to bond the epoxy matrix of the carbon fiber to the polyimide flexure layer. Once fabricated, the small overall scale of the robots makes them difficult to assemble. To address the limitations of the original SCM process, a larger-scale version of the process called "scaled Smart Composite Microstructures" (hereon referred to as SCM) was developed by Hoover et al. [56]. The scaled SCM structures use cardboard as the structural layer, PET as the flexural layer, thermal adhesive and a laminator to bond layers, and can be machined using an IR laser. This process can produce robot structures at 2–10X the size scale of the original SCM process in 2–3 hours instead of 2–3 days. A whole phylogeny of legged robots has been created using this process, and they have the common features of being actuated by hobby DC motors, being able to carry a suite of sensing, communication, and control electronics, and carrying onboard power for continuous operation from 15 to 30 min in duration. Many robots have been created using the cardboard structure, PET flexure layup described in [56]. The first two autonomous robot platforms created with this process are hexapedal robots with legs driven in an alternating tripod gait for fast forward running: DASH has a sprawled posture with straight legs and compliant body structure [9] and DynaRoACH has an upright posture with curved legs [54]. Birkmeyer et al. adapted the design of DASH for vertical climbing by lowering its center of mass and placing its drive mechanism in the plane of locomotion to produce CLASH, which uses compliant ankles with spine arrays for climbing cloth [7] and gecko adhesive patches for climbing smooth surfaces [8]. In a branch from using a single motor to drive all legs, the eight-legged OctoRoACH robot used two motors to drive left/right leg sets with the capability of differential drive steering control [112]. The latest in the line of scaled SCM robots is VelociRoACH, which maintains differential drive steering control while being tuned for high-speed running [43].

As an alternative to SCM, Onal et al. developed a print-and-fold origami-based robot fabrication process, in which a single sheet of plastic (PEEK or PET) is laser cut with perforations defining folds for assembling 3D structures and kinematic joints [105]. Circuitry can also be integrated into the robot structure by using solid-ink printing of masks on copper film and wet etching to make traces, and then using a pick-and-place machine to populate components. Using this process, the researchers fabricated a 45 g, 8.2 cm long folded legged robot that could run at 41 cm/s.

To extend the mobility and sensing capability of SCM legged robots, several additional payloads have been added. This includes multi-modal legged/flapping wing locomotion by BOLT [110], inertial or aerodynamic tails for augmented turning [82] [83], an integrated jumping module on DASH [65], and a force sensing shell on VelociRoACH [35]. Very Large RoACH (a 149 g, 1.6x length scale version of VelociRoACH with tethered power) has a load decoupling platform that drags against the ground and reduces leg loading, allowing it to move forward with payloads of up to 200% of its base body weight [142]. In addition, CRAM,

a recent modification to DASH with a compliant shell and split body that sprawls under compression, demonstrated forward running speeds of 14 cm/s when crawling in confined vertical spaces with half of its body height in clearance (relative to a 27 cm/s unloaded forward speed) [61].

Simple SCM robots can leverage cooperation to enhance mobility. Robot cooperation has been demonstrated by VelociRoACH launching an ornithopter [114], cooperative step-climbing of two VelociRoACH robots with a winch connection [19], and cooperative steering of two VelociRoACH robots connected by a passive yaw joint [120].

The limitations of SCM material choice was apparent with X2-VelociRoACH [42], which used a high-power brushless DC motor to push the bounds of forward running speed. This robot replaced PET with Cuben fabric or ripstop nylon for additional tear strength, and under high leg loading the Cuben fabric tore and the cardboard structure of the leg flexures peeled back. This failure highlights a limitation of scaling up the SCM process and stronger materials are needed to prevent breaking.

After trying to scale SCM up to build folded robots at the meter length scale, Fitzner et al. [31] discovered that structure stiffness, joint misalignment, and flexure strength/off-axis stiffness scaled unfavorably. To address this limitation, the researchers developed a process called plate and reinforced flexure (PARF) fabrication, which uses laser-cut foam board plates joined together with fiber-reinforced tape. Joints can be selectively strengthened with multiple pieces of reinforcing tape attaching the top and bottom of the connecting pieces forming the flexure and wrapping around the width of the connecting pieces. The PARF fabrication process was used to create the 90 cm long robot BigANT, which can run forward at 30 cm/s.

The high-payload folded legged millirobot developed in this thesis LoadRoACH is compared to prior robots in Table 2.1. Each row details the following specifications of a folded legged robot: structural material, flexural material, overall mass (including leg mechanisms, leg actuators/transmission, control/sensing electronics, and battery), overall length, and highest reported forward running speed. With the exception of the last two entries, all of the robots in this table are fabricated using a version of the SCM process. Also note that HAMR-VP and Very Large RoACH are the only robots in this table that operate under tethered power.

While payloads including tails, shells, and jumping mechanisms have been added to SCM robots, only small payloads relative to the weight of the main body, drive actuators, batteries, and control board can be added before locomotion performance degrades. LoadRoACH, the robotic platform contributed by this dissertation, is the first palm-sized legged SCM robot (with a base mass of 54.8 g) that can support an addition of 27.2 g in payload while maintaining running performance, which is 50–170% of the overall mass of previous platforms around 10 cm in length.

Table 2.1: Comparison of folded legged robots

Robot	Structural material	Flexural material	Overall mass (g)	Overall length (cm)	Speed (cm/s)
RoACH [57]	S2-Glass	PET	2.4	3	3
MEDIC [81]	Fiberglass	PET	5.5	5	0.06
HAMR3 [4]	Carbon fiber	Polyimide	1.7	4.7	4.2
HAMR-VP† [5]	Carbon fiber	Polyimide	1.3	4.3	44
HAMR-F [34]	Carbon fiber	Polyimide	2.8	4.5	17.2
BOLT [110]	Carbon fiber	PET	11.4	18	150
DASH [9]	Cardboard	PET	16	10	150
DynaRoACH [54]	Cardboard	PET	24	10	140
OctoRoACH [112]	Cardboard	PET	35	13	50
VelociRoACH [43]	Cardboard	PET	29	10	250
TAYLRoACH [82]	Cardboard	PET	48	10–20	100
X2-VelociRoACH [42]	Cardboard	Nylon	54	10	490
Very Large RoACH† [142]	Cardboard	PET	149–449	16	6–19
CRAM [61]	Cardboard	PET	46	18	14–27
LoadRoACH w/ tail and shell [18]	PET	PET+nylon	82	15	72
Print-and-fold legged robot [105]	PET	Perforated PET	45	8.2	41
BigANT [31]	Foam board	Fiber-reinforced tape	∼3000	90	30

†Tethered power

2.2 Protective Structures of Robots

Robots that move through the natural world and human-architectured environments will come into contact with water, mud, and granular media that can potentially damage electronics and mechanical transmission components. Furthermore, small mobile robots will encounter obstacles with size scales significantly greater than their own, which can result in falls with substantial impact velocity. Search and rescue robots deployed in the field require protection from water and loose terrain, as well as from impacts that result from drops or

falls.

Swimming robots require complete protection against water leakage that could possibly damage electronics and other water-sensitive components. Hirata developed a fish robot with an articulated 2 DOF tail, whose electronic components are waterproofed by passing drive linkages through linear bearings, with rubber O-rings clamped between rigid body casing components [49]. Similar water-sealing methodology is applied to the designs of underwater robots BoxyBot [89], which has three actuators that drive one caudal fin and two pectoral fins, and HippoCampus [39], which is driven by four propellers. An alternative strategy is demonstrated in the water-proofing of the legged salamander-inspired amphibious Pleurobot [69]. The base design of the four-legged Pleurobot is prone to water damage and consists of 27 servomotors driving the spine, tail, and legs. To protect the motors and control electronics from water, the robot is placed in a flexible "dry-suit" that is manufactured using stitched together pieces of nylon fabric laminated with polyurethane. A waterproof zipper allows the the dry-suit to be placed over or removed from the robot, and the robot's steel leg rods are press-fit through glued-in silicone cylinders to enable foot contact with the environment.

Jumping robots need to withstand impact forces from high-speed collisions, and many of them employ compliant elements to protect their electronics and weaker structural components. The wind-up jumping robot designed by Kovač et al. incorporates a lightweight impact-absorbing cage structure made of thin carbon fiber rods connected with 3D printed ABS joints [85]. Similarly, Jollbot [2] jumps by compressing then releasing a surrounding spring steel cage, which also provides impact protection. The tethered jumping robot built by Sugiyama and Hirai [127] consists of SMA spokes that store energy by deforming a surrounding rubber ring, which provides viscoelastic protection. Similarly, Tolley et al. made an untethered soft robot with pneumatic leg actuation and explosive jumping actuation that is encased in silicone rubber, which absorbs energy during impacts [130].

Flying robots also benefit from crash-proofing to protect propellers and electronics from collisions after flight malfunctions or during navigation of cluttered environments. Many commercial drones are equipped with protective cages, such as the AscTec Hummingbird with propeller guards connected by carbon fiber rods used in [71], or the Qball-X4 with a polyhedral carbon fiber cage providing protection from all impact orientations used in [134]. Klaptocz et al. developed a tetrahedral protective structure for a rotorcraft [78], which arranges carbon fiber rods in a frame that absorbs energy through Euler beam buckling. Briod et al. designed the GimBall rotorcraft [13] with a carbon fiber frame whose rotation is decoupled from the main propulsion and steering modules via a gimbal system, which minimizes the effect of impacts on the orientation of the flight control elements. GimBall can autonomously navigate densely cluttered forests while withstanding multiple collisions.

Ground robots can also expand their utility in real-world environments through impact resilience, which allows them to fall from heights of several times their length scale without being damaged. O'Halloran et al. designed a two-wheeled robot with shock reduction elements in the wheels, transmission, and suspension that could withstand impact forces from a 3 story drop [104]. Chanthasopeephan et al. developed a legged/rolling robot whose compliant legs absorb impacts from falls up to 1 m [23]. The compliant frame of the 16 g folded

legged millirobot DASH (fabricated using SCM) absorbs impact to help survive terminal velocity falls [9]. Recently, DASH's compliant body construction was shown by Jayaram et al. to facilitate horizontal to vertical transitions after head-on collisions with walls, reproducing the dynamic transition behavior of cockroaches [62]. A viable alternative to SCM for creating centimeter-scale ground robots with integrated compliance and kinematic joints is shape deposition manufacturing (SDM) as implemented by Cham et al. [20]. SDM is a process that leverages successive steps of 3-axis CNC milling and deposition of rigid and viscoelastic polyurethane plastics, with wax support material. This process can be used to create integrated compliant leg joints and chassis with embedded electronic components, which provide impact protection while removing stress concentrations of fasteners and connectors. However, integration of body compliance into a robot's structure to mitigate impact damage is not always feasible if significant payloads need to be carried by the robot.

In the context of protective structures for vehicles and robots, thermoforming is a common manufacturing process. However, the application of thermoformed protective structures to centimeter-scale SCM robots is especially challenging because added weight to the robot has the cost of significantly reducing locomotion performance. For this reason, the thermoformed exoskeleton needs to be thin, compliant, and use minimal fasteners and adhesives.

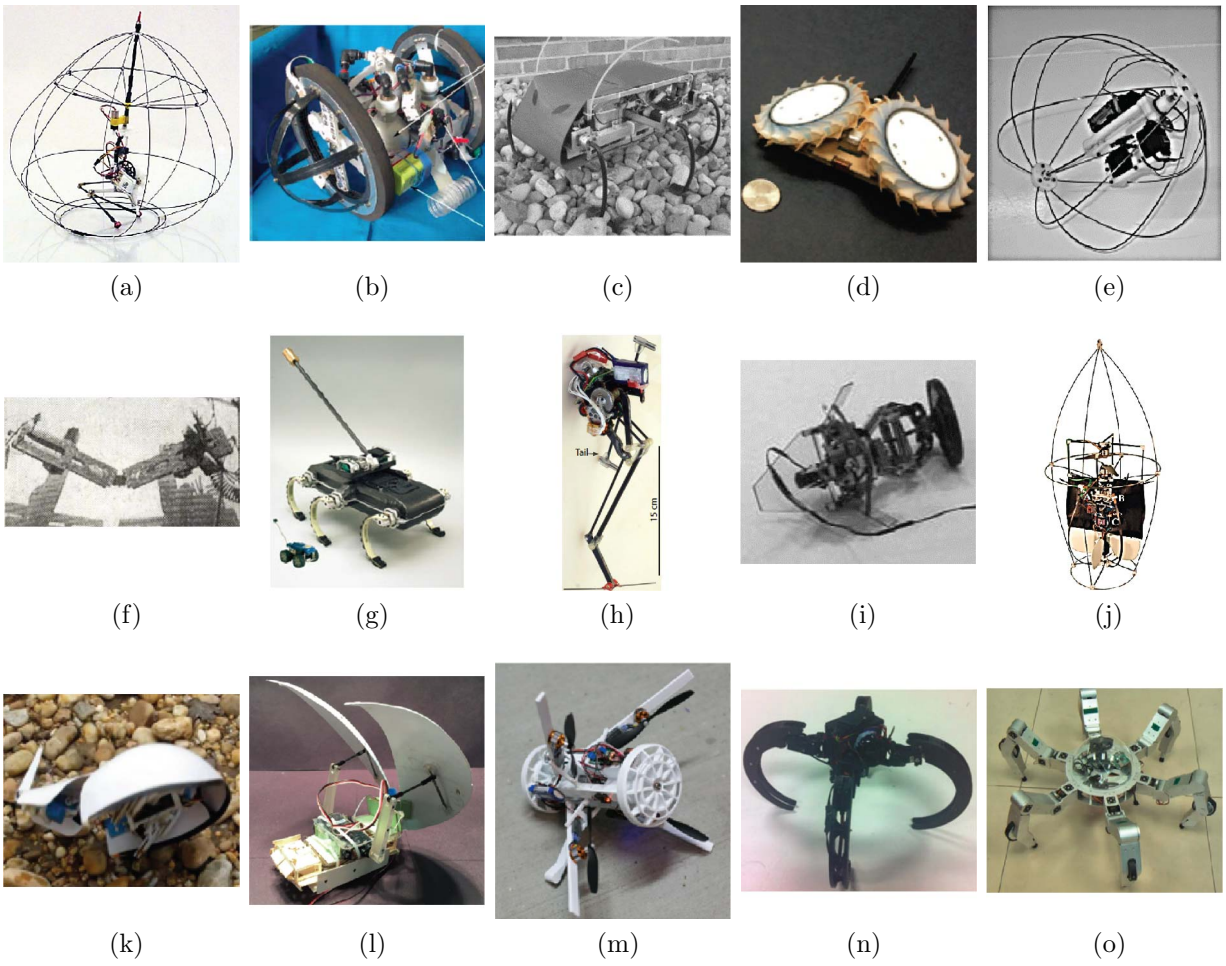
In addition, the geometry of the SCM kinematic linkages make it difficult to seal the robot against the environment without restricting the legs. Traditional methods for sealing against fluids, such as compressing a rubber gasket between two rigid components, are not feasible in this application because of the high weight costs.

With the above considerations in mind, this work aims to expand the application of water resistant and impact-reducing structures to folded millirobots.

2.3 Self-Righting Strategies of Animals and Robots

Robots that are free to run outside of controlled laboratory environments will encounter unstructured terrain with various length scales of rugosity. This challenging terrain can cause a robot to unexpectedly flip or tumble, which necessitates the ability to self-right. With rapid self-righting capability, search and rescue robots can quickly recover from an immobilized posture to maintain contact of propelling appendages and make progress towards a goal location. To accompany the robot descriptions in this section, representative pictures of robots capable of self-righting are shown in Figure 2.2.

One approach to self-righting is to design a robot's shape so that it passively reorients to a righted configuration, which can be achieved using the capture regions analysis developed by Kriegman [86]. Some species of turtles have particularly tall shells that either passively self-right under gravity with terrain contact, or require little pushing effort from limbs [28]. Robots that are designed to passively self-right use a combination of convex hull shaping and a low center of mass. The jumping robot with carbon fiber roll cage designed by Kovač et al. [85] and the hybrid air/ground vehicle Rotochute [6] have a tall egg-shaped cage with mass concentrated at a flat bottom towards which the robot preferentially lands. The first



(a) (b) (c) (d) (e)

(f) (g) (h) (i) (j)

(k) (l) (m) (n) (o)

Figure 2.2: Pictures of robots capable of self-righting. Passively self-righting robots: (a) jumping robot by Kovač et al. [85] and (b) wheeled/jumping robot by Tsukagoshi et al. [132]. Invertible robot designs: (c) RHex [115] and (d) PUFFER [70]. (e) Jollbot [2] self-rights through shape change. Inertial self-righting robots: (f) cat-inspired two DOF spine by Yamafuji et al. [141], (g) Tailbot [22] and RHex [93] with offset mass tails, and (h) Salto with balanced tail [44]. Ground pushing self-righting robots: (i) gen. 2 jumping robot by Burdick and Fiorini [15], (j) AirBurr tailsitter rotorcraft [79], (k) horseshoe crab robot [87], (l) cockroach-inspired winged robot model [90], (m) hybrid ground/air vehicle [100], (n) Scorpio legged robot [129], and (o) NOROS legged robot [109].

generation jumping robot for celestial exploration built by Burdick and Fiorini is a sphere with a low center of mass [15]. The wheeled and pneumatic jumping search and rescue robot by Tsukagoshi et al. [132] is a narrow cylinder with spherical caps on the ends of the cylinder, which passively tips onto its wheels after landing. Another passive self-righting strategy is to design a robot that can operate from multiple orientations, such as the hexapedal legged

robot RHex [115], which has legs that can fully rotate and contact the ground in both upright and inverted postures, and the wheeled pop-up rover PUFFER [70], which has large wheels that encompass its body and a passive tail that causes the robot to flip upright in forward drive and flip inverted when driving backwards.

While passive self-righting methods can be robust to environment conditions, they may limit mobility in the case that a robot needs to navigate tight spaces and low clearances. Active methods for self-righting require coordination of a robot's actuators and there are a variety of strategies including reconfiguring shape or mass distribution to tilt towards one side, inertial reorientation by pushing on internal degrees of freedom while airborne, and reorientation through ground contact. Animals have a high degree of neuromechanical control over their body and limb functions, and as such, exhibit a diverse set of self-righting behaviors that provide inspiration for robot designs.

In line with shaping capture regions of shapes with a given mass distribution, there are some robots that make slight adjustments to their convex hull or center of mass to tip upright. This mode of active self-righting is exhibited in road and blister beetles [32], which initiate self-righting by arching their bodies towards the ground to raise their center of mass, with the middle leg, head, and last abdominal segment contacting the ground. With an unstable body posture, these beetles can easily tip towards their sides and then complete self-righting using their legs. The Jollbot prepares to jump by compressing its spherical steel cage into an ellipse elongated perpendicular to the jumping axis, which causes the robot to passively roll to align its jumping mechanism with respect to the ground [2]. An earlier version of the jumping robot with carbon fiber roll cage by Kovač et al. [84] shifted its center of mass downward along an axis of a spherical cage to self-right towards its legs, which was coupled with energy storage and leg retraction in preparation for the next jump. Similarly, the single actuator jumping/rolling robot designed by Ho and Lee [50] has a cylindrical frame and shifts its center of mass radially along the cylinder to roll towards its foot while storing energy for a jump.

A large set of bio-inspired self-righting strategies fall in the category of inertial righting. The principle of inertial righting dates back to the falling cat problem—physicists observed that a cat can articulate its body in a back bending maneuver that conserves angular momentum to roll over while airborne and land on its feet [68]. Yamafuji et al. built a robot with a two DOF pneumatically actuated spine that exploits this same principle [141]. Dyhr et al. performed experiments with hawkmoths that showed the animal reflexively moves its massive abdomen in response to visual stimuli to stabilize flight [29]. Jusufi et al. discovered that lizards can push on the massive inertia of their long tails to right and turn in mid-air [66] [67], which later was discovered to extend to pitch correction after slipping during a jump off of a low-friction vault by Libby et al. [94]. Libby, Chang-Siu, and Johnson et al. analyzed and tested a lizard-inspired strategy for aerial self-righting, in which a robot pushes on the inertia of a massive tail to reorient its body [94] [21], and reaction wheel, tail, and legged strategies for inertial righting can be mathematically anchored to a simple template [93]. One of the first robots to use an inertial tail to balance pitch attitude was the Uniroo hopping robot [144]. Similarly, the kangaroo-inspired hopping robot by Liu et al. [95] uses

an inertial tail to limit pitch oscillations during hopping. The MSU tailbot jumping robot [146], the UC Berkeley Tailbot [22], and RHex with tail [93] all use a tail with offset mass at the end to correct their pitch attitude while airborne. The Salto jumping robot [44] uses a balanced inertial tail to correct its pitch attitude while airborne. The water running robot built by Kim et al. [75] uses a massive tail that rotates in the yaw plane to stabilize roll oscillations of the body. An inertial tail on the MIT Cheetah can be used to reject impulsive disturbances [11]. Taking inspiration from how hawkmoths use their massive abdomens to redirect flight force, Demir et al. attached the battery pack of a quadrotor drone to the end of a servo, which enabled it to act as a tail for rejecting pitch disturbances [27]. Inertial moments from reaction wheels can even be used as the primary actuation method for locomotion, as demonstrated by the internally actuated rovers for low-gravity planetary bodies developed by Hockman et al. [51]. These rovers can spin up and brake three orthogonal reaction wheels to perform tumbling, hopping, and twisting motions starting from rest on ground terrain.

While inertial reorientation strategies are well understood and can rapidly self-right a robot while airborne, terrestrial robots may not always have enough time to reorient during a fall. Furthermore, inertial righting strategies rely on morphologies that have large appendage inertia, which may hinder other locomotion tasks. There are many animals and robots that push against the ground with limbs or tail-like appendages to self-right. Turtles with flat or medium shell height profiles rely on neck and foot pushing to complete self-righting [28]. Locusts self-right by pushing primarily with a hind leg to roll about a longitudinal axis, while tucking the hind leg on the opposite side away from the rolling motion [30]. Frantsevich performed comprehensive experiments showing diverse mechanisms for self-righting in 116 representative species of beetles [32]. The most common strategies involved surface grasping with a single leg on high-friction surfaces to produce a righting moment with a large lateral component and somersaulting by pushing with the stable support of two limbs.

Kessens et al. developed a quasi-static framework for contact planning with actuated limbs that change a robot's convex hull to reorient on sloped surfaces [73]. An extension of this work established a self-rightability metric based on potential energy barriers to righting [72].

Many robots perform quasi-static self-righting with ground contact of appendages, in which the forces and accelerations to dynamically move past energy barriers are negligible. The actuated appendages are often dedicated to self-righting. The second generation jumping robot for celestial exploration built by Burdick and Fiorini could self-right by pushing outward with flaps that deploy from the sides and back of the robot to reorient onto its foot after landing [15]. The AirBurr tailsitter rotorcraft with an elongated body self-rights after a crash by deploying four spring-loaded arms to tilt from its side to point its propellers upward [79]. Krummel et al. designed a horseshoe crab robot that can self-right in surf zones by pushing its tail against the ground to roll its body upright [87].

For other self-righting robots that utilize ground-contacting appendages, their self-righting actuation is coupled to other functions. Morton and Papanikolopoulos developed a hybrid ground/air vehicle that transforms from a wheeled configuration to a flying configuration

with propellers deployed, and the propeller arms push against the ground during deployment to reorient the robot for flight [100]. Chen et al. built a jumping robot that pushes against the ground with an appendage that rotates overhead the robot to self-right coupled with storing spring energy for the next jump [24]. Zhang et al. demonstrated self-righting of a wind-up jumping robot using a pole leg (which can also be used to adjust the robot's jump heading) to push the robot onto its legs from side-laying or front-laying landing orientations [145]. The MSU tailbot uses its tail for inertial attitude correction in the air and also as a ground-contacting appendage after jumping to transition between a laying-down posture to an upright posture from which it can jump again [146]. The quadruped SpotMini developed by Boston Dynamics uses a top-mounted five DOF arm for object manipulation and self-righting [123].

The final class of robots that self-right through ground contact have many actuated DOF of legs or internal joints that can be coordinated in self-righting procedures. The four-legged rolling/walking Scorpio robot [129], which has three actuated DOF per leg, can coordinate its leg motions to transform between locomotion modes and recover from being tipped on its side. Peng et al. developed open-loop leg motion plans for terrestrial self-righting of the NOROS robot [109], which has six legs articulated by three servo motors each. This leg trajectory plan positions two legs along a line to provide a support axis, and the other four legs stably push to rotate the robot upright. The three-unit JL-I modular robot has treaded modules connected by three DOF spherical joints, which can be coordinated to self-right from postures in which the modules are laying on their side or back [37]. The HyQ2Max hydraulic quadruped robot has three actuated DOF per leg, and the improved joint layout and extended joint ranges relative to previous HyQ robot designs enable it to push overhead with one lateral pair of legs and roll its body upright [119].

Li et al. thoroughly analyzed the threshold of quasi-static self-righting for cockroach-inspired winged robot models, and predicted how much energy would need to be injected to overcome energy barriers in the case that the robot can not simply quasi-statically self-right [90]. The researchers found that both the winged robot model and cockroaches that used wings to aid in self-righting had wing morphologies that necessitated some injected kinetic energy indicative of dynamic self-righting. In a case where dynamic self-righting is clearly required, Saranli et al. controlled the six leg actuators of RHex within a multi-contact dynamic framework to execute a flip about its pitch axis [116]. However, in the case of ground contacting appendages, most robots quasi-statically self-right and their speed of execution is much slower than their animal counterparts.

2.4 Turning Strategies of Legged Animals and Robots

Legged animals have a diversity of turning mechanisms that provide inspiration for roboticists to design maneuverable mechatronic systems. Animals exhibit complex turning behaviors that range from gradual turns to rapid turning escape responses, and have many independent muscles that control their leg motions. Often there are synergies between leg sets following

a consistent gait, and straight walking or running can be biased to steer towards a given direction with slight adjustments to that gait. Woodlice turn by further extending and increasing the step length of the legs on one side [59]. Crayfish also turn by increasing step length of legs on the outside of the turn [25]. Common fruit flies turn by decreasing step length on the inside of the turn [126]. Several species of ants turn by maintaining an alternating tripod gait pattern with similar relative footfalls within a tripod, but the tripods are rotated relative to the body and the inner legs take shorter steps [147]. Adult stick insects turn by temporarily desynchronizing their step pattern to speed up legs on one side of the body [36].

Although several animals have been observed to follow kinematic turning strategies in which they vary stride length, foot placement, or stride frequency, there have been several observations of dynamic strategies in which ground reaction forces are redirected to change heading in either a periodic gait or a transient maneuver. Jindrich and Full found that to produce large turns, the discoid cockroach does not significantly alter its gait pattern relative to straight running, but instead generates forces causing most of the linear and angular impulse required for the turn with the legs on the outside of the turn [63]. Through a simple mathematical model in this study, the researchers postulated that any leg of the cockroach could be used to produce the momentum change required for turning during forward running, and the front legs can turn with the greatest effectiveness by pushing perpendicular to the instantaneous forward velocity. Similarly, ostriches turn with minimal changes to leg kinematics or net torque production at each joint, and roll their body away from the turn to reduce braking or acceleration forces required to turn [64]. Wild mice making a 90 degree turn on a track maintain a bounding gait pattern while adjusting body posture and force production [133]. The mouse first plants its front feet toward the outside of the turn and rotates its head towards the turn, then twists its lower body into the turn, and then pushes directly forward with their hind limbs with greatly reduced body inertia. The escape response of the American cockroach is also a very dynamic behavior [16]. In response to a wind puff on one side, the cockroach abrubtly halts the current gait and pushes simultaneously with all six legs to turn, with all legs acting to purely rotate the body about the back end of the cockroach. The cockroach then transitions to its regular alternating tripod gait for straight running.

The lateral leg spring (LLS) model developed by Schmitt and Holmes reduces a many-legged animal to a single effective leg in stance per stride and predicts that turning can be produced with changes in leg stiffness, leg length, touchdown angle, or center of pressure [118]. This template qualitatively matches cockroach turning behavior. Changes in leg length and touchdown angle of a single effective leg in stance model kinematic turning gaits, and changes in center of pressure of a single effective leg in stance model the asymmetric leg force distributions found in dynamic turning. This template-level modeling of biological turning projects that animal and robot anchor systems can achieve turning through various strategies.

There is a large class of robots that are heavily actuated, with multiple actuated DOF for each limb and body segment that can be coordinated for turning gaits. These robots

are generally heavier and less dynamic than animals or minimally actuated robots. The University of New South Wales Robocup 2000 team developed an omnidirectional locomotion method for the quadruped Sony ERS-110 robot with three actuated DOF per leg [47]. The locomotion method was to follow trotting gaits with rectangular foot paths that lie in vertical planes at different angles relative to the robot to achieve forward/backward, sideways, and point turn motions that could be composed to reach a desired position and orientation faster than other Robocup competitors. Degrave et al. tested similar feedforward turning gaits on the Oncilla quadruped robot, which has three actuated DOF per leg [26]. The Oncilla robot turns by decreasing step size on one side or by maintaining the same nominal half ellipse leg trajectories as for forward walking, while using its leg scalpulae to rotate its front legs outwards from the sagittal plane away from the center of the turn and its back legs towards the center of the turn. Horvat et al. implemented a synchronized spine and leg controller for the Pleurobot, which is a quadruped with four actuated DOF per leg and five actuated yaw joints in its spine that connect the front leg set and back leg set [58]. Pleurobot can use this controller to turn by enforcing the linear and angular velocity of the front leg segment with the front legs, and then coordinating the spine motion to have the back leg segment follow the same orientation of the time history of the front leg segment motion. Tsujita et al. developed a control strategy for kinematic and dynamic turning of a quadruped robot with three active DOF per leg and a driven yaw body joint [131]. The first part of this control strategy is a spontaneous locomotion controller that generates nominal joint trajectories for each leg driven by non-linear oscillators, which are then maintained through feedback control of individual joint torques and contact detection to adjust the leg oscillator phasing based on when each foot actually hits the ground. The second part of the control strategy is a voluntary motion controller that adjusts the leg tip velocities during contact, leg contact periods, body yaw joint configuration, and body posture towards the inside of the turn based on the desired turning gait. The hexapedal RiSE robot, which has two actuated DOF per leg with force sensing at the feet, implements a similar control strategy to climb and turn on vertical poles and building faces [122]. RiSE follows a feedforward spatial gait trajectory that is adjusted based on foot interactions with the surface and turns by differentially adjusting the force applied at its left and right feet.

Small, highly mobile legged robots are often underactuated to achieve fast running performance. This class of robots includes SCM robots built from folded structures. These robots, which have simply driven appendages with coupled leg motions and passive joints, have a variety of turning strategies that fall into two categories—kinematic turning and dynamic turning.

Kinematic turning strategies adjust the position or velocity parameters of individual leg motions to effect a body rotation. One of the first minimally actuated robots was the quadrupedal Scout-1 robot with one motor per leg, which turns by adjusting left/right phase parameters of its periodic gait [14]. Similarly, the hexapedal RHex robot turns using left/right differential adjustment of Buehler clock phase and stance time parameters [115]. The 2.4 g hexapedal RoACH robot can turn by picking its middle legs up off the ground and placing the four front/back legs on the ground such that one side of legs swings back while

the other swings forward, producing a kinematic turn [57]. The myriapod robot by Hoffman et al. is composed of compliantly-connected modular segments (up to 8 demonstrated), which has left/right leg sets with coupled swing and lift actuation to alternate steps with each side (two independent actuation signals) [53]. This myriapod robot can effectively turn using a single driving waveform with a different phase offset for each segment, which drives the legs with a shorter duty factor of contact on one side and causes a turn towards that side. The quadrupedal HAMR-VP microrobot turns by adjusting the phase of its left/right leg lift cycles to deviate from a nominal trotting gait [5]. The hexapedal iSprawl robot turns by adjusting foot placement through a shift in the equilibrium position of certain legs in its resonant running gait [76]. The hexapod built by Hayashi et al. drives each leg with a servo motor for sagittal plane swinging and a solenoid for leg extension/retraction, and turns by taking shorter steps with one side of legs [45]. Z. Wang et al. analyzed and tested a turning method for a hexapod with each leg driven by a single DOF Jansen mechanism [136]. By differentially lengthening a single link in the Jansen mechanism of the legs on one side relative to the other, the robot maintains flat leg trajectories along the ground and a combination of duty factor adjustment and differential leg tip velocity changes causes the robot to turn. The Mini-Whegs series of robots with four wheel-legs maintains an alternating diagonal gait with a single drive motor, and turns by moving a servo actuated sliding rack driving the steering arm connected to the vertical pivot of each front wheel axle [99]. Similarly, the hexapedal DASH robot runs in an alternating tripod gait driven by one actuator and turns by using a servo motor to skew its compliant leg support structures, biasing its leg motions towards one side [9]. The octopedal OctoRoACH robot turns through differential velocity control of the two motors driving left and right leg sets [112]. The hexapedal VelociRoACH robot [43] can also turn with differential velocity control of its left and right leg sets. A pair of VelociRoACH robots connected by a passive compliant yaw joint have augmented turning performance on various surfaces with velocity control of four independent motors [120].

Kinematic turning strategies can be less effective for legged robots running at faster speeds because they do not consider oscillatory dynamics, inertial forces, and transient contact forces during turning. Both the Scout II quadruped [106] and the quadruped designed by X. Wang et al. [135] have a single rotary actuator driving each compliant leg, and these robots turn by applying a larger leg motor torque during stance of the legs toward the outside of a turn. Many dynamic turning strategies rely on carefully tuned compliance of legs. The hexapedal DynaRoACH SCM robot drives its legs in an alternating tripod gait with a single motor and can rapidly turn by stiffening the middle leg towards the outside of the turn, with large roll and pitch oscillations excited relative to straight running with uniform leg stiffness [54]. Haldane and Fearing applied a reduced-order roll plane model of the VelociRoACH compliant legged robot and showed that for periodic gaits of a fixed frequency with a left/right phase offset that deviates from an alternating tripod, the middle legs apply asymmetric braking forces that produce dynamic turns [41]. The single actuator hexapedal 1STAR robot follows an alternating tripod gait with wheel-legs and turns by applying alternating acceleration and deceleration phases of leg rotation between stances, which consistently produce a turn in one direction due to having soft middle legs and stiff

front/back legs during a tripod stance [143]. Many-segmented robots can also leverage the passive dynamics of their body connections to enhance turning. Aoi et al. [1] demonstrated this phenomenon for six modules connected by passive yaw springs with two legs each. The researchers found that when the spring constants of the connected modules fall below a certain threshold, a stability bifurcation occurs that causes body undulations during straight walking and this instability enhances the maneuverability of the robot during turning gaits. In a unique demonstration of how dynamic body reconfiguration can enhance turning, Nie et al. showed that actively shifting a floating mass from the rear to the front of a four-wheeled vehicle while executing a turn causes it to enter a controlled drift with a rapid yaw reorientation [102]. For a comprehensive survey of turning methods for legged robots, refer to the thesis of A. J. McClung [97].

In addition to kinematic or dynamic modulation of legged gaits for turning, there are some methods that dedicate actuation to turning that is decoupled from the legs. This can be especially useful for underactuated robots that cannot directly control lateral pushing and pulling forces. The hexapedal TAYLRoACH SCM robot can execute rapid transient turns on low-friction surfaces through the inertial effect of swinging a tail in the yaw plane [82]. A later iteration of this robot, SailRoACH, uses a tail for rapid turning through the generation of both transient inertial and sustained aerodynamic yaw moments [83]. Similarly, the water-running robot developed by Kim et al. turns with yaw moments generated by hydrodynamic forces acting on a submerged tail [74]. Patel and Braae enhanced the turning performance of the Dima wheeled robot, which swings a massive roll tail during high-speed turning to counteract large centripetal accelerations that would otherwise tip the robot over [108]. Finally, Zhang et al. demonstrated slow heading changes of a jumping robot before takeoff using ground contact of a tail appendage [145].

2.5 Locomotion with Terrain Contact of a Tail

Although there is a significant body of work in the fields of biology and robotics on using tails or tail-like appendages for self-righting, turning, and other reorientation tasks, there is limited research on tail contact coordinated with legged locomotion. Jusifi et al. performed experiments with geckos that showed during climbing, a gecko's tail pushes on the wall to prevent pitching back and functions as an emergency fifth leg for recovery from wall detachment [66]. Willey et al. found that the American alligator must compensate for a dragging force of its massive tail (28% of its body mass), and that this may contribute to the low energy recovery of their walking gait [138]. McInroe et al. showed through experiments with a biological model (mudskipper) and a physical robot model (MuddyBot driven by laterally positioned forelimbs and a posterior tail) that using a large tail for propulsion coordinated with forelimb motion improves forward progress on sandy inclines and is an important biomechanical feature of early vertebrate land locomotors that transitioned from aquatic to terrestrial domains [98]. O'Connor et al. discovered that kangaroos use their tail to propel and power low-speed locomotion in a pentapedal gait [103]. During brachiation,

primates use their tail as an additional locomotion appendage to grasp and swing from branches [117].

Robots primarily take inspiration from animal tails in their implementation for stabilizing walking and climbing locomotion. The dinosaur-like TITRUS-III robot uses tail-ground contact to stabilize quasi-static gaits [128]. Several robots, including Scout [125], RiSE [122], Stickybot [77], and Waalbot II [101], have an extended passive tail that contacts the climbing surface to prevent pitch-back. Seo et al. designed a tracked robot that pushes with an active tail to stabilize climbing and transition between orthogonal surfaces [121]. The tracked HELIOS robot [38] and the wheel-legged SeaDog robot [80] use compliant tails to stabilize climbing over step obstacles. The wheel-legged robot with active wheel/tail appendage RoMiRAMT-II pushes with the tail to assist in climbing step obstacles and drags the tail with anisotropic lateral friction to limit lateral deviation during straight locomotion [88]. Hemes and Papanikolopoulos showed with an analytic quasi-static model that a robot with an actuated tail-like appendage can tumble onto tall steps with a lower coefficient of friction requirement than a wheeled robot of comparable size and complexity [46]. In a unique demonstration of how an active tail can be functionalized as an appendage powering locomotion, Brill et al. explored the hybrid dynamics of the tailed Jerboa robot to find empirical contact sequences that lead to high jumps and significant horizontal gap crossings [12]. The novel robot platform in this thesis introduces the use of a multi-functional single DOF tail on a legged robot for rapid self-righting as well as dynamic turns leveraging ground contact.

Chapter 3

Exoskeletal Shells for Folded Millirobots

In this chapter, we demonstrate the manufacturing of an integrated exoskeletal shell that is compatible with the SCM rapid prototyping process. The developed exoskeleton manufacturing process uses the adaptable thermoforming process to create a variety of shell shapes through CAD-driven laser cutting and 3D printing of molds. These mold prototyping processes allow for rapid, low-cost iteration of shell molds to accelerate from the proof-of-concept stages up through to field deployment. Thermoforming is inexpensive, quick, and the process produces shells that can be recycled. Our exoskeleton manufacturing process leverages the thermoforming of multiple materials to produce a compliant structure that protects against falls, collisions, and other sources of potential damage from the environment. This structural shell is integrated with a flexible shell that seals the robot against water, sand, and mud during locomotion through complex terrain. The exoskeleton is integrated into the VelociRoACH robot platform while permitting mobility of the SCM linkages that drive the legs.

3.1 Thermoforming for Integrated Robot Shells

Thermoforming provides a means to fabricate a wide variety of integrated protective structures for robots. The vacuum-forming process is simple: a sheet of thermoplastic polymer is heated and then drawn over a mold with vacuum pressure, as shown in Figure 3.1. The mechanical properties (e.g. stiffness, damping) of the protective structures can be tuned by adjusting the type and thickness of thermoplastic used. Vacuum-formed components are inexpensive and rapid to produce, similar to the SCM robots that they protect.

Three components are required to manufacture vacuum-formed parts: a thermoforming machine, a mold, and a thermoplastic sheet. We use the *Formech* Compact Mini vacuum former. There are many way to design and manufacture vacuum forming molds. Surfaces generated from mathematical equations (e.g. with software like K3Dsurf) are simply

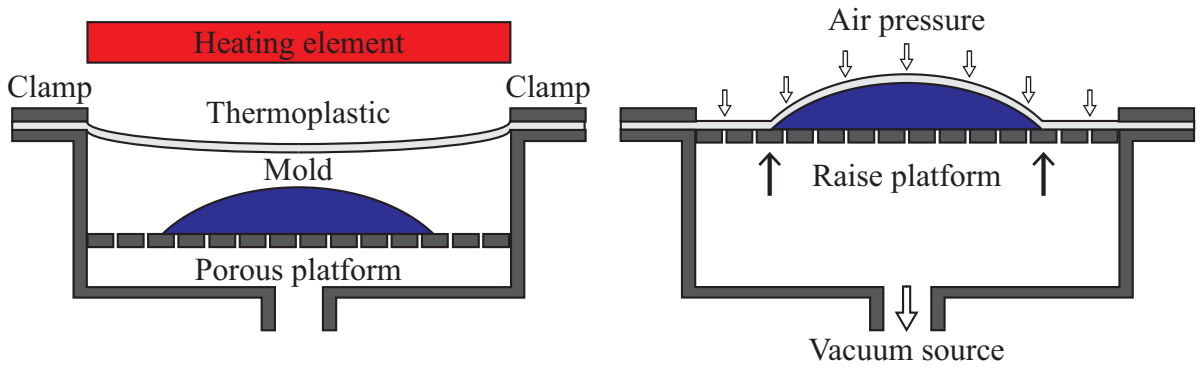
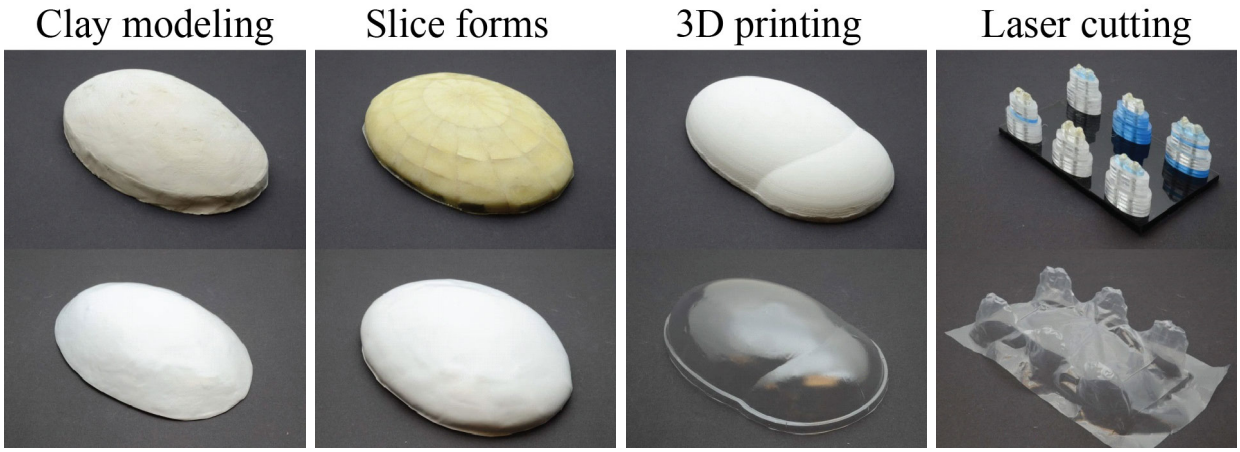


Figure 3.1: Schematic of the thermoforming process. (a) Heating of a thermoplastic sheet softens it above a positive mold. (b) Pressure difference from a vacuum source forms the softened thermoplastic onto a positive mold into the desired shape.

controlled and easily varied by a small number of geometric parameters. 3D CAD (e.g. SolidWorks) offers an alternative for designing exoskeletons of shapes of greater complexity. The mold needs to be designed such that the plastic sheet, once formed, is removable. This is accomplished with either universal positive draft angle, or a multi-part mold. Once the mold is designed, a physical version can be constructed using a variety of techniques, each of which has associated trade-offs.

Molds of arbitrary geometry can be sculpted with clay (Figure 3.2a, Sculpey clay). This method is straightforward and has low cost but is imprecise. Slice forms are an alternative that is also low in cost and more precise than clay. We used cardboard forms filled with polyurethane foam (Figure 3.2b, generated by Autodesk 123D). These two methods can be used to rapidly produce molds, and do not require any specialty equipment. They are most suited to creating proof-of-concept molds for low fidelity prototypes. Other methods can be used if more accuracy is needed. 3D printing (Figure 3.2c, printed with polylactic acid (PLA) plastic using an *Ultimaker* 2) is precise but also expensive and time consuming. Laser cut molds (Figure 3.2d, *VersaLaser* VL-200) are accurate but mostly limited to stacks of 2D shapes.

After the mold has been manufactured, it remains to select an appropriate polymer film to fabricate the shell structure. Many materials can be used—the only restrictions are that the polymer is a thermoplastic and that the film thickness is in a workable range. We have found good success with 760 μm thick polystyrene, 250–510 μm thick ABS, 130–250 μm thick polycarbonate, and 50–150 μm thick high density polyethylene. The former three materials are useful for structural shells, with polycarbonate having the largest flexural modulus (2.38 GPa) and the best forming of features that require large deformation of the formed material. Polyethylene is useful for forming flexible barriers against water and



(a) (b) (c) (d)

Figure 3.2: Top: molds constructed using (a) clay modeling, (b) slice forms, (c) 3D printing, and (d) laser cutting. Bottom: exoskeletal shells made from these molds by thermoforming using (a,b) 750 μm polystyrene, (c) 250 μm polycarbonate, and (d) 50 μm polyethylene.

granular terrain.

After the mold is prepared and the material is selected, parts can be made with the vacuum former. First, the plastic sheet is clamped to the frame of the vacuum former, and heated by heating elements above until it begins to sag (e.g. 230 °C, 30 s for 750 μm polystyrene, 25 s for 250 μm polycarbonate) (Figure 3.1a). The heating elements are then removed, and the positive mold sitting on a stage underneath is quickly raised while a vacuum source is turned on. This results in cool air pressing the softened plastic sheet onto the mold and forming it into the shape of the mold (Figure 3.1b). Finally, we trim away excess plastic at the base and smooth the edges to obtain the exoskeletal shell. In this way, complex integrated structures for robots can be rapidly produced.

3.2 Flexible Shell for Environmental Protection

For operation of SCM robots in potentially harmful environments, we want to add protection from water and granular media without limiting the motion of the robot. However, we do not want to simply encapsulate the whole robot in a flexible layer because there needs to be an interface for the appendages to interact with the environment. For convenience, we also want the option to have the flexible shell be resealable.

3.2.1 Design

We designed the flexible shell as a custom shaped “bag” made from high density polyethylene. This material has the benefits of being able to be formed on a thermoforming machine, and

being able to be heat welded with a hand heat sealer (*Audion Elektro*). We assumed that the bag was inextensible and designed the bottom layer of the polyethylene bag to allow the robot mechanisms to move freely by adding the appropriate amount of slack. The geometry of the thermoformed bottom bag layer is shown in Figure 3.3. An image of a robot leg passed through a protruding section of the bottom bag layer is shown in Figure 3.4b.

There are several options to make the flexible shell resistant or impervious to the environment. If the robot needs to be waterproof, it can be fully heat sealed inside the bag. This approach precludes easy maintenance access to the robot. Water-resistant polyethylene zippers can be incorporated into the flexible layer to provide a reclosable seal against the environment, as shown in Figure 3.9b. This zipper leaks when submerged at depth in liquid, making the shielding merely water resistant, and not waterproof.

The interface from the inside of the sealed bag is a two-part snap fit attachment. Half of the interface is attached to the robot hip inside the flexible bag layer. The other half is outside the bag layer and snaps into the inner piece, wedging the bag layer between the two components. A cross section of the cast polyurethane (*Innovative Polymers* TP-4014) segmented leg mount that is designed for this purpose is shown in Figure 3.4. Modular legs for the robot slide into dovetail connections on the outer components.

3.2.2 Manufacturing

The process for manufacturing the flexible shell is shown in Figure 3.3. The process begins by thermoforming protrusions into one side of a 51 μm thick split polyethylene zipper bag (Figure 3.3a). Next, volume to accommodate the robot is thermoformed into the other side of the bag (Figure 3.3b). Then, the zipper halves are joined and a hand heat sealer (*Audion Elektro*) is used to heat weld the three edges of the bag (welding through the zipper on the sides) and the bag is cut at the outer extent of the heat weld (Figure 3.3c). The formed flexible shell protects the robot from water and granular terrain, is resealable, and allows for legged locomotion in conjunction with the leg mounts shown in Figure 3.4.

3.2.3 Characterization

To test that the resealable flexible shell provides protection against the intrusion of granular media and water, VelociRoACH was placed in the full exoskeleton (following the procedure in Figure 3.9), and then run over both poppy seeds and shallow water.

First, the robot ran for 5 min at full motor power through a 2.5 cm thick layer of poppy seeds. Approximately 6 grams of poppy seeds accumulated in the structural shell of the robot, but no seeds were inside the flexible shell.

Next, VelociRoACH ran in place for 3 min in a container filled to a height of 1 cm with water. The electronics and SCM mechanisms survived the test. However, some water droplets were observed inside the flexible shell and there was some wetting of the lower cardboard structures. Upon inspection after the test, the bag layer appeared to have small perforations from the leg clips that allowed water to enter. From a separate evaluation of

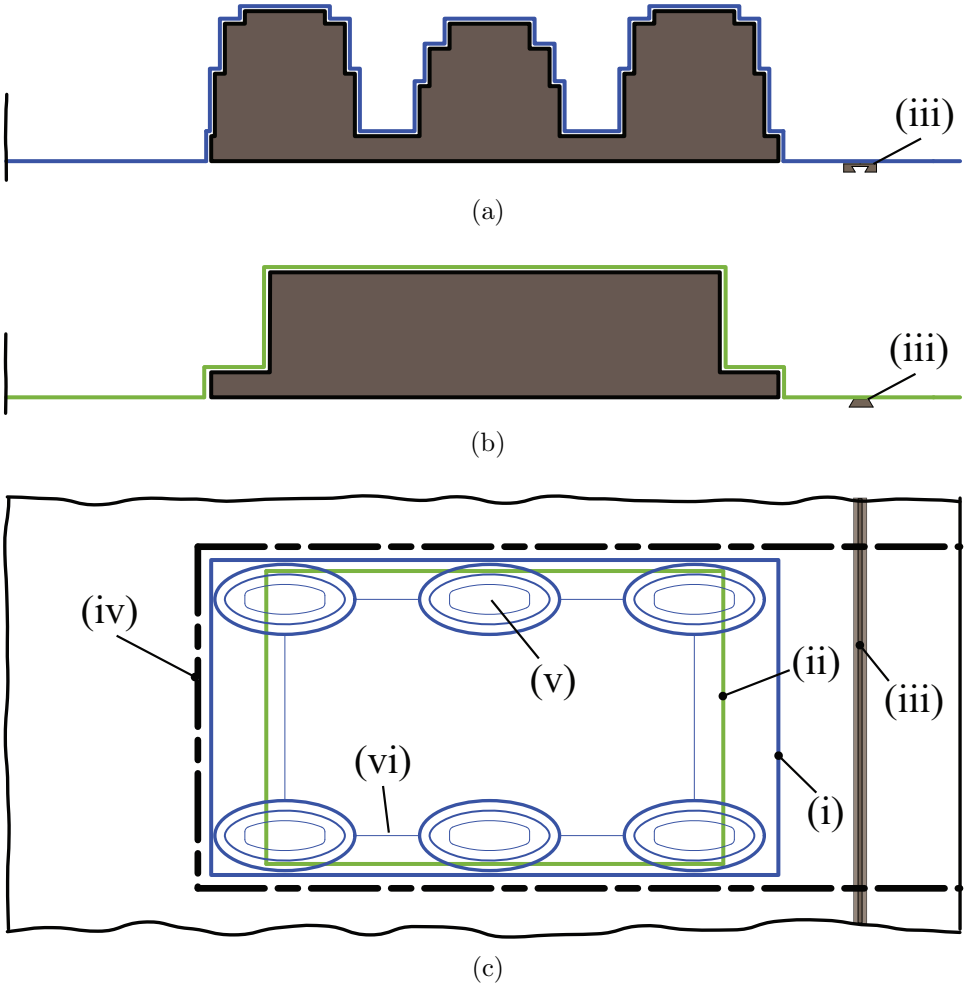
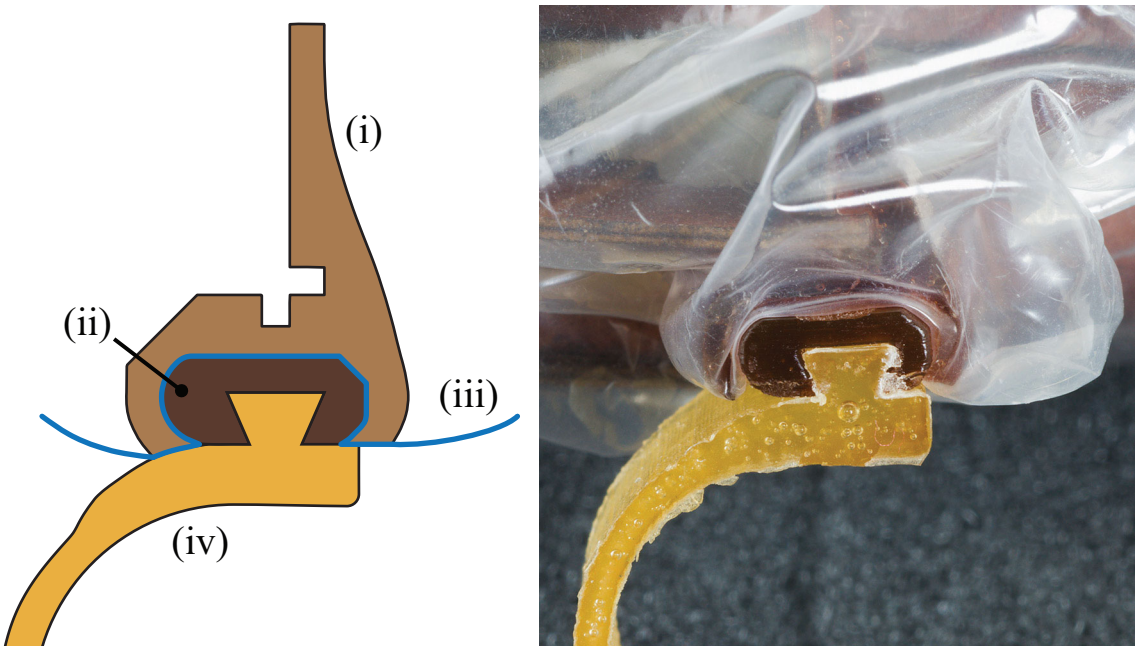


Figure 3.3: Sealed flexible shell manufacturing process. (a) Side view: forming of the bottom bag layer with protrusions for freedom of leg motion. (b) Side view: forming of the top bag layer. (c) Underside view: bag layer assembly with details (i) bottom piece of the bag, (ii) top piece of the bag, (iii) joining "ziploc" zipper on the bag, (iv) heat welds at the edge of the two layers, (v) formed out-of-plane pockets, shown topologically in this view, and (vi) extra vertical webs that unavoidably form in the contoured bag layer between peaks, due to the high aspect ratio of the mold.



(a) (b)

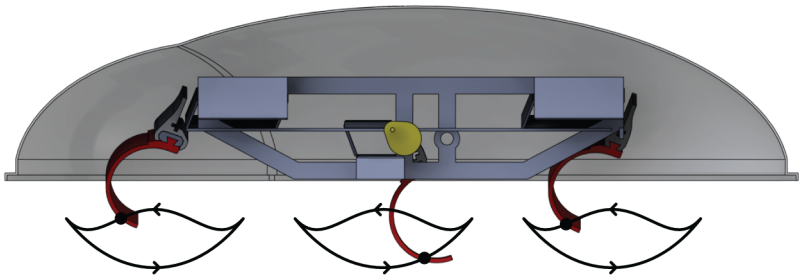
Figure 3.4: Leg mounts that clip through the flexible shell. (a) Diagram with details (i) half of the leg mount is attached to the robot hip inside the bag layer, (ii) the other half of the leg mount is outside the bag layer and snaps into the inner component, (iii) bag layer wedges between the two leg mount halves, and (iv) VelociRoACH legs slide into dovetail connections on the outer component. (b) Close-up of molded leg clips capturing the sealing bag on the robot.

the zipper, it admits some water when submerged in shallow water, so it is another potential source of failure of the water seal.

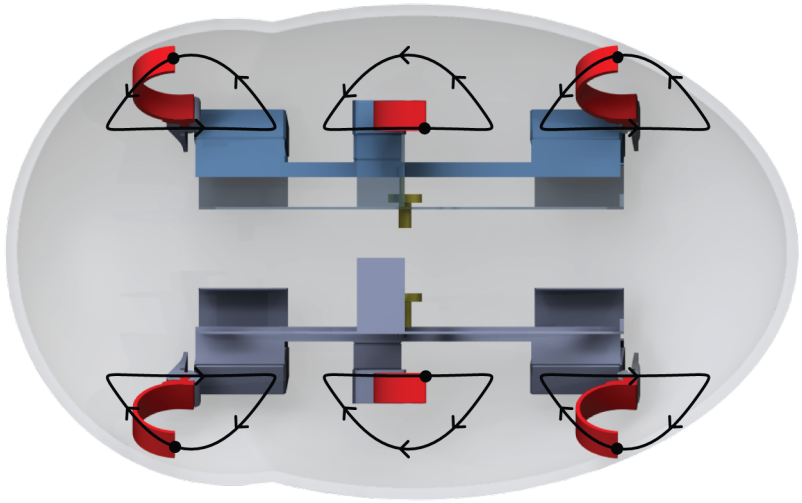
To fully waterproof the robot, we would omit the zipper and fully heat seal the robot into the bag. This comes at the cost of the re-usability of the flexible shell. In addition, we would need to place shielding materials such as rubber or foam at any sharp interfaces that could potentially perforate the bag.

3.3 Structural Shell for Impact Protection

The structural layer of the exoskeletal shell is designed to reduce the shock imparted to the robot by impacts while satisfying the constraints that it fits around the robot structure and that it does not interfere with the motion of the legs.



(a)



(b)

Figure 3.5: (a) Side view and (b) underside view of solid model renderings of VelociRoACH assembled in the structural shell. The structural shell clears the leg motion of the robot.

3.3.1 Design

The structural shell is split into a bottom and top section that are thermoformed separately. The top shell (shown in Figure 3.5) is designed such that it does not interfere with the VelociRoACH's SCM linkages. This leaves the design space mostly open. We chose an ellipsoidal shell shape, which is terradynamically streamlined to enable a passive roll motion during the traversal of cluttered terrain [91], while being capable of absorbing impact from high-speed collisions.

Shown in Figure 3.5, a kinematic model of the VelociRoACH transmission was used to trace out the trajectories of the leg tips of the robot. These trajectories are used in conjunction with the solid model geometry to shape the shell volume such that there is no interference of any mechanisms or leg with the shell. During this process, a secondary ellipsoidal bulb was added to the front shell volume to clear the forward part of the front

leg stroke. The top shell also needs an interface to the bottom shell. We chose to use an integrated snap-fit ring along the bottom edge of the top shell. This approach has the advantage that it is reclosable, and requires no adhesives. On the top shell, this feature is accomplished with an outwardly protruding lip which is shown in Figure 3.5a.

Shown in Figures 3.7 and 3.8, the bottom shell requires more complicated geometry than the top shell. It incorporates an undercut lip which retains the protruding lip of the top shell. It also has material cut away to allow pass-through of the legs. The bottom shell was designed to have these features be cuttable with an infrared laser. The limited focal range of the laser cutter limits the curvature of the bottom shell, so it must be mostly flat.

The primary function of the thermoformed structural shell is to mitigate impact shock. Therefore, after designing the shape of a structural shell to fit the form and kinematics of the robot, the stiffness of the shell needs to be tuned to absorb impacts. Assume the robot is dropped with its legs pointed upwards from a vertical height h and impacts the ground with a linear spring of stiffness k producing the impact force. The robot impacts the ground with velocity $v_{imp} = \sqrt{2gh}$ from conservation of energy (with acceleration due to gravity g) and the force during impact F_{imp} is given below from Newton's second law:

$$F_{imp} = ma_z = k\Delta z, \tag{3.1}$$

where m is the robot mass, a_z is the vertical acceleration during impact, and Δz is the spring deflection during impact. To determine the maximum acceleration $a_{z,max}$ during impact, conservation of energy is applied from the instant before impact with the robot traveling at v_{imp} to the instant that the robot reaches zero velocity with maximum spring deflection Δz_{max}:

$$\frac{1}{2}mv_{imp}^2 = \frac{1}{2}k\Delta z_{max}^2, \tag{3.2}$$

where it is assumed that the maximum spring force is significantly greater than the weight of the robot. Now, solving (3.2) for Δz_{max} and plugging the result in for Δz in (3.1), with $a_z = a_{z,max}$ and $v_{imp} = \sqrt{2gh}$ yields:

$$a_{z,max} = \sqrt{\frac{2kgh}{m}} = \sqrt{\frac{CEbt^3gh}{2mL^3}}, \tag{3.3}$$

where the right hand side expression results from applying the assumption that the effective spring of the shell is modeled by a rectangular cantilever beam undergoing small deflection, with effective stiffness $k = \frac{3CEI}{L^3}$ and area moment of inertia $I = \frac{bt^3}{12}$. In these expressions, E is the Young's modulus of the shell material, b is the overall width of the shell structure, t is the shell thickness, L is the overall length of the shell structure, and C is a constant that accounts for stiffening effects of the top shell's ellipsoidal curvature and the bottom shell's structural ribs. The rectangular cantilever beam assumption comes from the observation that the shell shown in the side view in Figure 3.5a is anchored at the bottom of the robot chassis, which means forces applied vertically downward to the top shell deflect the flat bottom shell similarly to a cantilever beam.

If we assume that b, L, and m are set by the robot in the exoskeleton, then E and t are the design parameters to adjust the shell stiffness to bring the impact acceleration below a target value. The elastic moduli of thermoformable polymers are largely constant, and prescribing the stiffness of the shell by material choice limits the design space. A material of the right stiffness may have sub-optimal attributes in other areas, such as impact resistance, formability, or laser machine-ability. We chose polycarbonate for the shell because it excels in these areas and we tuned the shell's stiffness with geometric design.

With the material fixed, tuning the shell thickness t is an effective way to minimize the impact acceleration, because the peak acceleration $a_{z,max}$ scales with $t^{3/2}$. Additional considerations that need to be made when adjusting shell thickness are that the added mass of the shell increases linearly with t, and that the shell may bottom out against the robot body during impact if it falls below a stiffness threshold, which can increase the peak impact acceleration. Another option to increase stiffness is by adding structural ribs to the top and bottom structural shells.

3.3.2 Manufacturing

The top shell mold was made with a 3D printer (*Ultimaker* 2) because of the precision required for the outwardly protruding lip that snaps into the receiver lip on the bottom shell. The 3D printed mold is made of PLA plastic with a 3 mm hull that is filled at a 30% volume rate. This build setting produced an excessively strong mold, and the hull thickness and fill rate could be reduced to reduce build time. A diagram of a thermoformed top structural shell is shown in Figure 3.6. Polycarbonate of 250 μm sheet thickness was heated for 25 s before being formed over the top mold.

The bottom structural shell manufacturing process is shown in Figure 3.7. The overhead and cross-section diagrams of the thermoformed bottom shell (Figure 3.7a and 3.7b) show the structural ribs, vacuum feeds, undercut lip, and alignment pins in the mold. Because the bottom shell is mostly planar, all three layers of the mold are made of laser-cut acrylic—the base and middle layers are 6.35 mm thick and the top layer is 3.18 mm thick. The base layer of the mold contains laser-etched channels (using a *VersaLaser* VL-200 with raster setting, 80% power, 12% speed) that are approximately 1.6 mm deep. When the polycarbonate is formed over the mold, the channels form stiffening ribs into shell. As a general process guideline, the width of the ribs should be at least twice their depth in to fully form. Vacuum feeds are cut through the base layer around the outermost edge and along the center of the rib trenches to sufficiently form the undercut lip and rib features. The vacuum feeds are cut without forming any closed curves to ensure the base mold layer remains a single piece. The middle layer of the mold defines the outer extent of the undercut lip and stacks over and aligns to the base layer using 3.18 mm diameter aluminum alignment pins that are anchored in the base layer. The top layer of the mold defines the inner extent of the undercut lip and is placed over the middle layer using the same alignment pins. The middle and top plates are split along a line of symmetry to release the shell after forming.

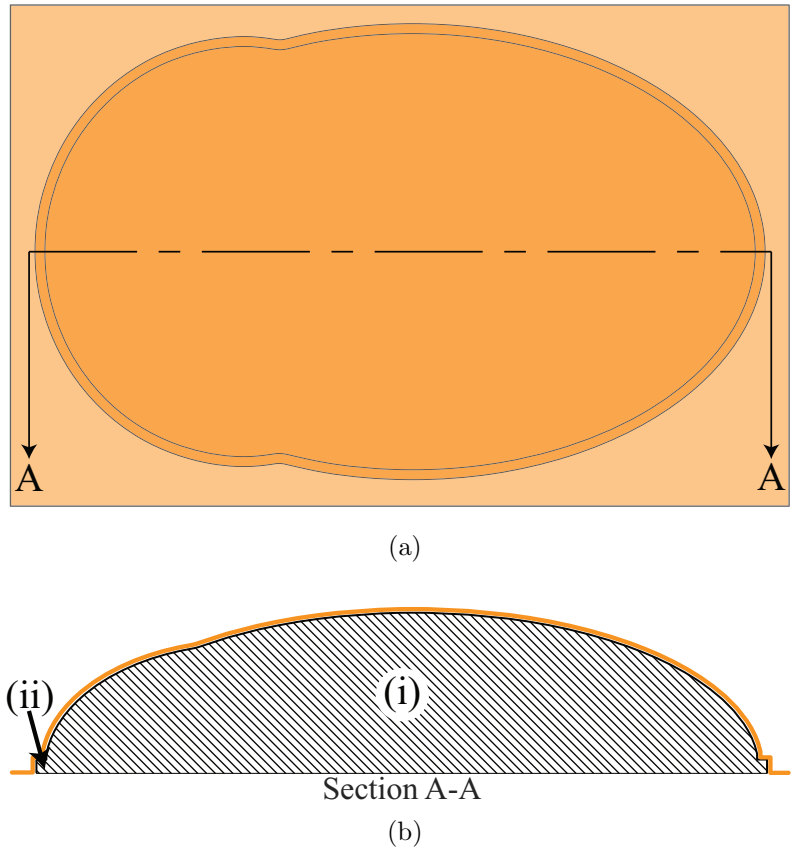


Figure 3.6: (a) Top view and (b) side section view of the thermoformed structural top shell over a 3D printed mold. (i) 3D printed PLA plastic ellipsoidal form with a 3 mm hull and 30% fill. (ii) Outwardly protruding lip at the base.

The bottom structural shell is made by thermoforming the 250 μm polycarbonate sheet into the bottom mold using the same process time as for the top shell. The uncut bottom shell is released from the mold (Figure 3.7c) by roughly cutting around the top layer of the mold outward of the alignment pins, pulling the base plate with dowel pins downward, and then pulling the middle and top plates outward along their parting line.

As a final process step, the roughly cut bottom shell is precisely cut using a laser cutter (Figure 3.7d). The parts of the bottom shell that were thermoformed over the protruding alignment pins are snapped over alignment pins in a matching laser cutting jig plate. With the top left corner of the jig plate as a coordinate reference in the laser bed, the laser cutter is used to cut outlines around the receiver lip and the through holes for the legs. The laser is focused to the flat top layer of the formed shell. The cut settings for the leg holes (10% power, 2.5% speed) are twice the power of those used for the receiver lip (5% power, 2.5% speed) because the bottom of the shell is not in the range of focus for the laser. Images of the bottom shell mold, thermoformed shell before precise cuts, and final bottom shell after

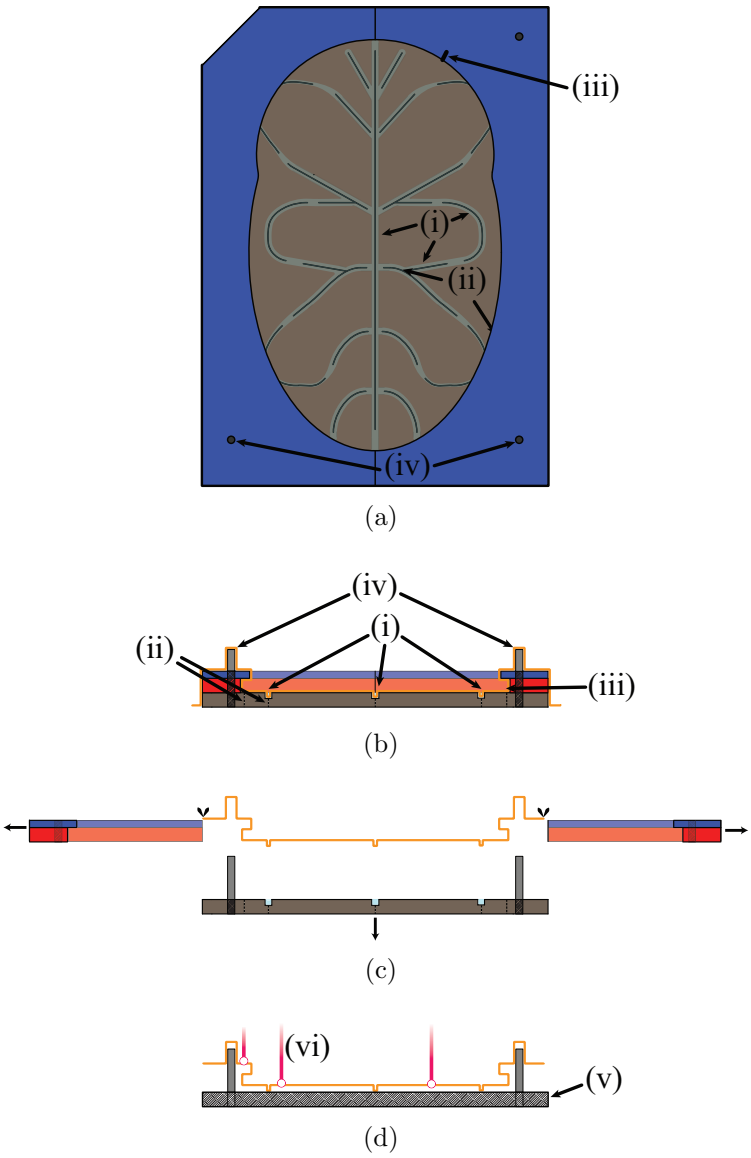


Figure 3.7: Bottom structural shell manufacturing process: (a) Overhead view of multi-layer laser cut mold. The pattern in the bottom layer will form the structural ribs (i) and thin cuts provide vacuum feed (ii). The top plate of the mold forms the undercut lip feature (iii). Alignment pins (iv) are added to stack up the mold layers. (b) Cross section view of thermoformed plastic shell in mold, where the undercut lip (iii) formed by separate layers of the mold is shown. (c) To release the formed shell, the shell is roughly cut around the top layer of the mold, the base plate with dowel pins is pulled downwards, and the top two plates defining the undercut lip are pulled outward. (d) The roughly cut shell is aligned to a fixture plate (v) for laser cutting which duplicates the alignment pin pattern as in the stack-up above, and then holes for legs and final outline release cuts are made (vi).



Figure 3.8: Images of the bottom shell mold, thermoformed bottom structural shell, and finished bottom shell after release cuts.

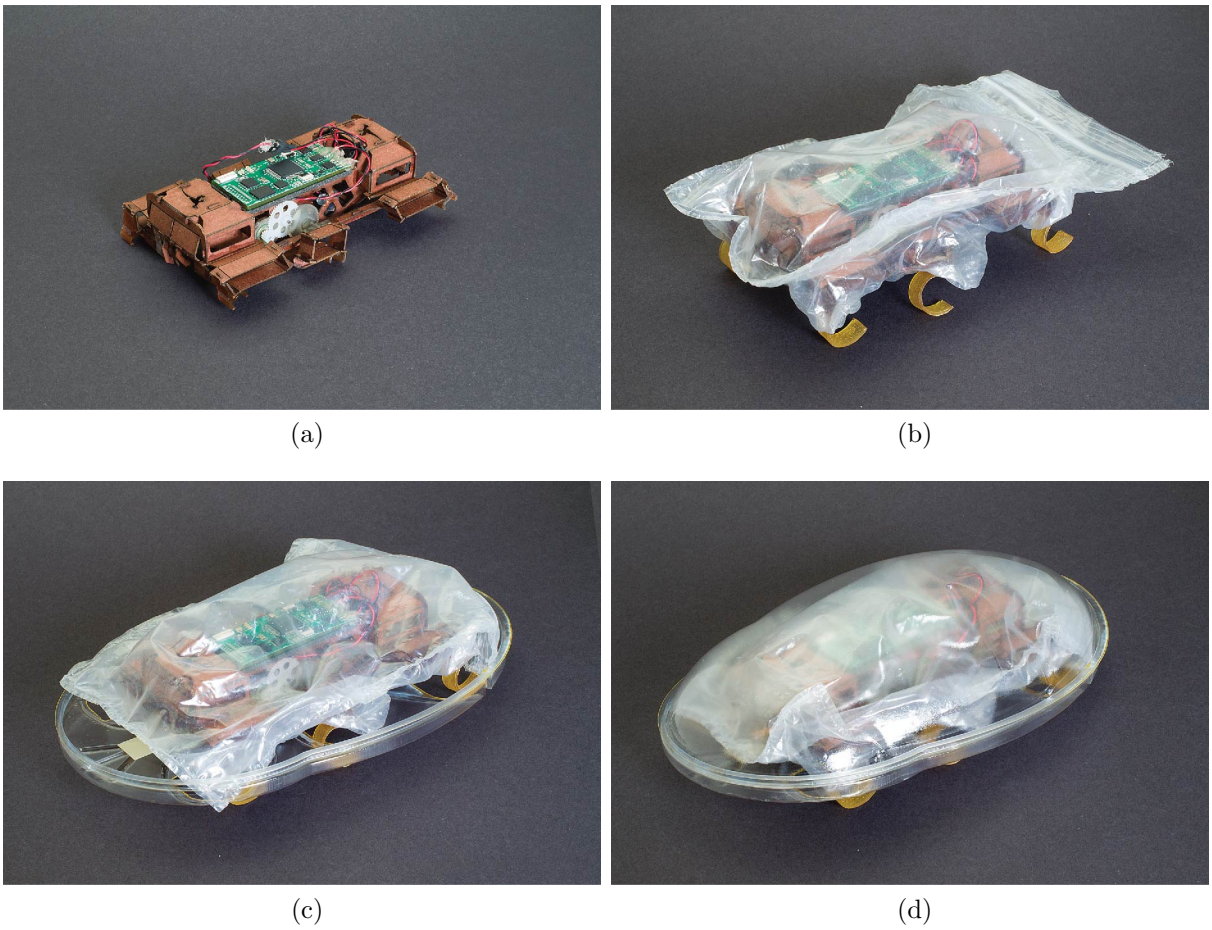
precise cuts are shown in Figure 3.8.

3.3.3 Assembly and Integration With Flexible Shell

We show assembly of a VelociRoACH into the flexible and structural components of the exoskeletal shell in Figure 3.9. Each assembly step is reversible by design, so that it is possible to remove the robot from the shell for maintenance. Assembly order begins with the folded cardboard robot chassis as shown in Figure 3.9a, with actuators and control board installed, and molded leg clip receivers attached to the hips. In Figure 3.9b, the body is inserted into the flexible shell, which is then sealed at the anterior with the "ziploc" strip bonded into the bag. The legs are clipped onto the leg clip receivers through the bag layer as detailed in Figure 3.4. In Figure 3.9c the bottom structural shell is adhered to the underside of the sealing bag, and in Figure 3.9d, the top structural shell is snapped into the rim feature of the bottom shell.

3.3.4 Characterization

As an evaluation of the structural shell, the robot was assembled in the shell following the steps in Figure 3.9 and dropped from various heights. After initial tests demonstrating structural damage to the robot and the failure of the snap fit between the top and bottom shells from drop heights as low as 3 m, a layer of foam (1.6 g) was added between the top of the robot and the top structural shell. With the addition of this shock absorbing component, the robot with exoskeleton remained undamaged and intact after two successive drops from four stories (12 m) with a top-first impact orientation (the robot in the shell preferentially falls top-first due to aerodynamic effects). The SCM structures, transmission, and electronics of the robot sustained no damage. To assess damage, the robot's components were inspected visually for any signs of fracture of plastic components, tearing of flexures, or failure of glue joints. The functionality of the robot was then tested by commanding it to run forward. In addition, the snap fits of the segmented leg mounts and structural shell remained secure in place after the drops. However, the battery connection was lost upon impact and after bouncing, the robot did not land on its feet in one of the trials.



(a) (b)

(c) (d)

Figure 3.9: Assembly process for adding exoskeletal shell to the robot: (a) cardboard robot body, (b) with flexible shell and mounted legs, (c) with bottom structural shell, and (d) complete with top structural shell.

3.4 Performance Trade-Offs of Exoskeletal Shell

Although the robot exoskeleton offers improvements in locomotion over granular media and impact resistance, it also comes at some cost. VelociRoACH in the exoskeletal shell could run on flat carpet at 1.1 m/s, which is 40.7% of the top speed of the unencumbered robot [43]. The shell adds a total of 13.5 g of mass (10.7 g structural layer, 2.7 g bag layer) to the 30.1 g robot (with battery and board). Also, the shell increases the length by width by height dimensions of the robot from 10 cm $\times$ 7 cm $\times$ 4.5 cm to 18.5 cm $\times$ 12 cm $\times$ 5.3 cm.

Chapter 4

Design of a High-Payload Folded Legged Millirobot

In order for folded millirobots to be mission-ready in challenging environments, they need to carry significant payloads. Depending on task specialization, this extra payload can be dedicated to battery power, additional actuation, sensing, or protection from the environment. This chapter describes the motivating challenges of supporting heavy loads with folded structures and details the design of LoadRoACH, a high-payload folded legged millirobot that can carry shell and active tail payloads for increased robustness and mobility across a variety of terrain types.

4.1 Limitations of Prior Folded Legged Millirobots

At small scales (feature size of several hundred microns, overall size scale of a few centimeters), folded microrobots fabricated using SCM suffer from unfavorable scaling of battery and control electronics, making it difficult to create a fully autonomous system. As the scale increases to that of folded millirobots (feature size of several millimeters, overall size scale of 10–20 centimeters), batteries, sensors, and microcontrollers are widely available for autonomous operation, and the challenge becomes creating structures that can withstand the forces from running locomotion and impacts after falls. These millirobot systems still have strict payload budgets. With a palm-sized footprint and typical masses of 30–100 grams, system payloads that increase battery capacity or available motor power, provide additional actuated degrees of freedom, add mechanical robustness, and increase sensor information must be weighed against each other in the available payload budget. In the following subsections, scaling analyses following dimensional analysis techniques [33] are performed that demonstrate how flexure peel loading, flexure mechanism load transmission, and impact force from a terminal velocity fall unfavorably scale as a robot's length scale isometrically increases and payload is added relative to the base robot platform. These scaling analyses motivate the development of a palm-sized folded millirobot with improved mechanical robustness.

4.1.1 Scaling of Flexure Peel Loading

Legged SCM robots such as VelociRoACH [43] and X2-VelociRoACH [42] have demonstrated peeling failure at flexural joints under high loading conditions. Peel strength (force per unit length of bonded material) is the material limit that quantifies this failure mode. Peeling failure occurs at flexures that form kinematic joints, and it can either be a failure of the adhesive between the flexural and structural layers of the composite or an internal failure of the structural material (i.e. internal delamination of cardboard plies). To evaluate whether larger, heavier SCM robots are more susceptible to flexure peeling failure, the force loading of legged running per unit flexure length must be determined and compared to the peeling strength. The following scaling analysis applies the dynamically similar running scaling laws of a Spring Loaded Inverted Pendulum model of legged running used by Haldane et al. to design VelociRoACH [43].

There are two cases of interest for analyzing the limitations of scaling folded robots. The first case is isometric scaling, in which length scales with fundamental length l, area with l^2, and volume with l^3. The second case is added payload scaling, in which the fundamental length scale of the system remains constant, but the mass m increases sublinearly with the payload added to the robot. The total mass is $m = m_{robot} + m_{payload}$, and the added payload scaling analysis considers how quantities of interest scale with respect to m.

In the first case of isometric scaling, length scales with l, mass scales with l^3, and running frequency scales with $l^{-1/2}$. Based on the mass [M], length [L], and time [T] dimensions of the peak ground reaction force F_{run} [MLT^{-2}], with time inversely proportional to running frequency, the following scaling relation holds:

$$F_{run} \sim l^3. \tag{4.1}$$

In the second case of added payload scaling, length is constant, running frequency is constant, and mass m increases sublinearly with the added payload. Therefore, the peak ground reaction force F_{run} scales proportionally with mass:

$$F_{run} \sim m. \tag{4.2}$$

If loads proportional to F_{run} propagate flexure peeling failures, then the peel loading per unit flexure width $\gamma_{peel} \sim \frac{F_{run}}{l}$ must exceed a material limit. Assuming fixed construction of the robot's SCM structures, the peel loading scales as follows:

$$\gamma_{peel} \sim l^2 \sim m^{2/3} \tag{4.3}$$

$$\gamma_{peel} \sim m, \tag{4.4}$$

where (4.3) gives the peel loading relation for the first case of isometric length scaling and (4.4) gives the peel loading relation for the second case of added payload scaling. Therefore, unless the adhesive bonds between the flexures and structures of an SCM robot design are strengthened, there will be a point past which normal running loads will cause peeling failure if the SCM robot is isometrically scaled in length or has payload added to it. Because

isometric length scaling increases the width of all flexures while added payload scaling keeps the same base robot design, the peel loading γ_{peel} scales less favorably for added payload scaling ($\gamma_{peel} \sim m$) than for isometric length scaling ($\gamma_{peel} \sim m^{2/3}$).

Later in this chapter, material and process improvements to SCM for palm-sized robots are presented that eliminate flexure peeling failures that occur if existing platforms such as VelociRoACH [43] and OctoRoACH [112] have significant payloads added to them.

4.1.2 Scaling of Flexure Mechanism Load Transmission

At small scales, folded robots designed using SCM or similar flexure-based fabrication processes operate under the assumption that the flexures act as ideal hinges, which only rotate about the hinges and are orders of magnitude stiffer in other loading directions. However, as robots increase in length scale and carry heavier payloads, robot designs need to consider significant deflections of mechanisms away from intended appendage paths. For legged robots, this corresponds to mechanism deflections causing legs to splay outwards or fail to pick up off the ground, resulting in ineffective running gaits.

Hoover and Fearing developed a flexure compliance analysis approach based on an Euler-Bernoulli beam model with linear elasticity, three directions of linear displacement, and three directions of angular displacement [55]. By composing the compliance matrices of serial and parallel flexures, the resulting strain energy in the desired deflection direction under multi-axis loading can be compared to the overall strain energy, which gives a metric for a folded mechanism's effectiveness in transmitting force in the desired direction. For example, a Sarrus straight-line linkage can be stiffened against off-axis loading through the addition of redundant parallel linkages mounted at certain angles relative to each other.

For the RoACH family of legged robots, including DynaRoACH [54], OctoRoACH [112], VelociRoACH [43], and LoadRoACH, the new robot platform developed in this dissertation, the legs are driven by coupled orthogonal planar linkages. In the transverse plane, a slider-crank linkage causes adduction and abduction of the legs, with flexures oriented along the fore-aft direction. In the sagittal plane, a four-bar linkage causes protraction and retraction of the legs, with flexures oriented laterally. During forward legged running, RoACH robots generate significant vertical and fore-aft forces. The fore-aft forces cause shear loading of the slider-crank flexures during stance phases. If the legs contact the ground during swing phases, the vertical forces cause shear loading of the four-bar flexures and compressive loading of the slider-crank flexures.

The following analysis explains the unfavorable scaling of the load transmission of a flexure-based leg drive mechanism under high off-axis loading. Assume that a kinematic flexure designed to rotate about its width axis is being loaded in the shear direction along its width, and that displacements in the shear direction past a certain threshold cause ineffective leg propulsion. Assuming the flexure acts as a linear elastic cantilever beam with small deflection and has Young's modulus E, width w_{flex}, length l_{flex}, and thickness t_{flex}, its shear stiffness is $k_{shear} = \frac{E w_{flex}^3 t_{flex}}{4 l_{flex}^3}$. Now, assume that the three length dimensions of the

flexure scale linearly with overall length scale l. Then the shear stiffness scales with length as $k_{shear} \sim l$.

From the assumptions of the previous subsection, the maximum ground reaction force during running scales with isometric length scaling according to $F_{run} \sim l^3$ and with added payload scaling according to $F_{run} \sim m$. To relate this running force to shear deflection δ_{shear}, the following Hookean relation is applied:

$$\delta_{shear} \sim \frac{F_{run}}{k_{shear}}. \tag{4.5}$$

Now, to normalize the effect of the off-axis shear deflection of the mechanism across length scales, the angular deflection for small displacements $\theta_{shear} = \frac{\delta_{shear}}{l_{moment}} \sim l$ is analyzed, where l_{moment} is the moment arm from the point of force application to the flexure.

Combining the previous scaling relations, the resulting scaling relation of the angular deflection of a flexure loaded off-axis in shear is:

$$\theta_{shear} \sim l \sim m^{1/3} \tag{4.6}$$

$$\theta_{shear} \sim m, \tag{4.7}$$

where (4.6) gives the angular deflection relation for the first case of isometric length scaling and (4.7) gives the angular deflection relation for the second case of added payload scaling. The off-axis angular deflection of a flexure loaded in shear increases proportionally to isometric length scale ($\theta_{shear} \sim l \sim m^{1/3}$) and to the mass of the robot platform with added payload ($\theta_{shear} \sim m$). Therefore, to maintain effective running performance, flexures of folded robots at large scales and with high payload need to be stiffened in off-axis loading directions relative to smaller and low-payload designs. Additionally, the flexure topology of the mechanism can be changed to avoid the low off-axis stiffness of flexures placed in series.

In the design of the VelociRoACH legged robot, there is a significant reduction in off-axis mechanism stiffness compared to the bulk flexure stiffness due to the serial compliance of a slider-crank mechanism for hip abduction/adduction, an orthogonal four-bar mechanism for leg protraction/retraction, and a planarizing four-bar linkage that allows the mechanism to be driven by a single crank [43]. In preliminary running tests with VelociRoACH carrying additional payload, the ideal leg paths of the drive mechanism were not maintained under high payloads due to vertical mechanism deflections, causing the legs to drag against the ground during designed leg recirculation phases of the gait. These observations motivated the mechanism redesign and flexure stiffening changes to VelociRoACH that led to the design of LoadRoACH.

4.1.3 Scaling of Terminal Velocity Impact Force

Legged SCM robots in search and rescue scenarios encounter obstacles (including collapsed building faces, piles of rubble, and stairways) that are many times larger than an individual robot's length scale, which can result in falls from substantial heights. This subsection

analyzes how the impact force that a robot withstands after a terminal velocity drop scales with increases in size and added payload.

The maximum impact force that a falling robot experiences is after an impact at terminal velocity. From a force balance of a robot falling vertically with gravity and form drag acting on it, terminal velocity v_{term} is reached when these forces are equal:

$$mg = \frac{1}{2}\rho C_D A v_{term}^2, \tag{4.8}$$

where m is the robot mass, g is gravitational acceleration, ρ is the density of air, C_D is the drag coefficient of the falling robot, and A is the projected area perpendicular to the fall direction. Solving (4.8) for v_{term} produces the terminal velocity expression:

$$v_{term} = \sqrt{\frac{2mg}{\rho C_D A}}. \tag{4.9}$$

Again, the scaling analysis is performed for two cases: in the first case, length is scaled isometrically and in the second case, the length scale remains fixed while mass scales sublinearly with added payload. In the first case, $m \sim l^3$ and $A \sim l^2$ while g and ρ are length scale invariant. Although C_D can vary significantly as the Reynolds number ($Re \sim v_{term} l$) changes, the assumption is made that the form of the robot can be changed to maintain constant C_D. This results in the terminal velocity scaling relation $v_{term} \sim l^{1/2}$. In the second case, m scales sublinearly with added payload and A remains fixed (g, ρ, and C_D remain constant under added payload scaling), so the terminal velocity scales according to $v_{term} \sim m^{1/2}$.

Now, assume the robot undergoes an elastic ground impact and a linear spring with coefficient k produces the impact force. Conservation of energy from the point immediately before the impact to the rebound instance during impact with maximum spring deflection Δz_{max} (assuming negligible changes in gravitational potential energy) results in the following relation:

$$\frac{1}{2}k\Delta z_{max}^2 = \frac{1}{2}m v_{term}^2. \tag{4.10}$$

Because of the linear spring assumption, the maximum spring deflection is $\Delta z_{max} = \frac{F_{imp}}{k}$, where F_{imp} is the maximum force during impact. Substituting this expression for Δz_{max} into (4.10) results in the following impact force expression:

$$F_{imp} = v_{term}\sqrt{km}. \tag{4.11}$$

Assuming a compliant structural shell protects the robot from impact, a reasonable simplified model of the spring is a rectangular cantilever beam with small deflection. For this spring model, the stiffness is $k = \frac{Ewt^3}{4L^3}$, where E is the elastic modulus of the beam, w is the beam width, t is the beam thickness, and L is the beam length. In the first case, all dimensions of the spring scale linearly with overall length scale l and $k \sim l$. Also, the mass scales

according to $m \sim l^3$. In the second case, k remains constant and m scales sublinearly with added payload. Thus, the impact force relation (4.11) scales as follows:

$$F_{imp} \sim l^{5/2} \tag{4.12}$$

$$F_{imp} \sim m, \tag{4.13}$$

where (4.12) gives the first case and (4.13) gives the second case.

To predict whether the robot will sustain damage after a terminal velocity impact, F_{imp} must be compared to a material failure limit. Assume the breaking stress of the weakest part of the robot is σ_{break}. Then the maximum force that the robot can withstand F_{break} scales with l^2 in the case of isometric length scaling and remains constant in the case of added payload scaling.

Finally, the ratio of impact force to breaking force can be determined for each scaling case:

$$\frac{F_{imp}}{F_{break}} \sim l^{1/2} \sim m^{1/6} \tag{4.14}$$

$$\frac{F_{imp}}{F_{break}} \sim m, \tag{4.15}$$

where (4.14) gives the relation for isometric length scaling and (4.15) gives the relation for added payload scaling. Therefore, without designing structures to protect a robot against impacts, the force from terminal velocity impacts will break robot structures if isometric length increases or payload additions surpass an upper threshold. Impact resilience scales much less favorably for added payload scaling ($\frac{F_{imp}}{F_{break}} \sim m$) compared to isometric length scaling ($\frac{F_{imp}}{F_{break}} \sim l^{1/2} \sim m^{1/6}$). This consequence of scaling limits the paths that a large, heavy robot can take in a search and rescue mission because it will be less robust to drops.

The scaling of terminal velocity impact force relative to a material limit can be compared to the scaling analysis of animal robustness to collisions by Jayaram et al. [62]. In their analysis, the authors showed that the specific kinetic energy ($v^2/2$, units of J/kg) of vertebrate runners scales according to $m^{1/3}$, which closely matches an inverted pendulum locomotion template. Therefore, smaller animals are subjected to lower energy impacts relative to their mass. In addition, the specific energy that biological and engineering materials can absorb (based on a characteristic elastic-plastic fracture toughness and geometric scaling of isotropic materials) scales according to l^{-1} or $m^{-1/3}$. Finding the intersection of these two relations yields a fundamental size scale limit termed the Haldane limit ($m = 1$ kg for vertebrate runners). For animals with masses above the Haldane limit, kinetic energy of forward running cannot be fully dissipated without causing irreversible plastic deformation. Thus, these animals need to actively avoid obstacles and gradually slow to a stop to avoid structural damage. The palm-sized robots in this dissertation have masses that are well below the Haldane limit, so they should not sustain damage from running into obstacles. However, terminal velocity falls are significantly more energetic, with specific kinetic energy $v^2/2$ that scales with m as payload is added to a robot, compared to the $m^{1/3}$ relation of

inverted pendulum running. The mass threshold for sustaining terminal velocity impact damage should therefore be lower than the Haldane limit.

Protective exoskeletal structures integrated into the design of folded legged millirobots, as described in Chapter 3, can mitigate the unfavorable scaling of impact force relative to material strength.

4.1.4 Payload Carrying Comparison of Folded Legged Robots

The high-payload folded legged millirobot LoadRoACH is compared to prior robots in Table 4.1. The first three columns give the name of the robot, its overall mass, and its overall length. For robots that carry a payload, the next two columns give the payload description and additional mass of the payload. The rightmost column gives the fastest reported forward running speed for the robot and payload combination.

The first group of rows gives the payload carrying capability of VelociRoACH-based legged robot designs with a base mass of 30 g and an overall length of 10 cm. These iterations include SailRoACH with an aerodynamic tail [83], VelociRoACH carrying the ornithopter H^2Bird [114], VelociRoACH with a protective shell [40], and TAYLRoACH with an inertial tail [82]. With payload masses of 14–18 g, VelociRoACH-based robots running under payload have forward speeds of 100–220 cm/s, compared to the unloaded running speed of 250 cm/s. These VelociRoACH iterations have comparable drive motor power output and SCM construction, so variations in running performance depend on the mass distribution and aerodynamic effects of the payloads.

The second group of rows gives two data points for the payload carrying capability of DASH-based legged robots, with an overall length of 10 cm. The original DASH platform [9] has a mass of 16 g and runs forward at 150 cm/s with no added payload. Jung et al. used a commercial version of the DASH robot platform with an overall mass of 33 g (*DASH Robotics*) and incorporated a jumping module into the chassis, which adds a payload of 26 g. This version of DASH was able to run forward at a speed of 56 cm/s. Note that these DASH platforms have comparable drive motor power output and SCM construction to VelociRoACH.

The third group of rows gives multiple data points for the payload carrying capability of Very Large RoACH (VLR), which is a 150 g, 1.6x length scale version of VelociRoACH with a load decoupling platform. Under high payload running, the load decoupling platform drags against the ground, which reduces the loading at the legs. As shown in Table 4.1, VLR's unloaded speed of 19 cm/s decreases to $\{13, 10, 6\}$ cm/s as $\{100, 200, 300\}$ g of payload is added. Note that VLR operates with tethered power. VLR carries higher payloads relative to body weight when compared to the other robot platforms, but runs with significantly slower running speed.

LoadRoACH, the folded millirobot presented in this thesis, has a higher overall mass (54.8 g) compared to VelociRoACH and DASH because of its dual-output double crankshaft transmission for more robust force transmission under heavy loading. LoadRoACH also uses a dual flexure material construction of PET and nylon, which combines the benefits of

Table 4.1: Comparison of folded legged robots with payload

Robot	Mass (g)	Length (cm)	Payload description	Payload mass (g)	Speed (cm/s)
VelociRoACH [43]	30	10	None	0	250
			Aerodynamic tail [83]	15	220
			Ornithopter [114]	15	150
			Protective shell [40]	14	110
			Inertial tail [82]	18	100
DASH [9]	16	10	None	0	150
Commercial DASH	33	10	Jump module [65]	26	56
Very Large RoACH† [142]	149	16	Metal weights	0	19
				100	13
				200	10
				300	6
LoadRoACH [18]	54.8	10	Shell and tail	27.2	72

†Tethered power

each material. PET provides high stiffness to off-axis loading, which increases proportional to payload. Nylon provides high tear strength, which helps the robot's kinematic flexures survive impacts. With protective shell and active tail payloads (27.2 g of added mass), LoadRoACH can run at 72 cm/s (29% of VelociRoACH's unloaded speed). LoadRoACH can carry heavier payloads than the other robot platforms based on VelociRoACH and DASH with comparable drive motor power, and can run 29% faster than DASH with a jump module, which carries a similar payload. In addition, the 82 g overall mass of LoadRoACH with shell and tail payload is 39–86% heavier than the total mass of the other palm-sized legged robots with added payload. The remainder of this chapter describes the design details of LoadRoACH that enable it to run with heavy payloads.

4.2 Design Details of LoadRoACH

LoadRoACH (pictured in Figure 4.1) is a new addition to the RoACH family of robots that maintains the SCM construction, dynamic gait, and differential leg drive of VelociRoACH [43] while improving its load capacity. LoadRoACH carrying a shell and tail payload was used in the tailed turning experiments in Chapter 6.

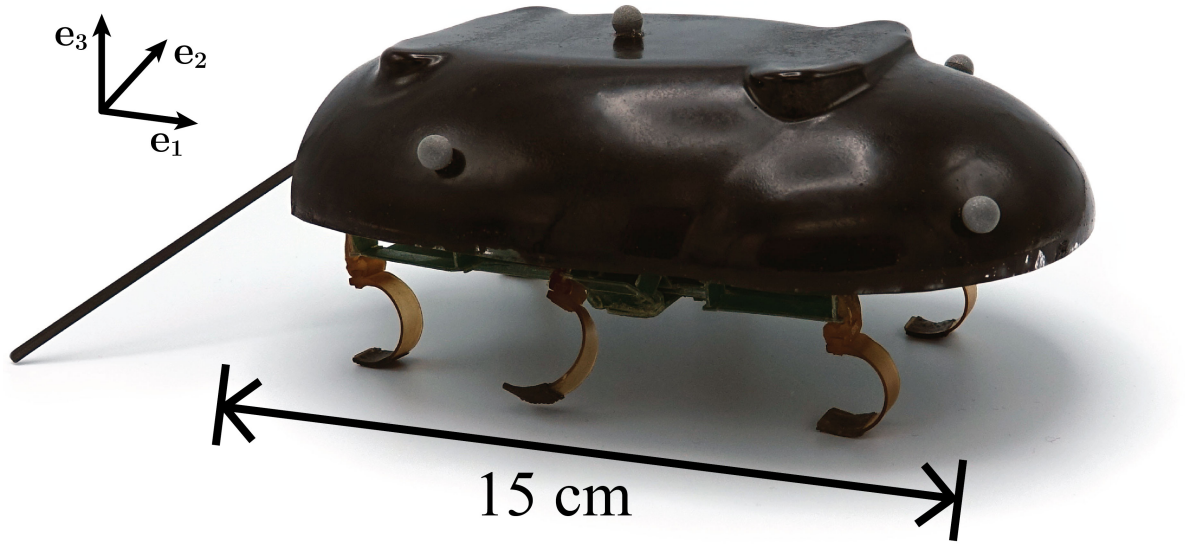


Figure 4.1: LoadRoACH with single degree of freedom tail for tail-assisted self-righting and dynamic turning.

4.2.1 Initial Design for Self-Righting

The legged robot in Figure 4.2 was developed for the tailed self-righting experiments in Chapter 5. The base platform is a modified VelociRoACH robot [43] with a mass of 53.6 g. The kinematic linkages of the robot have PET plastic as the structural material and ripstop nylon as the flexural material. To drive the robot legs with added payload, the leg transmissions have four times the torque capability of the original VelociRoACH, at the expense of a four times reduction in stride frequency. The robot has a 0.254 mm thick protective polycarbonate shell (adds 10.6 g) and a tail motor (*Pololu* 30:1 reduction high power micro metal gearmotor) that drives an interchangeable tail (adds 13.3 g). The total mass of the robot with added shell and tail is 77.5 g.

The tail is a flat carbon fiber beam (0.8 g with shaft attachment) with a width of 3 mm and a length of 10 cm. Because the tail motor is angled upward and the tail rotates along a cone, the effective tail length in the roll plane of the robot is 9 cm. The high stiffness and low mass of the carbon fiber tail is well-matched to the self-righting model, which isolates the effect of generating ground contact forces with a tail from the inertial effect of swinging a massive tail.

Although the modified version of VelociRoACH was able to perform tail-assisted dynamic self-righting while propelling itself with its legs, this robot was not able to run dynamically. The legs of VelociRoACH are driven by a single crank, with a compliant flexure mechanism constraining the output linkage to be horizontal. Due to the serial compliance of the leg mechanism, the robot running with payload tended to pitch significantly and splay its legs

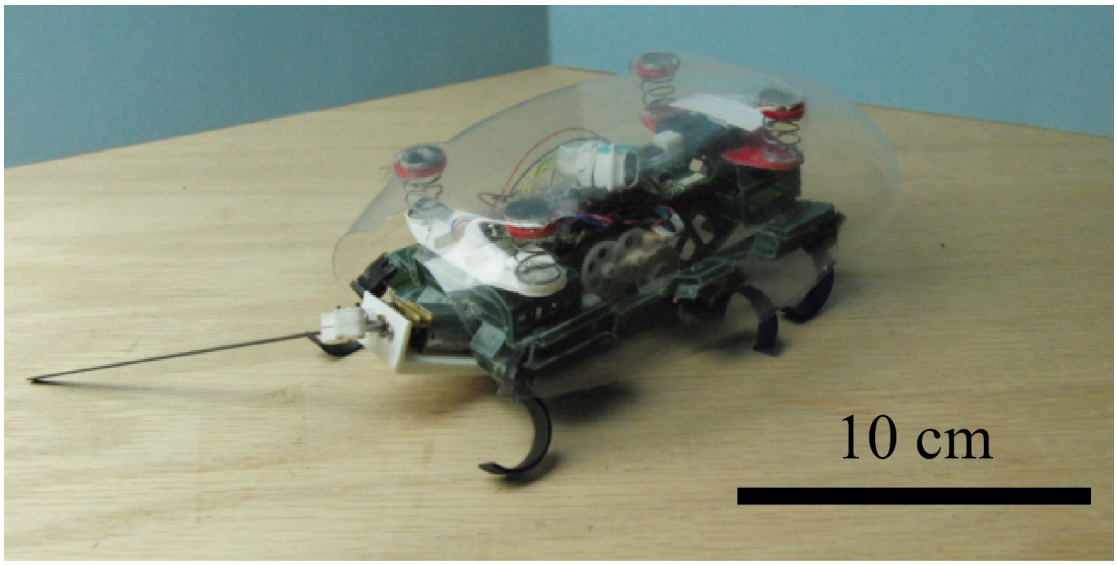


Figure 4.2: VelociRoACH with protective shell and tail for dynamic self-righting.

outward, resulting in ineffective leg propulsion. To realize the goal of achieving dynamic running with a folded legged millirobot carrying significant payload, design changes to the SCM flexure construction and leg transmission of VelociRoACH were implemented to develop LoadRoACH.

4.2.2 Folded Robot Material and Process Improvements

Due to the poor strength scaling of adhesive bonds as payload increases, the choice of materials for the structure and flexure layers of LoadRoACH needs to be carefully considered. Previous robots including DASH [9], DynaRoACH [54], OctoRoACH [112], and VelociRoACH [43] used 4 ply cardboard structures and 25 μm thick polyethylene terephthalate (PET) plastic flexures bonded with thermal adhesive to support overall masses of 16–35 g. However, initial high payload run tests of VelociRoACH with cardboard/PET SCM construction resulted in material failures including internal delamination of cardboard, delamination of PET from cardboard, and tears of PET flexures. Insights into design changes to prevent these failure modes are derived from previous tests of 180 degree peeling strength of a single structural layer bonded to a flexural layer and load until delamination tests of SCM test specimens (structure-flexure-structure layup) under cantilever bending loading.

Results for peel tests of adhesive bonds between various material combinations are shown in Table 4.2 (peel strength data are averages $\pm$ standard deviation from Haldane et al. [40]). The tests were performed according to the 180 degree peel testing standard for adhesive bonds ASTM D903 with a tensile testing machine (*Instron* 5544). A conceptual side-view schematic of the test is shown in Figure 4.3a. The structural materials are cardboard (*Pacon* 4-ply Railroad Board) and 1/16" thick balsa wood (*Midwest Products*). The flexural materials

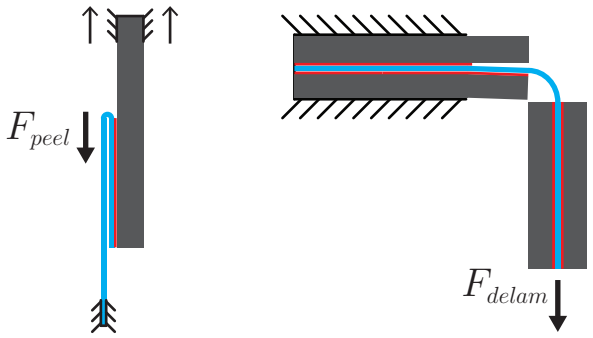


Figure 4.3: Side-view schematic of adhesive strength tests of flexural material (cyan) bonded to structural material (grey) using a thermally activated adhesive (red). (a) 180 degree peel strength test according to ASTM D903 with peel force F_{peel}. (b) Cantilever delamination strength test with delamination force F_{delam}.

Table 4.2: Peel strength of *GBC Octiva* hot-mount adhesive bonds [40]

Structural material	Flexural material	Peel strength (N/mm)
Cardboard	PET	0.095 ± 0.006
Cardboard	Ripstop nylon	0.132 ± 0.003
Balsa wood	PET	0.030 ± 0.003
Balsa wood	Ripstop nylon	0.097 ± 0.004

are 25 μm thick PET (*McMaster-Carr*) and uncoated 1.1 oz ripstop nylon (*Ripstop by the Roll*). The structural material was bonded to the flexural material using a hot-roll laminator (*Pro-Lam* PL-1200 HP) with rollers heated to 300 °F to apply thermally activated adhesive (*GBC Octiva* hot-mount adhesive). To improve bonding to the porous ripstop nylon fabric, the nylon was first dessicated in a vacuum oven with a vacuum pressure of 25 inHg and a temperature of 150 °F. Also, an additional layer of thermal adhesive was bonded through the fibers of the nylon in a preprocessing lamination step.

As shown in Table 4.2, the peel strength of both cardboard and balsa wood structures bonded to nylon flexures is higher than the peel strength for bonds to PET flexures. This is likely due to the preprocessing lamination step that embedded hot-mount adhesive into the ripstop nylon fabric. Also note that all the specimens with cardboard structures failed by internal delamination of the cardboard plies, which indicates that a stronger adhesive bond would not significantly improve the peel strength of SCM mechanisms constructed with cardboard. The specimens with balsa wood structures failed at the surface, which suggests that a stronger adhesive bond would improve peel strength. The peel strength test data was collected by Haldane et al. to inform the design of larger scale robots, and balsa wood is not available in thicknesses compatible with palm-sized robot feature sizes. Therefore, additional

Table 4.3: Cantilever delamination strength of SCM composites

Structural material	Flexural material	Adhesive	Bond temp. (°F)	Bond pressure (psi)	Delamination strength (N/mm)
Cardboard	Ripstop nylon (preprocessed)	Hot-mount adhesive	315	40	0.597 ± 0.0613
Cardboard	Ripstop nylon (preprocessed)	Polyethylene	315	40	0.672 ± 0.107
Polycarbonate	Ripstop nylon (preprocessed)	Hot-mount adhesive	280	-	0.838 ± 0.0711
Polycarbonate	Ripstop nylon	Hot-mount adhesive	315	40	1.15 ± 0.201
Polycarbonate	Ripstop nylon (preprocessed)	Hot-mount adhesive	315	40	1.55 ± 0.0430

delamination strength tests were performed to evaluate the strength of SCM mechanisms constructed with thin plastic as the structural material.

Results for cantilever delamination strength tests of SCM composites with various material combinations and bond processing conditions are shown in Table 4.3 (delamination strength data are averages ± standard deviation for three specimens). The tests were performed by clamping one end of bonded single-flexure SCM test specimens with width (8 mm) and cantilever length (1.5 mm) equal to that of a VelociRoACH hip flexure and then applying a vertical load with hanging weights of increasing mass to the free end until delamination was observed, as pictured in Figure 4.3b. The structural materials are cardboard (*Pacon* 4-ply Railroad Board) and 254 μm thick polycarbonate (*McMaster-Carr*). The flexural material is uncoated 1.1 oz ripstop nylon (*Ripstop by the Roll*). The structural material was bonded to the flexural material using either thermally activated adhesive (*GBC Octiva* hot-mount adhesive) or 51 μm thick low-density polyethylene (*McMaster-Carr*). In the flexural material column, if "(preprocessed)" is included, then the ripstop nylon was preprocessed by bonding thermal adhesive into the porous nylon fabric. The test specimens were subjected to one of two heat/pressure treatments to bond the layers of the SCM composite together. The first method is using a hot-roll laminator (*Pro-Lam* PL-1200 HP) with rollers heated to 280 °F and unregulated pressure. The second method is using a heated hydraulic press (*Carver* 3889) with platens heated to 315 °F to apply 40 psi of pressure to the specimens placed between two 1/4" thick pieces of silicone rubber for 60 s.

As shown in Table 4.3, the SCM composites with cardboard structures and ripstop nylon flexures have the lowest delamination strength. As in the peel strength tests, the cardboard specimens were observed to fail due to internal delamination of the cardboard. Using polyethylene instead of hot-mount adhesive to bond the SCM layers together only increased delamination strength by 13%. The SCM composites with polycarbonate structures and

Table 4.4: Properties of candidate SCM structural materials

	Polycarbonate	PET
Density (g/cm^3)	1.20	1.38
Flexural modulus (GPa)	2.2	2.3
Flexural strength (MPa)	90	80
Heat deflection temp. at 66 psi (°F)	280	230
Heat deflection temp. at 264 psi (°F)	270	150
Surface energy (N/m)	0.046	0.042
Laser cut quality	Charred edges	Clean edges

ripstop nylon flexures have significantly higher delamination strength values, and the delamination strength is highly sensitive to bond processing conditions. If the SCM composite was bonded using a laminator with a roller temperature of 280 °F and unregulated pressure, the delamination strength had a baseline value of 0.838 N/mm. If the SCM composite was bonded using a heated hydraulic press with a platen temperature of 315 °F and a pressure of 40 psi, the delamination strength was 37% higher for ripstop nylon without preprocessing and 85% higher for ripstop nylon with preprocessing. Overall, for SCM composites with ripstop nylon flexures, switching from cardboard to polycarbonate structures to avoid internal delamination failures improves delamination strength by 2.3x (from 0.672 N/mm for cardboard to 1.55 N/mm for polycarbonate).

From the peel strength results in Table 4.2, ripstop nylon shows a clear improvement as a flexural material over PET film with respect to bond strength. From the delamination strength results in Table 4.3, polycarbonate plastic is much more resistant to delamination because unlike cardboard, it does not fail internally. However, several factors need to be considered in the choice of a structural material for the SCM process. Properties of two candidate SCM structural materials (polycarbonate and PET) are shown in Table 4.4. Relevant properties include density, material stiffness and strength (flexural modulus and flexural strength are given), resistance to thermal processing (heat deflection temperatures at bending stresses of 66 psi and 264 psi are given), strength of bonds to thermal adhesive (surface energy is given as an indicator), and laser cut quality. In this table, all properties except surface energy are from [111]. The surface energy values are from [48].

Polycarbonate and PET have comparable density, flexural stiffness, and flexural strength. It follows that these structural materials will produce SCM composites of similar weight with similar strength and deflection under loading. In addition, the two structural materials have comparable surface energy values, so the improved delamination strength of polycarbonate

over cardboard should hold for PET as well. The two structural materials differ significantly in their resistance to thermal processing and laser cut quality. Polycarbonate is more thermally stable, as indicated by its higher heat deflection temperatures. The thermal stability of polycarbonate allows it to withstand higher temperatures and pressures while maintaining alignment of SCM flexure cuts on upper and lower structural layers. On the other hand, polycarbonate chars when laser cut, which produces more toxic fumes/residue than PET. In addition, the charred edges can make assembly of tabs in folded SCM structures more difficult. Therefore, PET is selected as the structural material, and the thermal processing at different stages of the SCM process is adjusted to ensure proper alignment of the structural layers.

Figure 4.4 highlights the design changes to LoadRoACH compared to previous RoACH robots that enable it to carry a payload equal to 50% of its body weight. LoadRoACH uses the composite structure shown in Figure 4.4b—layers of 254 μm thick PET (*McMaster-Carr*) provide structural rigidity (avoiding the internal delamination of cardboard under high loading) and a flexural layer of 25 μm thick PET (*McMaster-Carr*) bonded to 25 μm thick ripstop nylon (*Ripstop by the Roll* uncoated 1.1 oz) provides the advantages of both of these flexural materials. The thin PET layer is flexible enough to allow for free motion of the flexure while stiffening it in shear and compressive loading directions. The ripstop nylon fabric layer provides resistance to tearing under high impact forces.

To ensure the proper bonding and alignment of the SCM structure layup shown in Figure 4.4b, the following procedure was developed. In all lamination steps except for the final step, hot-mount adhesive (*GBC Octiva*) was applied using a laminator (*Pro-Lam* PL-1200 HP) with a roller temperature of 280 °F and unregulated pressure. This lower temperature compared to the 315 °F temperature used to produce the strongest bonds in Table 4.3 limits heat deflection of the structural PET layers, which prevents misalignment of flexural windows cut into these layers. For the final lamination step of the SCM parts, a different laminator (*Cheminstruments* HL-100) was used with a roller temperature of 315 °F and a nip pressure of 40 psi. Because this lamination step is performed on the final set of parts with flexures placed in correct relative locations, small thermal deformations of these parts do not significantly affect flexure functionality.

1. Two sheets of thermal adhesive are laminated through the ripstop nylon layer.
2. A single sheet of thermal adhesive is laminated to one side the flexural PET layer.
3. The ripstop nylon and flexural PET layers are laminated together, with the thermal adhesive on the flexural PET layer facing away from the nylon.
4. A single sheet of thermal adhesive is laminated to one side of each structural layer of PET.
5. The laser cutter removes flexure windows in the structural PET layers.

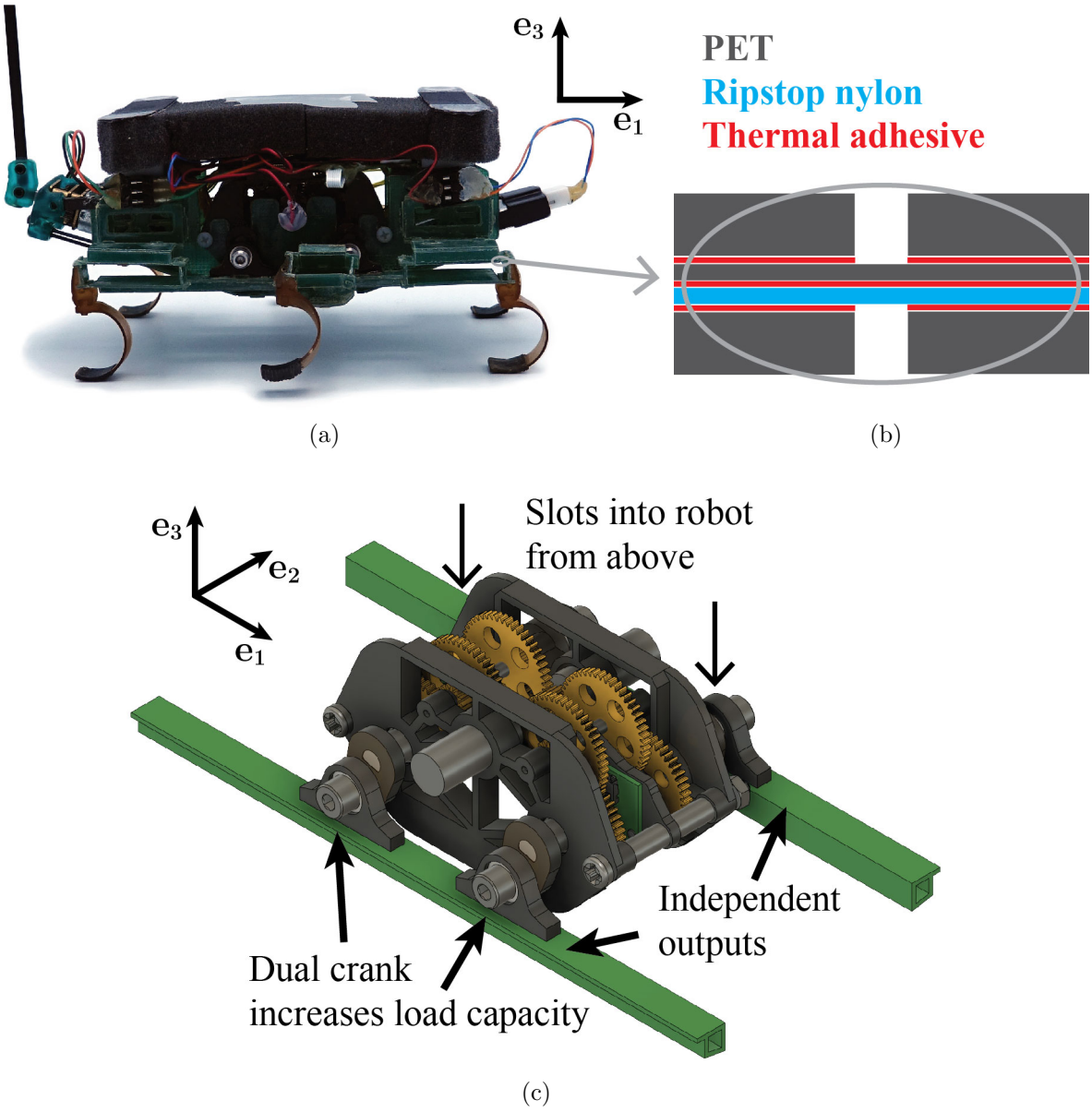


Figure 4.4: Annotated images of LoadRoACH with improved flexure technology and transmission. (a) Side view image of the robot without shell, (b) detail showing structure and flexure material, and (c) isometric solid model view of the leg transmission module.

6. The flexure windows in the two structural layers are aligned with the flexural layer placed between them and then the layers are laminated together.

7. The laser cutter performs outline cuts to release the final set of SCM parts.

8. The final set of SCM parts are laminated at higher temperature and pressure.

4.2.3 Leg Transmission Module Design

LoadRoACH has a custom transmission (pictured in Figure 4.4c) that can easily be swapped out and maintained. Nylon machine screws and hex nuts (*McMaster-Carr* 2-56 thread) hold the transmission module in place in the center of the folded robot chassis. The transmission is fabricated using polyurethane casting (*Innovative Polymers* IE-3075) for the 0.3 mm module gears, housing, and interface components, and 3D printing (*Form 2* grey resin) for the output shafts. Brushed pager motors (6 mm diameter, 3.6 Ω resistance) on each side of the transmission drive parallel geartrains with a 21.3:1 reduction, which synchronizes the motion of the two output cranks.

To reduce friction in the transmission, each output shaft is mounted in a ball bearing (*TRB RC* R144-2RS) and each output crank is attached to the output link using a shoulder screw (*McMaster-Carr* 2-56 thread) passed through a flange bearing (*McMaster-Carr* R133-2Z). The dual output crank design is similar to that of X2-VelociRoACH [42], and provides a more robust mechanical transmission of motor torques to leg forces than the planarizing four-bar linkage of VelociRoACH. The transmission also has two magnetic encoders (*AMS* AS5048B-HTSP-500) that measure the absolute rotation of diametrically polarized magnets (*SuperMagnetMan* D1021D) attached to the back of an output shaft on each side of the robot.

The output link on each side of the leg transmission drives an SCM kinematic linkage that is the synthesis of two planar mechanisms—a four-bar linkage in the sagittal plane causes the legs to protract and retract in the fore-aft direction, and a slider-crank linkage in the transverse plane causes the hips to adduct and abduct, which cycles the legs between stance and swing phases. Figure 4.5 shows a conceptual saggital plane drawing of the LoadRoACH transmission driving the legs on one side of the robot. As the crank angle φ varies, the robot transitions between stances with the outer (front and back) legs and the middle legs propelling the robot. The front and back legs are in phase and the middle leg is 180° out of phase with the outer legs.

The left and right motors of the transmission module can be independently controlled to follow two different types of gaits. The first type of gait is a differential drive gait, with each leg side driven at a different rotational speed (in cycles per second, or Hz). This gait can be used to produce turns, but the inconsistent phasing between the leg sides can produce transient disturbances to the motion. The second type of gait is a phase-locked gait, with each leg side driven at the same rotational speed and with a constant phase difference between the left and right leg sides. The two phase-locked gaits used in the experiments in this thesis are a bounding gait with a phase difference of 0° and an alternating tripod gait with a phase difference of 180°. Refer to the front, middle, and back legs of the robot as [L1, L2, L3] for the left side and [R1, R2, R3] for the right side. In a bounding gait, the robot cycles between stances with [L1, L3, R1, R3] propelling and [L2, R2] propelling. A bounding gait produces lower amplitude roll oscillations of the robot due to symmetric ground contact on the left and right sides. In an alternating tripod gait, the robot cycles between stances with [L1, R2, L3] propelling and [R1, L2, R3] propelling. An alternating

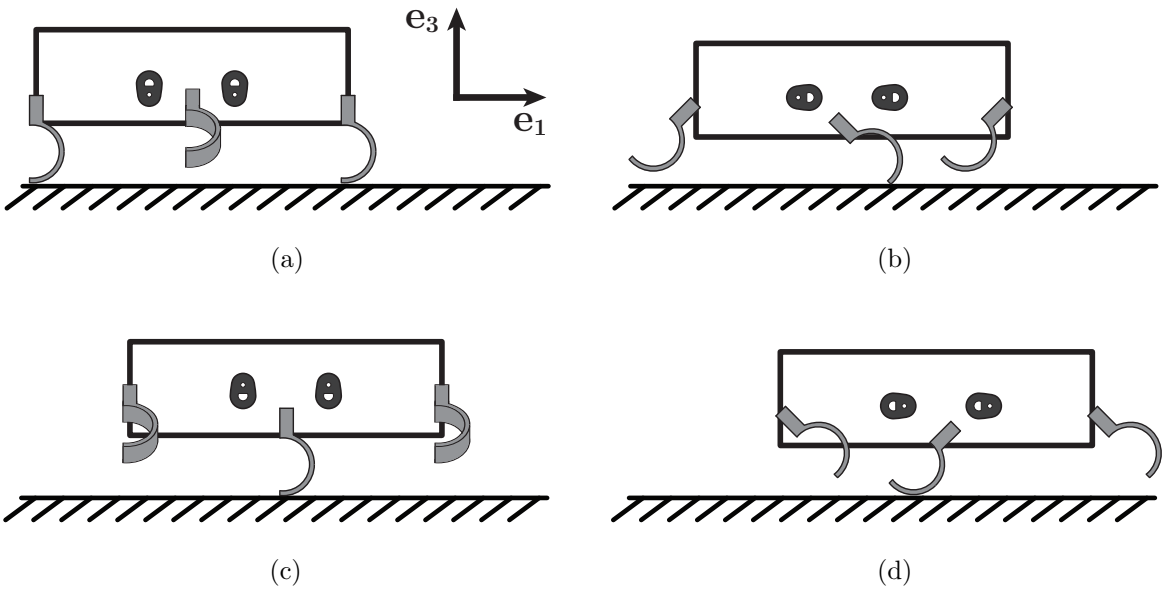


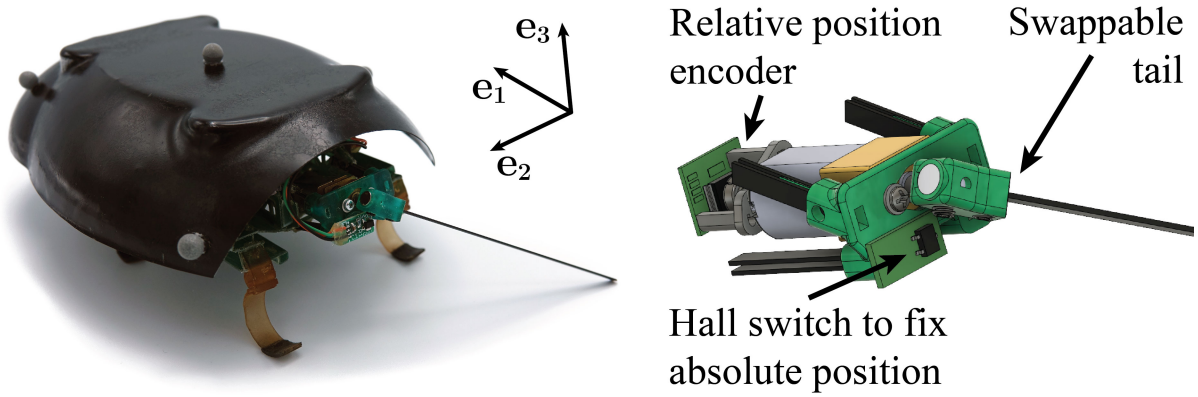
Figure 4.5: Conceptual sagittal plane drawing of robot leg positions as a function of crank angle φ. (a) Outer legs propel in mid-stance, $\varphi = 0°$. (b) Outer legs recirculate as middle leg touches down, $\varphi = 90°$. (c) Middle leg propels in mid-stance, $\varphi = 180°$. (d) Outer legs prepare to touch down as middle leg begins to recirculate, $\varphi = 270°$.

tripod gait provides a stable tripod of leg support during stances of high-speed running.

4.2.4 Shell Design

The shell design of LoadRoACH needs to satisfy multiple functional requirements. The first requirement is that the shell protects the robot from impacts during high-speed collisions. The second requirement is that the shell provides as little hindrance as possible to legged running. To address both of these requirements, the shell materials were chosen to be thermoformed 254 μm thick polycarbonate (*McMaster-Carr*), with 1/2" thick polyurethane foam (*McMaster-Carr*) providing a cushioned attachment point to the robot chassis. The polycarbonate shell is highly impact resistant and the soft polyurethane foam provides additional energy dissipation. Refer to the structural shell section of Chapter 3 for details on the shell manufacturing method, design considerations, and impact tests that informed the decision to mount the shell to the robot with a foam layer.

The polycarbonate shell is pictured with black spray paint and reflective markers for motion capture in Figures 4.1 and 4.6a, and is pictured without spray paint on the initial robot design in Figure 4.2. The ellipsoid shape on the front and sides of the shell is terradynamically streamlined to promote traversal through cluttered terrain as inspired by the study of robots and animals traversing grass-like beams by Li et al. [91]. The shell has a



(a) (b)

Figure 4.6: Tail module for LoadRoACH. (a) Image of the tail module attached to the robot. (b) Solid model diagram of the isolated tail module.

flat top for easy attachment to the polyurethane foam (pictured in Figure 4.4a). The shell attaches to the polyurethane foam using neodymium magnets fixed to the shell and foam with double-sided tape. This magnetic attachment allows for easy removal of the shell for robot programming and maintenance.

With all attachment components included, the shell adds 13.5 g of mass to LoadRoACH, which has a base mass of 54.8 g.

4.2.5 Tail Module Design

A picture of the tail module on the robot is shown in Figure 4.6a and a solid model representation is shown in Figure 4.6b. The tail is a 0.6 mm thick, 3 mm wide flat carbon fiber beam (*McMaster-Carr*) with a length of 9 cm, and is driven by a 30:1 reduction brushed metal gearmotor (*Pololu*). The component for mounting the motor to the robot body is 3D printed (*Form2* tough resin), with inserted flat carbon fiber beams (*McMaster-Carr*) providing attachment points to the flat structural plates at the back of the robot. The 3D printed tail mount attaches to the output shaft of the motor gearbox with set screws (*McMaster-Carr* M3 thread), which allows for easy swapping of tails. With all attachment components included, the tail adds an additional 13.7 g to LoadRoACH.

The magnetic encoder (*AMS* AS5048B-HTSP-500) placed behind a diametrically polarized magnet (*SuperMagnetMan* D1021D) on the back shaft of the motor measures the relative rotation of the output shaft (the back shaft rotates 30 times for every one rotation of the output shaft). The Hall switch on the front of the motor mount detects the passing of another diametrically polarized magnet attached to the tail mount. Based on the assembly of the Hall switch and magnet, biasing constants are determined to zero the tail position relative to the body-fixed vertical upon detection of a falling edge of the binary Hall switch

signal (a high reading indicates the presence of a magnetic field). In the microcontroller firmware, a debouncing scheme requires 12 consecutive high readings (sampled every 1 ms) before a falling edge to trigger a zero event. Zeroing the tail position with the Hall switch re-establishes the tail's absolute position after motor shaft slip events that can occur when the tail exerts large forces on the ground.

4.2.6 Multi-Material Leg Design

LoadRoACH runs with multi-material C-legs pictured in Figures 4.1 and 4.4a. The robot's legs need to satisfy two functional requirements. The first requirement is that the legs have stiffness that is tuned for effective dynamic running. The second requirement is that the legs have sufficient traction on rough and smooth terrain. To address both of these requirements, the C-legs are custom manufactured using a multi-material urethane casting process.

The process flow for manufacturing the robot's C-legs is shown in Figure 4.7. First, the C-leg with dovetail connector is cast (shown in Figure 4.7a) using a Shore D rigid polyurethane (*Innovative Polymers* TP-4014). The mold for the C-leg is made from silicone (*Quantum Silicones* QM 270) cast around 3D printed sacrificial parts (*Form 2* black) placed in a mold box. To remove bubbles from the silicone mold, the mixed silicone is placed in a vacuum chamber with a vacuum pressure of 28 inHg for 5 minutes before pouring and for 15 minutes after pouring. To remove bubbles from the cast C-leg, the mixed polyurethane poured into the mold is placed in a vacuum chamber with a vacuum pressure of 28 inHg for 1 minute and is then placed in a pressure pot with a pressure of 40 psi under a weighted aluminum plate (with *Polytek* Pol-Ease 2300 mold release applied) until demolding. Second, the C-leg is placed in a jig with hole guides and a hand drill is used to make 1.5 mm diameter attachment holes for the tread (shown in Figure 4.7b). Third, the C-leg is placed in a 3D printed (*Form 2* clear) two-part tread mold (shown in Figure 4.7c) and mold release is applied. Fourth, the leg tread is cast (shown in Figure 4.7d) around the tip of the C-leg using a Shore A urethane elastomer (*Innovative Polymers* IE-8000). The urethane elastomer flows through the holes in the C-leg, forming rivet attachment points to the leg tip without adhesive bonds. As in the C-leg casting step in Figure 4.7a, the tread mold and C-leg with poured elastomer undergoes successive vacuum chamber and pressure pot processing. Fifth, the C-leg with cast tread is removed from the two-part mold and excess urethane elastomer is cut away from the leg with an Exacto knife. Finally, the leg is cleaned with isopropyl alcohol to remove excess mold release.

The selection of leg stiffness is informed by the biomechanics observations of Blickhan and Full [10]. In a review of running experiments of 2, 4, 6, and 8 legged animals, the authors found that the running dynamics of the studied animals was well-matched to a single-leg reduced-order Spring Loaded Inverted Pendulum (SLIP) model. In this model, the dimensionless relative stiffness k_{rel} of the single effective leg was found to be around 10 across animals with different leg numbers and morphologies. According to dynamic scaling relations, similar values of k_{rel} as given below result in dynamically similar running behavior due to preserved ratios of centrifugal force to weight and natural frequency to

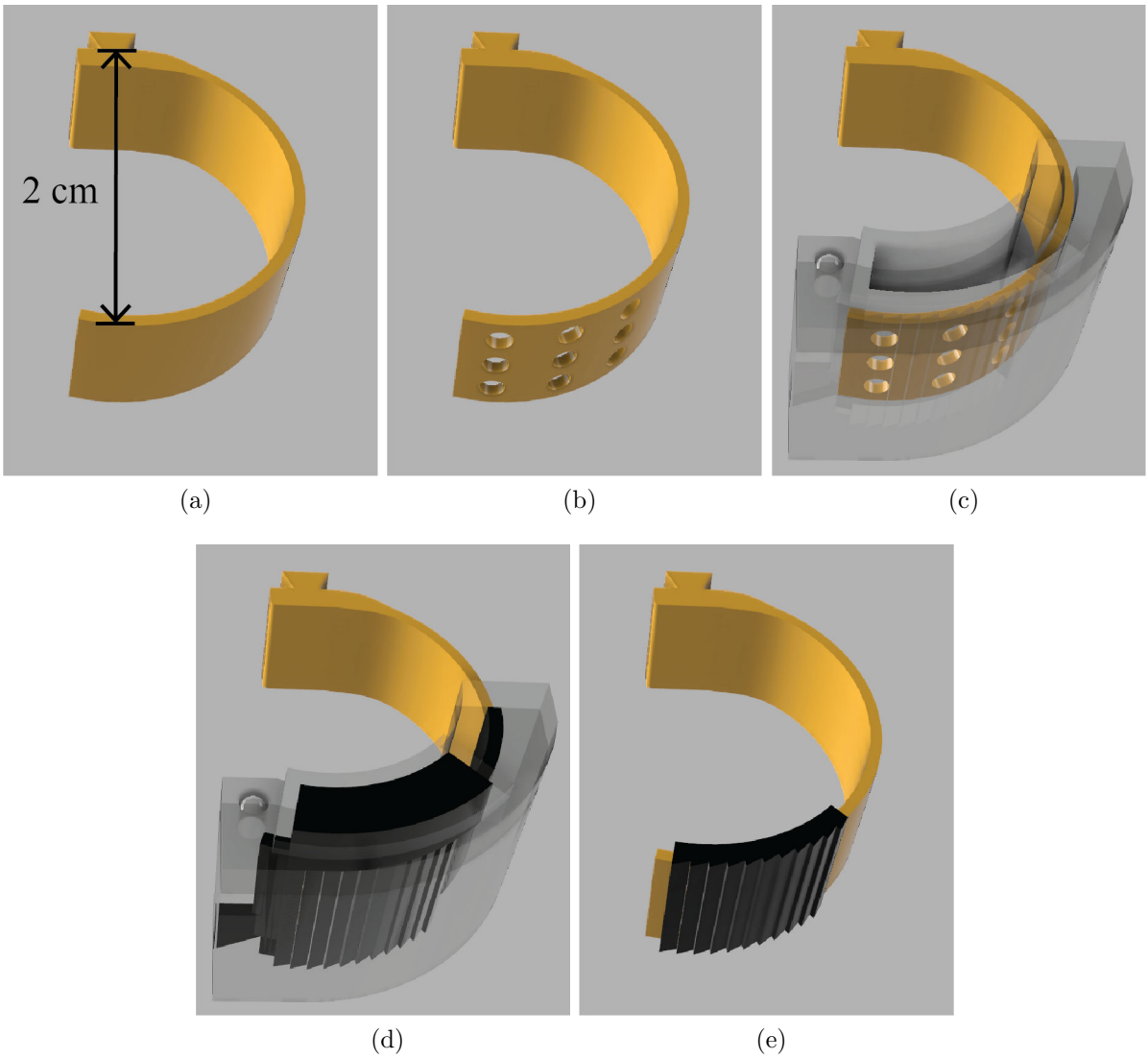


Figure 4.7: Multi-material leg manufacturing process flow. (a) Cast rigid polyurethane leg. (b) Drill holes for tread attachment. (c) Place leg in two-part tread mold. (d) Cast urethane elastomer overmolded tread. (e) Remove leg from mold and trim away excess urethane elastomer.

angular velocity:

$$k_{rel} = \frac{k_{eff} l_{eff}}{mg}. \tag{4.16}$$

In (4.16), k_{eff} is the stiffness of the single effective leg, l_{eff} is the uncompressed length of the leg, m is the total mass, and g is the gravitational constant. In order for LoadRoACH to maintain dynamically similar running to biological runners, the leg geometry and material

was chosen to achieve a value of k_{rel} close to 10. The 2 cm diameter C-legs constructed from TP-4014 have a thickness of 0.635 mm and a measured vertical stiffness $k_{leg} = 120$ N/m. The stiffness measurements were collected by compressing the legs vertically with a displacement of 5 mm and measuring the spring reading using a scale. The robot structure connecting the leg attachment point to the output crank also has some compliance, which results in a spring softening effect. The robot structure has an average stiffness of $k_{struct} = 293$ N/m per leg, which was measured by applying vertical forces at each leg attachment point. Assuming the robot has 3 legs in contact with the ground in an alternating tripod gait, the stiffness of its single effective leg due to the serial compliance of the legs and robot structure is:

$$k_{eff} = 3\left(k_{leg}^{-1} + k_{struct}^{-1}\right)^{-1}. \tag{4.17}$$

With the measured values for k_{leg} and k_{struct} inserted into (4.17), the effective leg stiffness of the robot is $k_{eff} = 255$ N/m. With effective leg length $l_{eff} = 3$ cm measured vertically from the contacting leg tips to the centerline of the output cranks of the transmission and mass $m = 82$ g, the relative leg stiffness of LoadRoACH is computed from (4.16) to be $k_{rel} = 9.5$.

The C-legs with elastomer tread are able to engage textured and smooth surfaces with high traction. The coefficient of friction of the C-legs was measured with a three-axis force sensor (*ATI* Nano43) by loading the leg vertically on a test patch of material and then dragging it backwards towards the open end of the "C". From these tests, the effective coefficient of friction of the leg was determined to be 1.25 for engagement with low-pile carpet and 0.65 for engagement with polyethylene tarp. Due to physical engagement of the leg tip with the loops of the carpet, the leg has a very high coefficient of friction on low-pile carpet. Due to engagement with the elastomer tread, the leg has a significantly higher coefficient of friction on tarp than typical values for rigid plastic engagement with steel that range from 0.1 to 0.4.

4.2.7 Power, Communication, and Control Electronics

LoadRoACH is powered by a single cell 300 mAh lithium polymer battery (*Lectron Pro*) and has an ImageProc 2.5c [3] for control and sensing. The ImageProc 2.5c consists of a 16-bit microcontroller (*Microchip* dsPIC33F), a Zigbee radio for experiment communication and telemetry recording (*Atmel* AT86RF233-ZU), two dual H bridges for motor control (*Texas Instruments* DRV8833RTY), and a six-axis gyroscope and accelerometer for inertial sensing (*InvenSense* MPU-6000). The microcontroller connects over an I2C bus to the magnetic rotary encoders (*AMS* AS5048B-HTSP-500) that measure leg and tail positions.

4.2.8 Low-Level Leg and Tail Control

The dsPIC33F microcontroller on the ImageProc 2.5c runs discrete time control loops at 1 kHz to apply pulse-width-modulated (PWM) voltage signals to the motors that track

desired leg gaits and tail motions. These simple proportional-integral-derivative (PID) controllers use position feedback from the rotary encoders that track the angular motion of the leg transmission and tail motor output shafts.

4.2.8.1 Leg Control

The block diagram for LoadRoACH's PID leg controller is shown in Figure 4.8. For clarity of explanation, this controller is represented as a continuous time block diagram, but in the experiments a discrete control loop is implemented on the robot's microcontroller. In the discrete control loop, the microcontroller takes sensor readings and updates PID terms every 1 ms, with the difference between the current position and the previous time step position applied for differentiation and the summation of positions over all previous time steps applied for integration. For each leg side, the gait synthesis block generates a position reference signal p_{ref} from an input stride frequency f and intrastride position setpoints $\boldsymbol{\delta} = [\delta_1, \delta_2, \delta_3, \delta_4]$. In a single leg cycle, the robot advances its leg position by 2π radians over a period T starting from the bottom dead center output crank position pictured in Figure 4.5a, which results in an average stride frequency of f.

The elements of $\boldsymbol{\delta}$ are fractional values that range from 0 to 1, which represent the fraction of a full leg cycle that the output crank advances during each $T/4$ seconds of the stride. The intrastride position setpoints sum to a full leg cycle, resulting in the relation $\sum_{i=1}^{4} \delta_i = 1$. Setting $\boldsymbol{\delta} = [0.25, 0.25, 0.25, 0.25]$ produces a constant velocity profile for p_{ref}. Increasing δ_2 and δ_3 relative to δ_1 and δ_4 results in faster recirculation and slower propulsion of the outer legs, based on the leg positions shown in Figure 4.5.

As discussed in Subsection 4.2.3, the leg controllers for the left and right leg sets can be implemented with different stride frequencies f for differential drive gaits or with a phase offset in the position reference signal p_{ref} for phase-locked gaits (bounding or alternating tripod).

The PID leg controller uses feedback on the leg crank angle φ. Magnetic rotary encoders placed behind the leg transmission output shafts are used to update the leg position measurement p_{meas}. Using this feedback, the controller computes a pulse-width-modulated (PWM) voltage u, which is the control signal. The control signal consists of four summed correction terms: a proportional term with gain K_P, an integral term with gain K_I, a derivative term with gain K_D, and a feedforward term with gain K_{ff}. The motor control signal can range from a minimum value of $-u_{max} = -3800$ counts, which produces full duty cycle backward drive, to a maximum value of $u_{max} = 3800$ counts, which produces full duty cycle forward drive. The control saturation block ensures that the PWM signal u_{sat} sent by the H bridge of the ImageProc2.5c to the drive motors is clipped to these limits. Note that the actual maximum value of the PWM signal is 4096 counts (100% duty cycle) and not 3800 counts (93% duty cycle). The ImageProc2.5c firmware limits the maximum PWM to 3800 counts to sample the back electromotive force of the motor during the off time of the control signal.

For the proportional correction term, the position error p_{err} is acted on by a modulo adjustment that generates an error signal p_{mod}. The modulo adjustment causes the gait

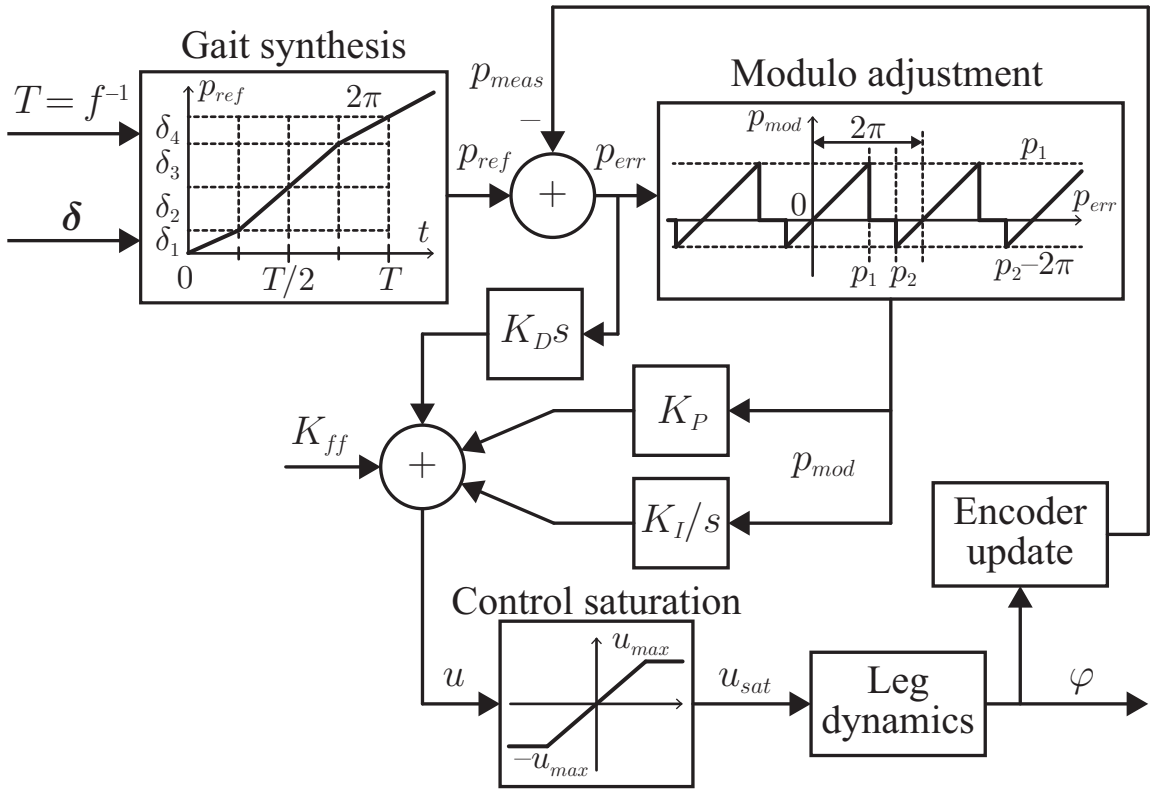


Figure 4.8: PID leg controller block diagram.

controller to synchronize with the relative position in the cycle as opposed to the absolute position, which prevents erratic jumps in leg velocity exceeding the desired stride frequency f after missing one or several leg cycles. If the modulo 2π error is less than p_1, then p_{mod} is positive and the proportional term drives the motor forward to catch up with the cycle. If the modulo 2π error is between p_1 and p_2, then p_{mod} is zero and the proportional term makes no correction as the position reference catches up with the leg position. If the modulo 2π error is between p_2 and 2π, then 2π is subtracted from the error to produce a negative value of p_{mod} and the proportional term drives the motor backward to re-synchronize with the cycle. This modulo adjustment of the proportional error allows for smoother motion in the presence of intermittent stalling of the transmission that may occur while running with high payload on high-friction or granular terrain. The error signal p_{mod} is scaled by a proportional gain K_P to generate a contribution to the motor control signal u.

For the integral correction term, the proportional error with modulo adjustment is integrated in time. On the microcontroller, discrete integration is achieved by adding to an integral error term at each time step. During each time step, the integral error is incremented by the current value of p_{mod} multiplied by the time step of 1 ms. The integral error is scaled by an integral gain K_I.

Table 4.5: Leg controller parameters

Parameter name	Symbol	Value
Proportional gain	K_P	444.4 PWM/deg
Integral gain	K_I	520.8 PWM/(deg-s)
Derivative gain	K_D	1.138 PWM/(deg/s)
Feedforward gain	K_{ff}	500 PWM
Control saturation limit	u_{max}	3800 PWM
Forward drive upper limit	p_1	270 deg
Backward drive lower limit	p_2	315 deg
Intrastride setpoints	$\boldsymbol{\delta}$	$[0.175, 0.325, 0.325, 0.175]$

For the derivative correction term, the error in leg position p_{err} is differentiated in time and then scaled by a derivative gain K_D. On the microcontroller, discrete differentiation is achieved by subtracting the previous value of p_{err} from the current measurement and dividing by the time step of 1 ms.

For the feedforward correction term, a constant PWM value given by feedforward gain K_{ff} is added directly to the PID correction terms. This feedforward gain compensates for friction in the transmission.

The leg controller parameters used for the experiments in the following chapters are shown in Table 4.5. These parameters are hand-tuned from successive running experiments on a carpet surface. The intrastride setpoints $\boldsymbol{\delta}$ were selected based on alternating tripod experiments with a stride frequency of $f = 10$ Hz. These experiments showed that faster recirculation and slower propulsion of the outer legs of the robot resulted in similar forward speeds and better leg tracking when compared to experiments with constant leg velocity or with faster propulsion and slower recirculation of the outer legs.

4.2.8.2 Tail Control

The block diagram for LoadRoACH's PID tail controller is shown in Figure 4.8. The tail position reference signal p_{ref} is generated in either a position or velocity input mode. If the position input p_{in} is set, then the tail moves to and holds an absolute angular position. If the velocity input v_{in} is set, then the tail rotates with constant angular velocity.

The PID tail controller uses feedback on the tail angle θ_t. The magnetic rotary encoder on the back shaft of the tail motor updates the relative position of the tail to generate the position measurement p_{meas}. The zero position p_{bias} is updated when the magnet on the tail motor output shaft passes over the digital Hall effect sensor on the front of the motor.

Because the tail is driven by significantly higher torque and supports less weight under nominal operation compared to the legs, stall events do not occur. Therefore, the tail controller does not feature the same modulo 2π adjustment of the position error as the leg controller. Similar to the leg controller, the tail controller has proportional, integral,

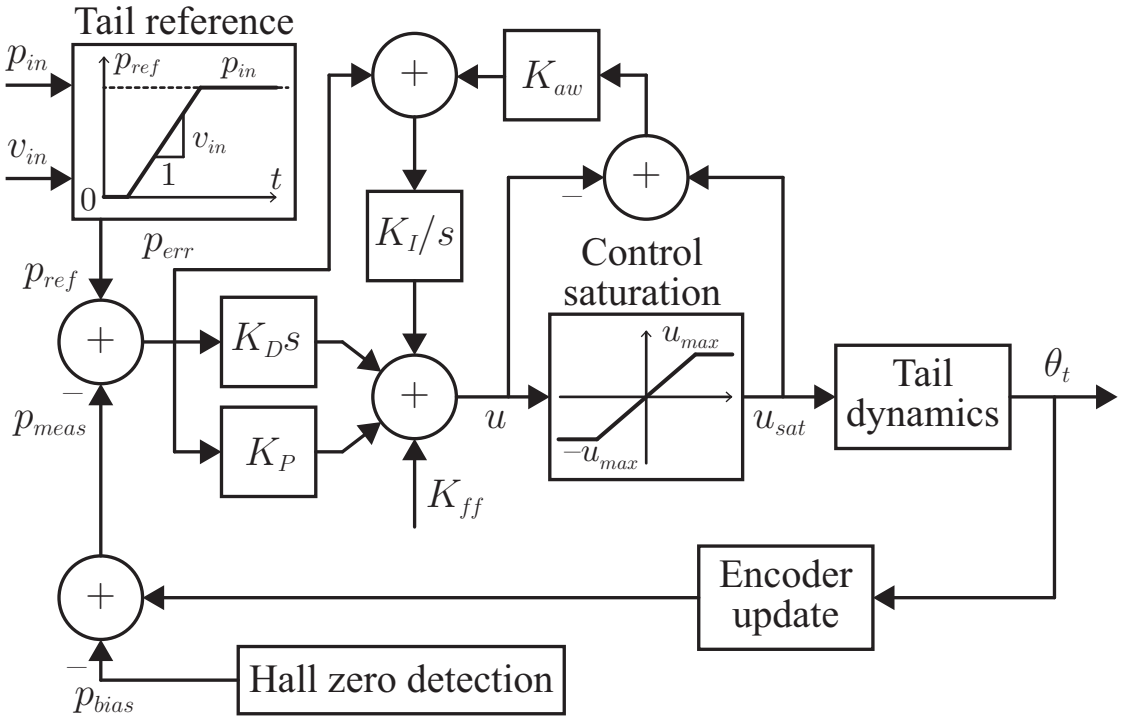


Figure 4.9: PID tail controller block diagram.

Table 4.6: Tail controller parameters

Parameter name	Symbol	Value
Proportional gain	K_P	666.7 PWM/deg
Integral gain	K_I	3906 PWM/(deg-s)
Derivative gain	K_D	10.24 PWM/(deg/s)
Anti-windup gain	K_{aw}	0.05859 deg/PWM
Feedforward gain	K_{ff}	0 PWM
Control saturation limit	u_{max}	3800 PWM

derivative, and feedforward correction terms with gains K_P, K_I, K_D, and K_{ff}. An anti-windup term $K_{aw}\,(u_{sat} - u)$ is added to p_{err} before integration and scaling by K_I. This anti-windup term provides negative feedback that corrects the control signal u towards the saturation limit $\pm u_{max}$ in the case of controller saturation, which may occur if high loading of the tail causes the p_{meas} to lag significantly behind p_{ref}.

The tail controller parameters used for the experiments in the following chapters are shown in Table 4.6. These parameters are hand-tuned from successive experiments of the tail tracking a step change in position.

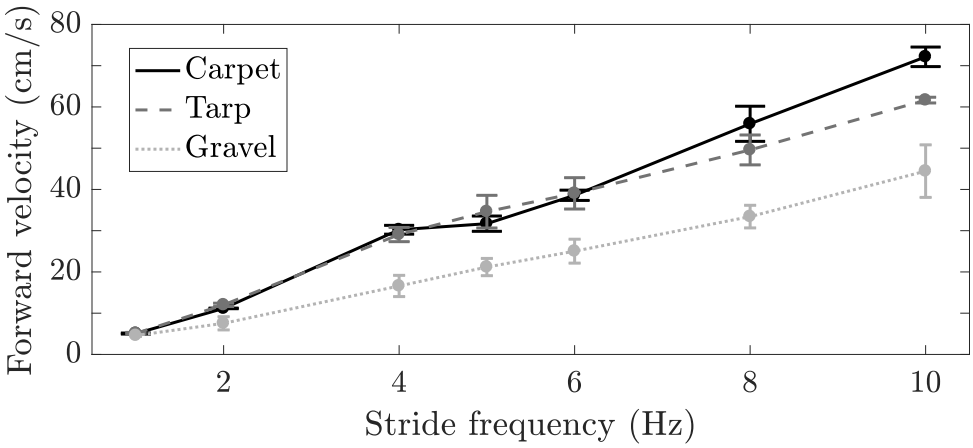


Figure 4.10: Average forward velocity for alternating tripod gaits with varying stride frequency on different surfaces. The data points are experimental averages over 5 trials and the error bars show one standard deviation.

4.3 Running with High Payload

With improved mechanical robustness of its flexures and transmission, the 54.8 g LoadRoACH robot is able to dynamically run while carrying a tail and shell payload of 27.2 g. To benchmark the running performance of LoadRoACH with a tail and shell payload, the robot was run in a motion capture environment (*OptiTrack*). The robot was commanded to follow an alternating tripod gait with stride frequencies ranging from 1 Hz to 10 Hz on carpet, tarp, and loose gravel (with centimeter-scale rocks) surfaces. The average forward velocity of the robot over 5 trials for each experiment condition are shown in Figure 4.10. At the fastest trackable stride frequency of 10 Hz, the robot has the highest forward velocity of 72 cm/s on carpet (with a measured leg-ground C.o.F. of 1.25). The robot also runs well on tarp (with a measured leg-ground C.o.F. of 0.65), because its cast polyurethane C-legs have a soft overmolded tread. Straight running velocity significantly decreases to 44 cm/s on gravel, because the robot has to overcome ineffective leg pushes against gravel and body-terrain interaction forces. Compared to the 30 g VelociRoACH running at 10 Hz without an aerodynamic stabilizer [43], LoadRoACH on average runs only 3 cm/s slower on carpet.

Whereas VelociRoACH is dynamically scaled from a Spring Loaded Inverted Pendulum model of an American cockroach (one of nature's fastest insects) to run with a maximum stride frequency of 24 Hz and a forward velocity of 2.5 m/s, the forward velocity of LoadRoACH is limited by motor power. The stride frequency of LoadRoACH was limited to 10 Hz because frictional losses in the transmission, inertial loading of the output linkages, and leg-ground reaction forces were balanced by the leg motors at this operation point. More motor power is required for higher speed running, and the scaling consequences of adding payload to a legged robot design while considering legged running dynamics, transmission losses, and available motor power is a potential avenue for future research.

Chapter 5

Tailed Self-Righting with Terrain Contact

5.1 Terrestrial Tailed Self-Righting Analysis

In this section, a roll-plane model of tail-assisted self-righting is developed assuming flat uniform terrain with Coulomb friction to determine tail design requirements and to predict the time required to self-right.

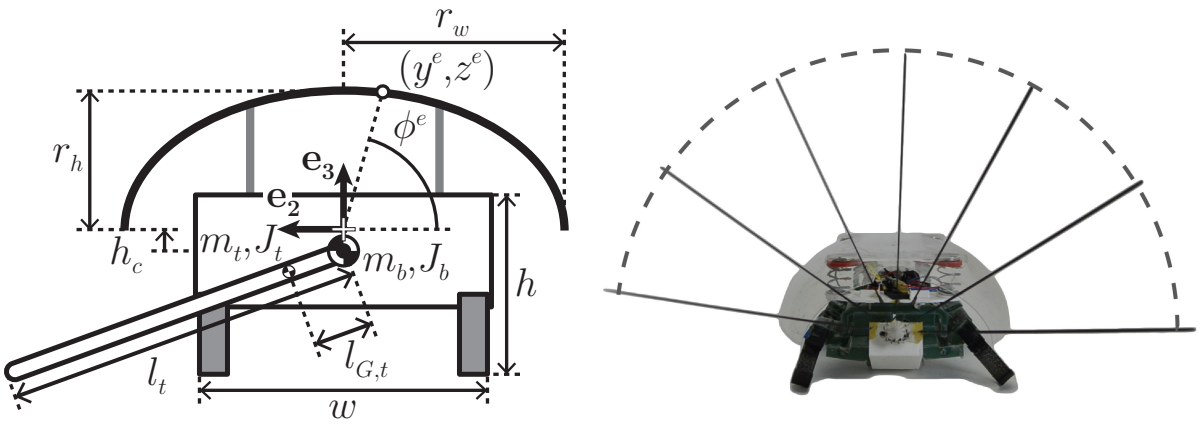
5.1.1 Model Parameters

For the dynamic model of tailed self-righting, Figure 5.1a shows the mass and geometry parameters of a VelociRoACH robot with shell and tail. The robot body with shell has mass m_b and mass moment of inertia about its roll axis J_b. The robot without shell has overall width w and overall height h. The robot's rigidly mounted shell is approximated as half an ellipse in the roll plane of the robot, with major axis radius along the width of the robot r_w, minor axis radius along the height of the robot r_h, and center offset height above the center of mass (C.o.M.) of the robot h_c.

A rigid tail is driven by a motor in the roll plane of the robot, with an assumed pivot point about the C.o.M. for simplicity of analysis. The tail has mass m_t and mass moment of inertia about its C.o.M. J_t. The tail C.o.M. is located a distance $l_{G,t}$ from the tail pivot. Overlaid video frames of the VelociRoACH robot used in experiments swinging its tail are shown in Figure 5.1b. Model parameters for this robot platform are given in Table 5.1.

5.1.2 Newtonian Dynamics Formulation

Figure 5.2 shows free body diagrams of tail-assisted self-righting. The analysis of self-righting is performed in the roll plane of the robot with world-fixed Cartesian frame $\{\mathbf{E_1}, \mathbf{E_2}, \mathbf{E_3}\}$, where $\mathbf{E_1}$ points into the page. The forces acting on the system include gravity ($\mathbf{g} = -g\mathbf{E_3}$, $g = 9.81$ m/s^2), body contact force $\mathbf{F_b}$, and tail contact force $\mathbf{F_t}$. In Figure 5.2a, $m = m_b + m_t$



(a) (b)

Figure 5.1: (a) Back view diagram showing mass and geometry parameters of a VelociRoACH robot with shell and active tail. (b) Overlaid video frames of VelociRoACH swinging its tail.

Table 5.1: VelociRoACH with shell and tail parameters

Parameter name	Symbol	Value
Body mass	m_b	76.7 g
Body mass moment of inertia	J_b	583 g-cm^2
Overall width, height	(w, h)	$(7.5, 4.5)$ cm
Shell major, minor axis radius	(r_w, r_h)	$(5.5, 3.5)$ cm
Shell center offset height	h_c	0 cm
Tail mass	m_t	0.8 g
Tail mass moment of inertia	J_t	3.5 g-cm^2
Tail length, C.o.M. distance	$(l_t, l_{G,t})$	$(9, 1.5)$ cm
Tail stall torque	τ_s	29.5 mN-m
Tail no-load speed	ω_{nl}	77 rad/s

is the total system mass. The net inertial force due to linear acceleration of the system C.o.M. is $-M\mathbf{a_G} = -m_b\mathbf{a_{G,b}} - m_t\mathbf{a_{G,t}}$.

For a given body roll angle θ_b (counterclockwise relative to $-\mathbf{E_2}$), the kinematics of a rolling ellipse provide constraints on the velocity and acceleration of the robot body. Figure 5.1a shows the coordinates (y^e, z^e) of a point on the ellipse shell in the frame of the ellipse $\{\mathbf{e_2}, \mathbf{e_3}\}$. This point is located at an angle ϕ^e relative to $-\mathbf{e_2}$. Using an alternate angle parameter ϕ satisfying $\tan\phi = \frac{r_h}{r_w}\tan\phi^e$, the body contact coordinates from the ellipse

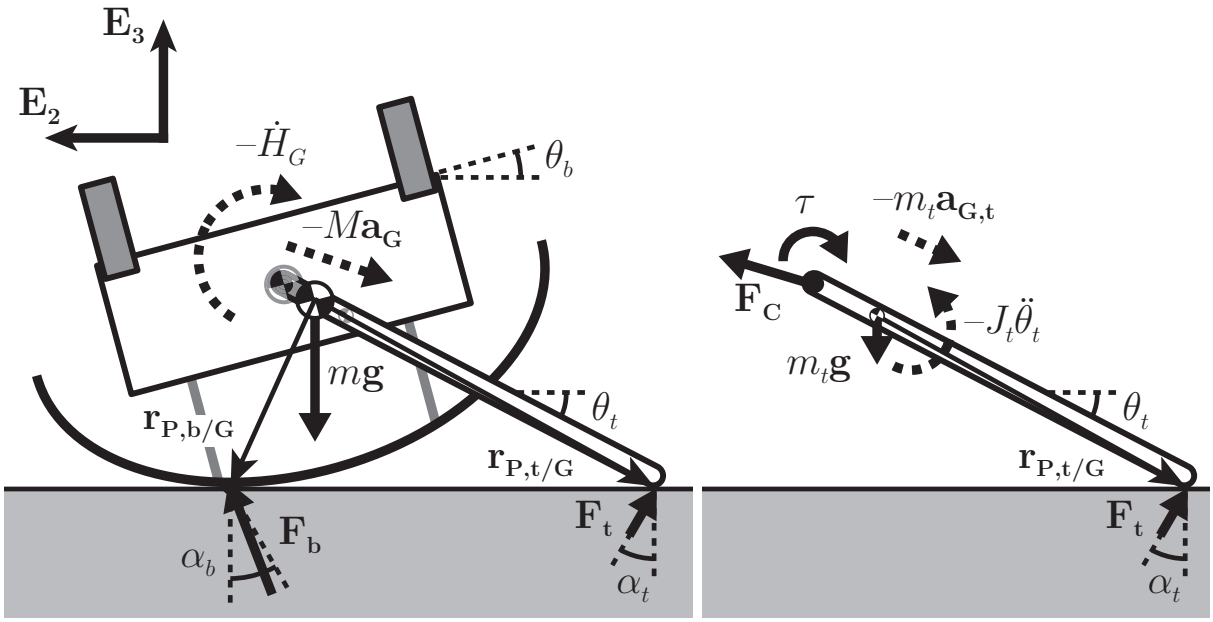


Figure 5.2: Roll plane diagrams of the forces and moments that act on a tailed robot during a dynamic self-righting maneuver. (a) Free body diagram of the overall system and (b) free body diagram of the tail.

center in the frame of the ellipse are:

$$y^e_{P,b} = -r_w \cos\phi \tag{5.1}$$

$$z^e_{P,b} = r_h \sin\phi \tag{5.2}$$

$$\phi = \tan^{-1}\left(\frac{r_h}{r_w \tan\theta_b}\right). \tag{5.3}$$

For contact with the ellipse shell, the value of ϕ as a function of θ_b is determined from the tangency condition (5.3), which ensures that the tangent vector to the ellipse points along the horizontal $\mathbf{E_2}$. These contact coordinates are valid for counterclockwise righting with $\theta_b \in [0°, 90°]$. For body angles greater than 90°, the robot is assumed to rotate about the edge of the shell. A rotation is applied to transform the contact displacements into the world-fixed Cartesian frame:

$$\mathbf{r_{P,b/G,b}} = \left(-y^e_{P,b}\cos\theta_b - \left(z^e_{P,b} + h_c\right)\sin\theta_b\right)\mathbf{E_2} + \left(-\left(z^e_{P,b} + h_c\right)\cos\theta_b + y^e_{P,b}\sin\theta_b\right)\mathbf{E_3}. \tag{5.4}$$

In (5.4), the notation $\mathbf{r_{P,b/G,b}}$ indicates the position vector pointing from the body C.o.M. to the body contact point. In the following equations, the subscripts $\mathbf{P,b}$ and $\mathbf{P,t}$ refer to body and tail contact points. The subscripts $\mathbf{G,b}$ and $\mathbf{G,t}$ refer to body and tail C.o.M.

points. The subscript **G** refers to the system C.o.M. Assuming zero velocity at the body contact, the constrained velocity of the body C.o.M. is:

$$\mathbf{v_{G,b}} = -\dot{\theta}_b \mathbf{E_1} \times \left(-\mathbf{r_{P,b/G,b}}\right). \tag{5.5}$$

Differentiating (5.5) with respect to time results in an expression for the body C.o.M. acceleration $\mathbf{a_{G,b}}$ in terms of body angle θ_b and its time derivatives ($\dot{\theta}_b$, $\ddot{\theta}_b$).

Because the rigid tail is assumed to maintain contact with the ground, the tail angle θ_t (counterclockwise relative to $-\mathbf{E_2}$) and its time derivatives ($\dot{\theta}_t$, $\ddot{\theta}_t$) can be written in terms of the body angle:

$$\theta_t = \sin^{-1}\left(\frac{\mathbf{r_{P,b/G,b}} \cdot \mathbf{E_3}}{l_t}\right) \tag{5.6}$$

$$\dot{\theta}_t = -\frac{\mathbf{v_{G,b}} \cdot \mathbf{E_3}}{l_t \cos\theta_t} \tag{5.7}$$

$$\ddot{\theta}_t = -\left(\frac{\mathbf{v_{G,b}} \cdot \mathbf{E_3}}{l_t \cos^2\theta_t}\dot{\theta}_t \sin\theta_t + \frac{\mathbf{a_{G,b}} \cdot \mathbf{E_3}}{l_t \cos\theta_t}\right), \tag{5.8}$$

where (5.6) comes from setting the tail height $l_t \sin\theta_t$ equal to $\mathbf{r_{P,b/G,b}} \cdot \mathbf{E_3}$, (5.7) comes from enforcing zero tail contact velocity in the $\mathbf{E_3}$ direction, and (5.8) comes from differentiating (5.7) with respect to time. Now, an expression for the linear acceleration of the tail C.o.M. can be determined:

$$\mathbf{a_{G,t}} = \mathbf{a_{G,b}} - \ddot{\theta}_t \mathbf{E_1} \times l_{G,t}\left(-\cos\theta_t \mathbf{E_2} + \sin\theta_t \mathbf{E_3}\right) - \dot{\theta}_t \mathbf{E_1} \times l_{G,t}\dot{\theta}_t\left(\sin\theta_t \mathbf{E_2} + \cos\theta_t \mathbf{E_3}\right). \tag{5.9}$$

The linear momentum balance for the overall system is:

$$m_b \mathbf{a_{G,b}} + m_t \mathbf{a_{G,t}} = (m_b + m_t)\mathbf{g} + \mathbf{F_b} + \mathbf{F_t}. \tag{5.10}$$

For the overall system in Figure 5.2a, (5.10) gives two linearly independent balance equations. An angular momentum balance for the overall system can also be written:

$$\dot{H}_G = J_b \ddot{\theta}_b + \left(J_t + \frac{m_b m_t}{m_b + m_t} l_{G,t}^2\right)\ddot{\theta}_t \tag{5.11}$$

$$-\dot{H}_G \mathbf{E_1} = \mathbf{r_{P,b/G}} \times \mathbf{F_b} + \mathbf{r_{P,t/G}} \times \mathbf{F_t}, \tag{5.12}$$

where (5.11) is the time derivative of the system angular momentum about the C.o.M. and (5.12) is an angular momentum balance considering the external forces acting on the system. The displacement vectors in (5.12) are given below:

$$\mathbf{r_{P,b/G}} = \mathbf{r_{P,b/G,b}} - \mathbf{r_{G/G,b}} \tag{5.13}$$

$$\mathbf{r_{P,t/G}} = \mathbf{r_{P,t/G,b}} - \mathbf{r_{G/G,b}} \tag{5.14}$$

$$\mathbf{r_{P,t/G,b}} = l_t\left(-\cos\theta_t \mathbf{E_2} + \sin\theta_t \mathbf{E_3}\right) \tag{5.15}$$

$$\mathbf{r_{G/G,b}} = \frac{m_t l_{G,t}}{m_b + m_t}\left(-\cos\theta_t \mathbf{E_2} + \sin\theta_t \mathbf{E_3}\right). \tag{5.16}$$

The last equation to solve for the system dynamics results from an angular momentum balance for the tail depicted in Figure 5.2b. The constraint force $\mathbf{F_C}$ at the tail pivot satisfies the linear momentum balance for the tail and is given below:

$$\mathbf{F_C} = -\mathbf{F_t} - m_t\mathbf{g} + m_t\mathbf{a_{G,t}}. \tag{5.17}$$

With this expression for $\mathbf{F_C}$, the angular momentum balance for the tail about its C.o.M. is:

$$-J_t\ddot{\theta}_t\mathbf{E_1} = -\tau\mathbf{E_1} + \mathbf{r_{P,t/G,b}} \times \mathbf{F_t} - l_{G,t}\left(-\cos\theta_t\mathbf{E_2} + \sin\theta_t\mathbf{E_3}\right) \times m_t\left(\mathbf{a_{G,t}} - \mathbf{g}\right), \tag{5.18}$$

where τ is the input torque (counterclockwise about $-\mathbf{E_1}$) from a DC motor, which linearly decreases in magnitude with relative tail velocity $\dot{\theta}_t - \dot{\theta}_b$:

$$\tau = \begin{cases} -\tau_s\left(1 + \frac{\dot{\theta}_t - \dot{\theta}_b}{\omega_{nl}}\right), & \dot{\theta}_t - \dot{\theta}_b < 0 \\ -\tau_s, & \dot{\theta}_t - \dot{\theta}_b \geq 0. \end{cases} \tag{5.19}$$

In (5.19), the tail motor applies torque clockwise relative to the body with maximum control effort. The torque-speed relation is parameterized by stall torque τ_s and no-load speed ω_{nl}.

Now, to solve for the system dynamics, friction conditions are applied to the contact forces. Coulomb friction is assumed with equal static and kinetic friction coefficients. The body and tail can have different coefficients of friction μ_b and μ_t. In the case shown in Figure 5.2, the body contact is rolling without slip, so both components of $\mathbf{F_b}$ are unknown and inside the static friction cone with friction angle α_b, where $\tan\alpha_b = \mu_b$. The tail contact is sliding, so the tail normal force $\mathbf{F_t} \cdot \mathbf{E_3}$ is unknown and $\mathbf{F_t}$ is directed along the sliding friction cone parameterized by μ_t:

$$\mathbf{F_t} \cdot \mathbf{E_2} = -\mu_t\left(\mathbf{F_t} \cdot \mathbf{E_3}\right)\mathrm{sign}\left(\mathbf{v_{P,t}} \cdot \mathbf{E_2}\right), \tag{5.20}$$

where $\mathbf{v_{P,t}}$ is the tail contact velocity. The five independent equations of the system are the tail angular acceleration constraint (5.8), the $\mathbf{E_2}$ and $\mathbf{E_3}$ components of the linear momentum balance (5.10), the angular momentum balance of the robot body (5.12), and the angular momentum balance of the tail (5.18). This system of equations is linear in the unknowns $(\ddot{\theta}_b, \ddot{\theta}_t, \mathbf{F_b} \cdot \mathbf{E_2}, \mathbf{F_b} \cdot \mathbf{E_3}, \mathbf{F_t} \cdot \mathbf{E_3})$ and is solved to determine dynamics equations and constraint forces as a function of system state $(\theta_b, \dot{\theta}_b, \theta_t, \dot{\theta}_t)$. The nonlinear system of second-order differential equations for θ_b and θ_t are numerically simulated in a following subsection.

If the solution for $\mathbf{F_b}$ produces a result outside of the static friction cone, then the body contact is sliding with known $\mathbf{F_b} \cdot \mathbf{E_2}$, the $\mathbf{E_2}$ component of the roll without slip velocity constraint in (5.5) is relaxed, and additional states $(y, \dot{y})$ for the body C.o.M. horizontal displacement and velocity are added to the dynamics formulation. A similar procedure for deriving the dynamics equations follows, but now $(\dot{y}, \ddot{y})$ are included in the balance equations, resulting in three second-order differential equations for (θ_b, θ_t, y).

In the following subsections, quasi-static analysis gives minimum torque requirements for the tail motor, and the dynamic system is simulated to predict the time required for self-righting with tail contact.

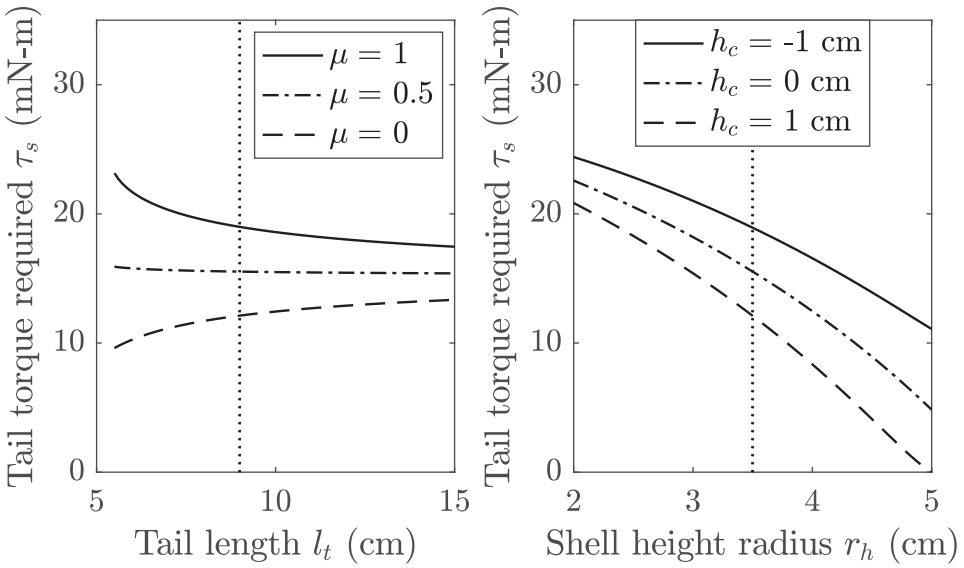


Figure 5.3: Tail torque required for quasi-static self-righting of a robot with an elliptical shell on flat terrain. (a) Varying tail length and tail-ground sliding coefficient of friction, with robot shell parameters held constant at $r_h = 3.5$ cm and $h_c = 0$. (b) Varying shell height radius and shell offset height above the C.o.M., with $l_t = 9$ cm and $\mu = 0.5$.

5.1.3 Quasi-Static Design Considerations

For quasi-static analysis of tail-assisted self-righting, the tail motor maintains static equilibrium throughout the righting process. The left-hand sides of the dynamics equations (5.10), (5.12), and (5.18) are zero, the body rolls without slip, the tail slides with Coulomb friction, and the unknowns are $(\tau, \mathbf{F_b} \cdot \mathbf{E_2}, \mathbf{F_b} \cdot \mathbf{E_3}, \mathbf{F_t} \cdot \mathbf{E_3})$. In quasi-static self-righting, the tail rotates the body from an inverted configuration ($\theta_b = 0°$) to a critical body angle ($\theta_b = \theta_b^*$). Past this critical body angle, the system C.o.M. is to the left of the body contact point and gravity tends to tip the robot onto its legs. The maximum tail motor torque over the range of admissible body angles provides a quasi-static limit on the stall torque τ_s required for tail-assisted self-righting on a horizontal surface.

First, the quasi-static tail torque required for self-righting is determined for varying tail length l_t and varying coefficient of friction $\mu = \mu_b = \mu_t$, with remaining parameters fixed at the values in Table 5.1. These results are plotted in Figure 5.3a. Over the range of tail lengths, the tail torque required increases with μ. For tail-ground interactions with no friction ($\mu = 0$), torque required increases with tail length. Shorter tails result in contact angles that are more aligned with the vertical contact force in the zero friction case, which results in a smaller torque required to move the tail. For tail-ground interactions with high friction ($\mu = 1$), the relationship between tail torque required and tail length is inverted. Because of the high friction resisting lateral motion of the tail slipping against the ground, shorter

tails result in a larger tail torque requirement. For tail-ground interactions with moderate friction ($\mu = 0.5$), tail length has a relatively minor effect on tail torque. To reduce the tail torque required to self-right on high-friction surfaces, a tail length of $l_t = 9$ cm was selected for VelociRoACH.

Next, the tail and friction parameters of the quasi-static model are held constant while the shell minor axis radius r_h and the shell offset height above the C.o.M. of the robot h_c are varied. As shown in Figure 5.3b, the tail torque required for self-righting decreases as r_h and h_c increase. As r_h approaches r_w in the $h_c = 0$ case (circular shell shape), all contact configurations on the robot shell become unstable, and the robot tends to tip towards its legs with no applied tail torque. The shape variation results suggest that the shell should extend as high as possible above the C.o.M. of the robot to reduce tail motor torque requirements for self-righting. However, increasing the overall height of the robot can prevent the robot from entering low-clearance structures. This size constraint limits the shell height parameters of VelociRoACH to $r_h = 3.5$ cm and $h_c = 0$.

Based on the quasi-static analysis, a 30:1 reduction gearmotor (*Pololu*) was selected to drive the tail, which has an output stall torque of $\tau_s = 29.5$ mN-m and a no-load speed of $\omega_{nl} = 77$ rad/s at a voltage of 3.7 V. This motor provides enough torque for the robot to quasi-statically self-right on flat terrain over the range of considered friction conditions.

5.1.4 Dynamic Righting Time Predictions

The system of second-order differential equations governing tail-assisted self-righting dynamics was numerically simulated using `ode45` in MATLAB, with events handling transitions between sliding and sticking contacts as well as detecting loss of contact when normal forces reach zero. The initial conditions are $(\theta_b, \dot{\theta}_b, \theta_t, \dot{\theta}_t)|_{t=0} = (0, 0, \theta_{t0}, 0)$, where θ_{t0} satisfies (5.6) with $\theta_b = 0$.

The results of the simulation for a wood surface ($\mu_b = 0.4$, $\mu_t = 0.5$) are shown in Figure 5.4. A negative applied tail torque rotates the tail clockwise as the body accelerates counterclockwise. For this simulation case, the body contact slips in the $-\mathbf{E_2}$ direction and the tail contact slips in the $\mathbf{E_2}$ direction. Due to Coulomb friction, this relative motion produces positive horizontal body forces and negative horizontal tail forces. The tail normal force remains relatively constant (from 31% to 39% of the robot weight), and the body normal force reaches a peak of 112% of the robot weight at time $t = 0.035$ s.

At time $t = 0.134$ s, the body and tail lose contact with the ground, and are assumed to have constant angular velocity until the robot is fully righted with $\theta_b = 180°$. The righting performance is quantified by the elapsed time, $t_r = 235$ ms.

The dynamic simulation's prediction of terrestrial righting time is now compared to aerial righting. Figure 5.5a shows the time t_r to complete aerial righting determined from the model in [93] for varying tail length l_t and tail end mass m_t. For aerial righting, t_r decreases as l_t and m_t increase (which increases the inertial leverage of the tail), with greater effects on t_r for tails with l_t ranging from 5 cm to 10 cm.

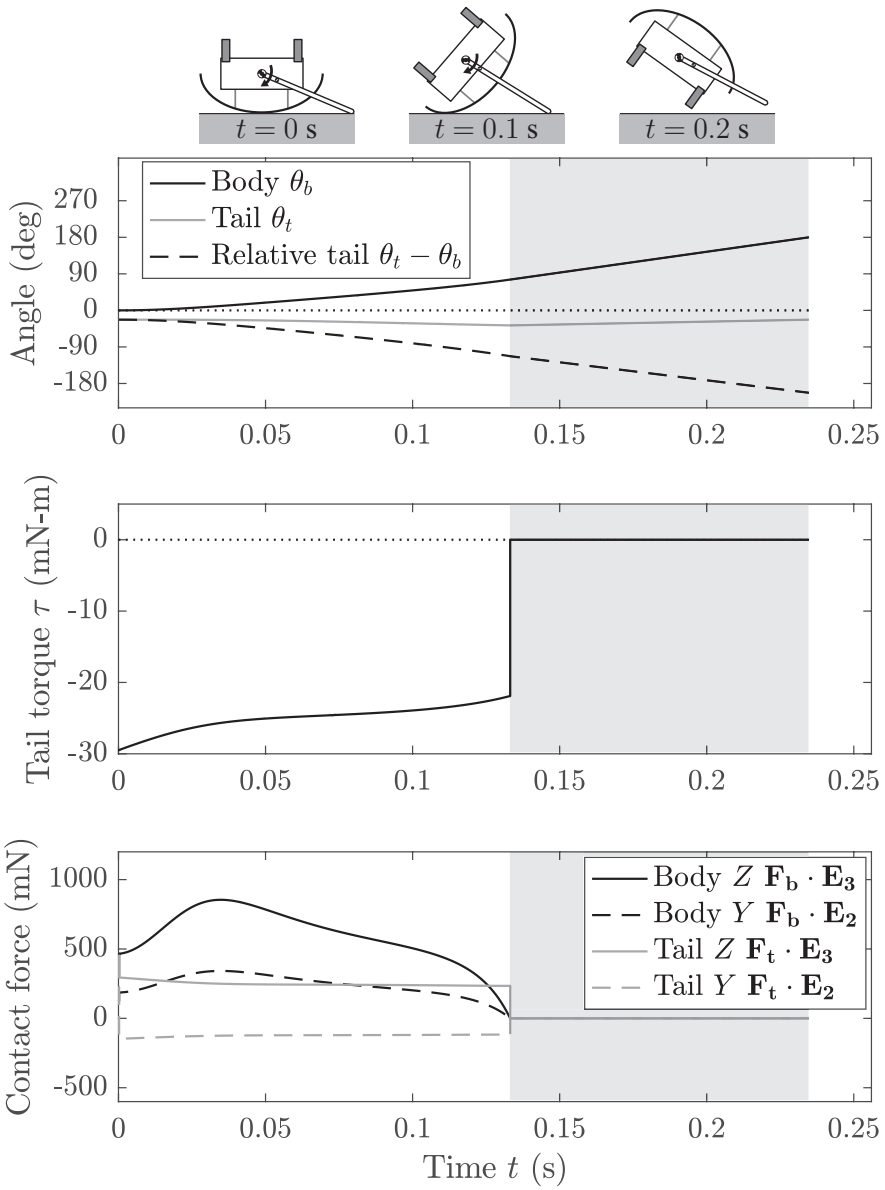


Figure 5.4: Tail-assisted self-righting dynamic simulation results on flat ground with Coulomb friction at the shell and tail contacts. The body and tail coefficients of friction are $\mu_b = 0.4$ and $\mu_t = 0.5$. The shaded time interval indicates the loss of body and tail ground contact.

Assuming uniform friction ($\mu = \mu_b = \mu_t$), the dynamic simulation was used to predict the terrestrial righting time for varying tail length l_t and coefficient of friction μ. In contrast to aerial righting, the terrestrial righting time results in Figure 5.5b show that t_r does not change much with varying l_t. The greatest effect of tail length is observed in the $\mu = 0.5$ case, in which increasing l_t from 7 cm to 15 cm increases t_r by 37 ms. Righting time is far

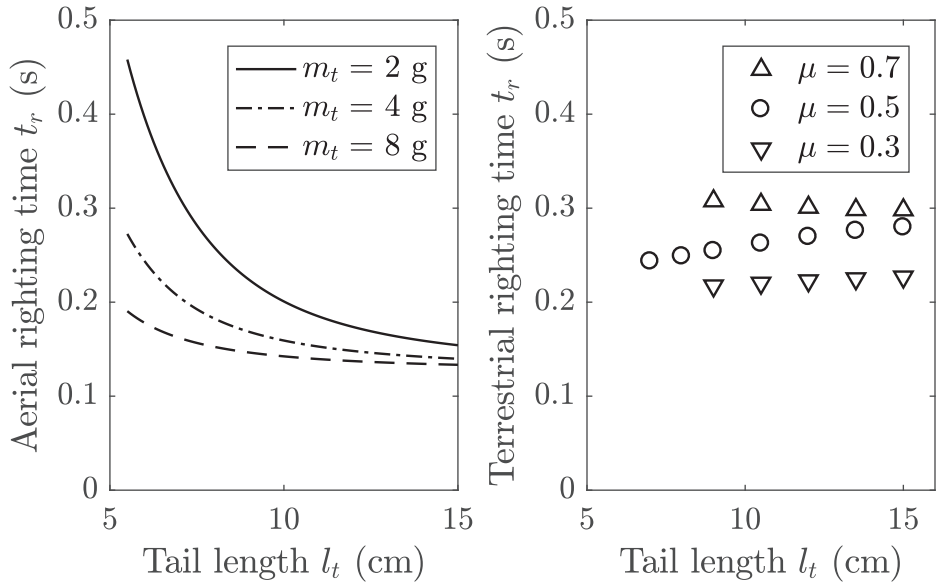


Figure 5.5: Comparison of the time to perform a 180° roll reorientation of a robot body for (a) aerial self-righting with an inertial tail of varying mass and length and (b) terrestrial righting with a low-mass tail of varying length on surfaces with varying coefficient of friction $\mu = \mu_b = \mu_t$.

more sensitive to the coefficient of friction μ—for a tail length $l_t = 9$ cm, increasing μ from 0.3 to 0.7 increases t_r by 90 ms. Overall, terrestrial righting over the range of l_t and μ values takes 84–174 ms more time than the fastest aerial righting case.

5.2 Terrestrial Tailed Self-Righting Experiments

5.2.1 Open-Loop Self-Righting Performance Tests

The self-righting performance of VelociRoACH was tested by executing an open-loop tail control sequence while inverted. A sequence of high-speed video frames (taken at 300 fps) are shown for a representative open-loop self-righting trial in Figure 5.6. In this experiment, the robot started inverted on a flat wood surface with its tail against the ground. Using a PID controller with feedback on tail position (measured with a magnetic rotary encoder), the robot applied an input voltage to swing its tail 180° clockwise. As pictured in the frame sequence, the tail pushes against the ground, causing the robot body to roll counterclockwise and self-right.

Telemetry data for ten repeated open-loop self-righting trials on wood are shown in Figure 5.7. The telemetry plots show the time trajectories of the body roll angle (measured

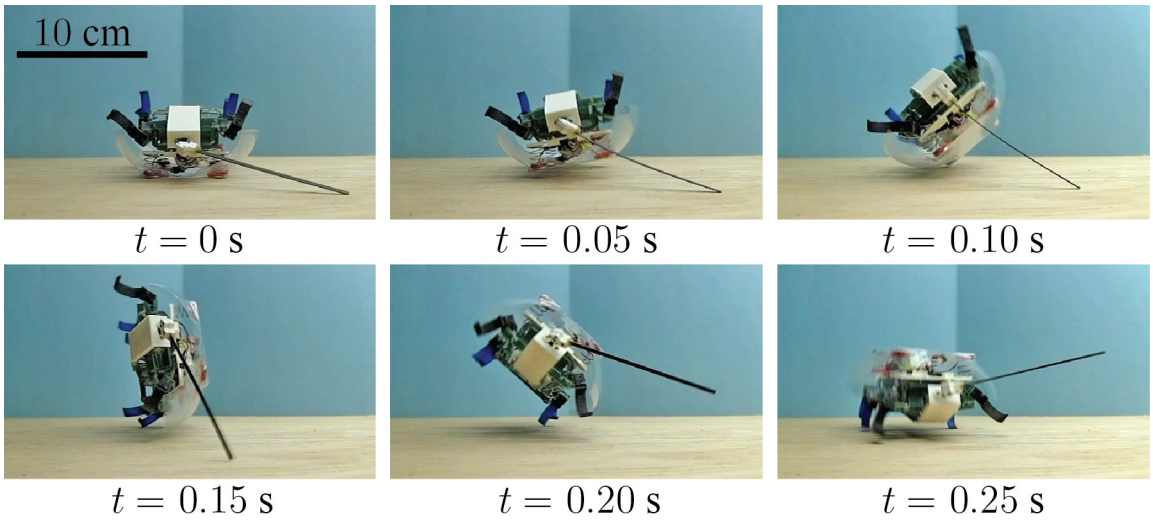


Figure 5.6: High-speed camera frame sequence of a VelociRoACH robot with shell and active tail performing a dynamic self-righting maneuver on wood.

using the onboard accelerometer and gyroscope), the tail rotation angle relative to the body (the zero reference for θ_t is the initial contact angle), and the tail torque. The tail torque is calculated using (5.19) and the tail encoder measurements.

The leftmost vertical dotted line marks the start of righting. At this time, the tail torque decays from a maximum magnitude as the tail rotates clockwise and the body rotates counterclockwise. The middle dotted line marks the end of the period of useful tail work. After this time, the tail leaves the ground and the applied torque repositions the tail towards the desired angle $\theta_t - \theta_b = 180°$. Since the tail has little inertial leverage, it no longer accelerates the body, as indicated by the linear increase in body angle after this time. The rightmost dotted line marks the average time at which the body reaches 180°. After this time, the left legs impact the ground and the robot settles onto its legs. For the wood surface experiments, the average righting time was 274 ms, with a standard deviation of 7.71 ms. Compared to the dashed simulation result ($\mu_b = 0.4$, $\mu_t = 0.5$), open-loop self-righting on wood was on average 41 ms slower. The planar model may underpredict righting time because in the experiments, the tail produced pitch and yaw motions outside of the roll plane. These higher dimensional dynamics could contribute to the more gradual roll angle acceleration of the robot body in the experiments relative to the model.

Open-loop tail-assisted self-righting was tested on the seven surfaces shown in Figure 5.8. Table 5.2 shows experiment righting times (average ± standard deviation) and success rates over ten trials for self-righting on each surface. The surface friction coefficients were determined from inclined plane tests measuring static friction—body friction μ_b was measured for the polycarbonate shell on the surface, and tail friction μ_t was measured for the polyurethane C-legs of the robot on the surface. The C-leg friction measurement approximates the increased effective friction of the tail from engaging surfaces with significant roughness (e.g.

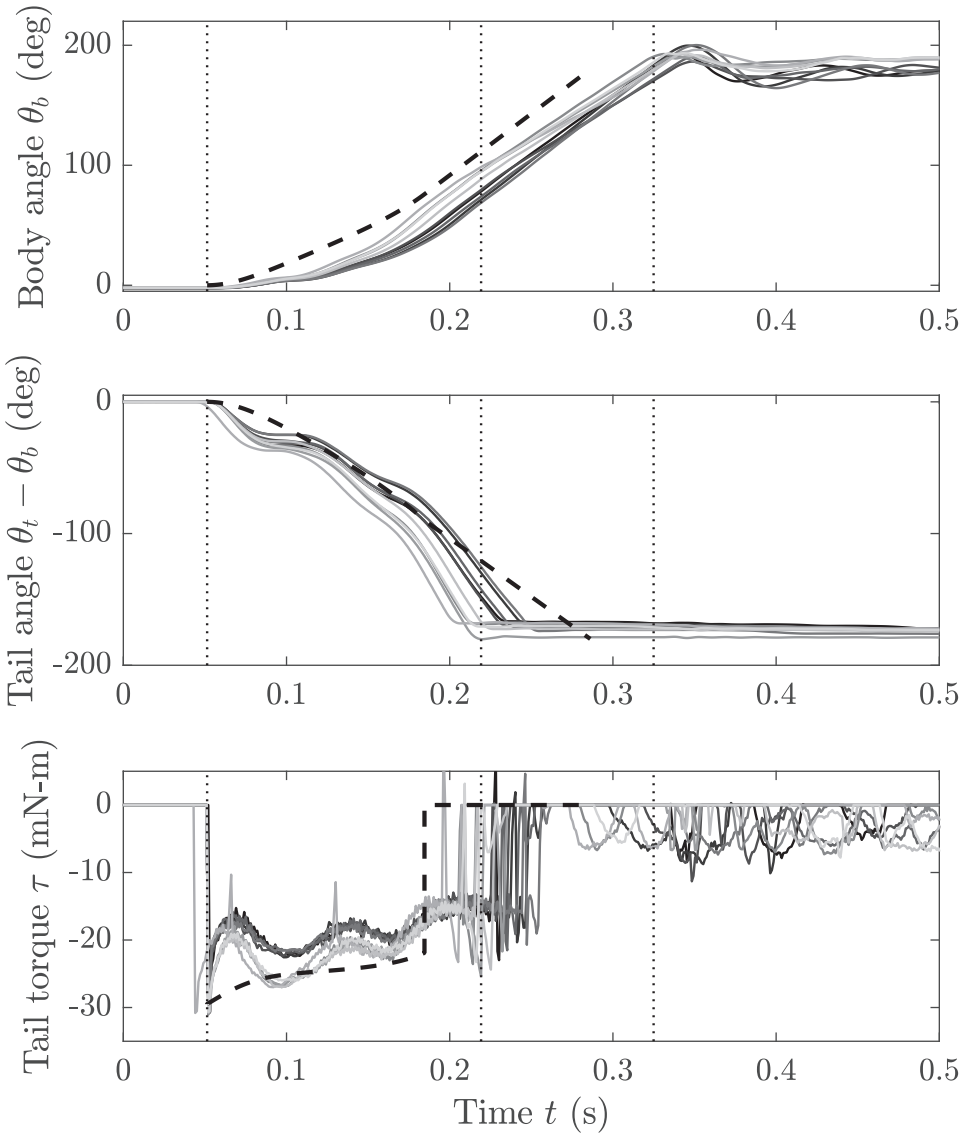


Figure 5.7: Robot telemetry for ten repeated trials of open-loop tail-assisted self-righting on wood. The vertical dotted black lines mark the start of righting, the end of the period of tail work, and the end of righting. The dashed black line is the dynamic simulation result.

carpet and rock surfaces). The righting times from the dynamic simulation are also shown. Note that the model results with an asterisk had modified initial conditions—due to the high tail friction, the simulation executions from zero initial velocity resulted in a sticking tail with non-physical contact forces. To numerically resolve these simulation cases, an initial horizontal velocity of $\dot{y}(0) = -12.5$ cm/s was used, which is up to 13% of the maximum body slip velocity.

For the more uniform wood, polystyrene, and carpet surfaces, lower body friction and

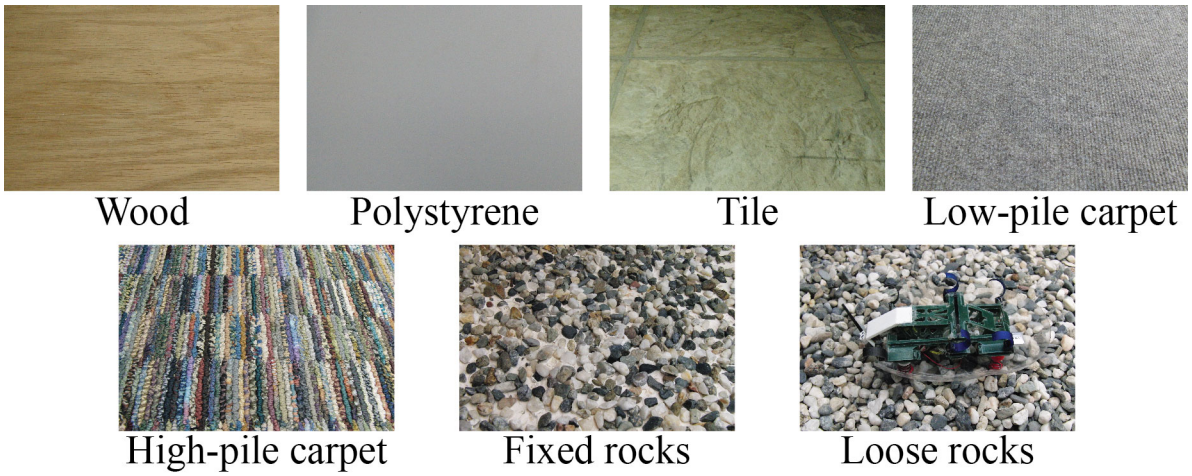


Figure 5.8: Surfaces used in open-loop tail-assisted self-righting experiments.

Table 5.2: Tail-assisted righting performance on various surfaces

Surface	C.o.F. μ_b/μ_t	Model t_r (ms)	Experiment t_r (ms)	Successes
Wood	0.4/0.5	235	274 ± 7.71	10/10
Polystyrene	0.3/0.3	217	264 ± 15.8	10/10
Tile	0.35/0.45	226	336 ± 51.7	10/10
Low-pile carpet	0.25/1	214*	259 ± 41.3	10/10
High-pile carpet	0.35/1	229*	256 ± 35.0	10/10
Fixed rocks	0.35/1.2	231*	292 ± 65.8	9/10
Loose rocks	0.35/1.2	231*	358 ± 138	8/10

higher tail friction are correlated with faster righting times. The fastest average righting time was on high-pile carpet ($t_r = 256$ ms). For the wood, polystyrene, and low-pile carpet surfaces, the simulation matches the trend in righting times, but consistently underpredicts righting times by 39–47 ms.

The surfaces with more variation in roughness and appearance (tile, fixed rocks, loose rocks) had the highest average righting times with relatively large spreads across the ten trials. The tile surface has millimeter-scale surface variations and the rock surfaces have centimeter-scale rocks either fixed in a single layer or loosely packed in multiple layers. Due to the variability of these surfaces, the tail can intermittently lose surface contact, which results in slower average righting times than predicted by the model. For the fixed and loose rock surfaces, the loss of tail effectiveness was sometimes so severe that the robot failed to right. An example trial of failed self-righting on loose rocks is shown in the high-speed video frame sequence in Figure 5.9. In these failure cases, the robot could still swing its tail again in another self-righting attempt.

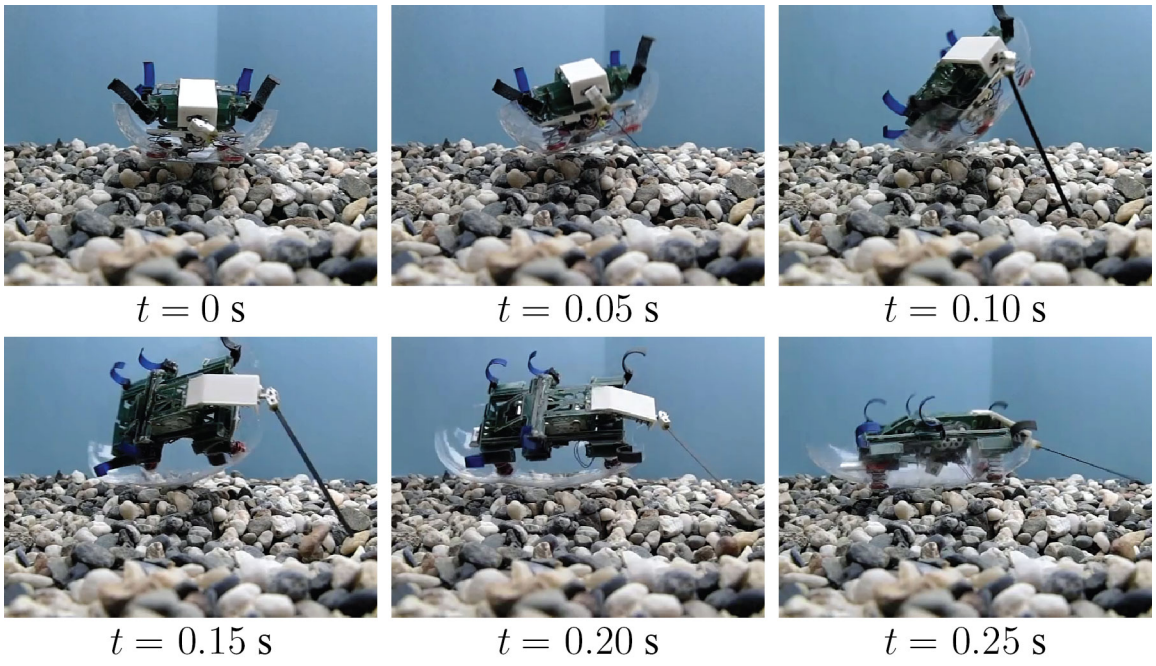


Figure 5.9: High-speed camera frame sequence of a VelociRoACH robot with shell and active tail failing to self-right after a single tail swing on loose rocks.

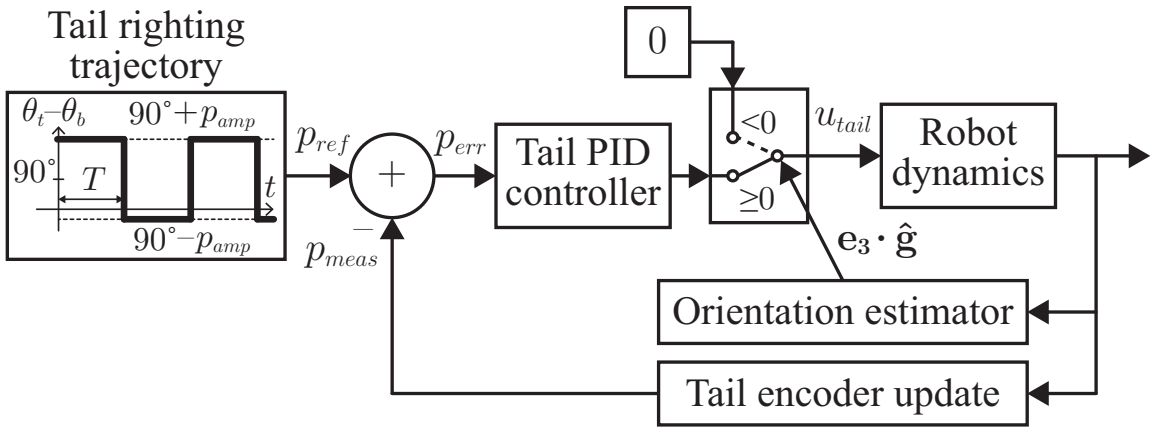


Figure 5.10: Autonomous tailed self-righting reflex control block diagram.

5.2.2 Autonomous Self-Righting Reflex on Unstructured Terrain

In addition to open-loop tests of tail-assisted self-righting, an autonomous self-righting reflex was demonstrated as VelociRoACH walked down a paper-covered obstacle with multiple step drops on the order of the robot's body length. The control strategy for this autonomous behavior is shown in the block diagram in Figure 5.10. Telemetry data from the robot during this experiment is shown in Figure 5.11 and a camera frame sequence is shown in

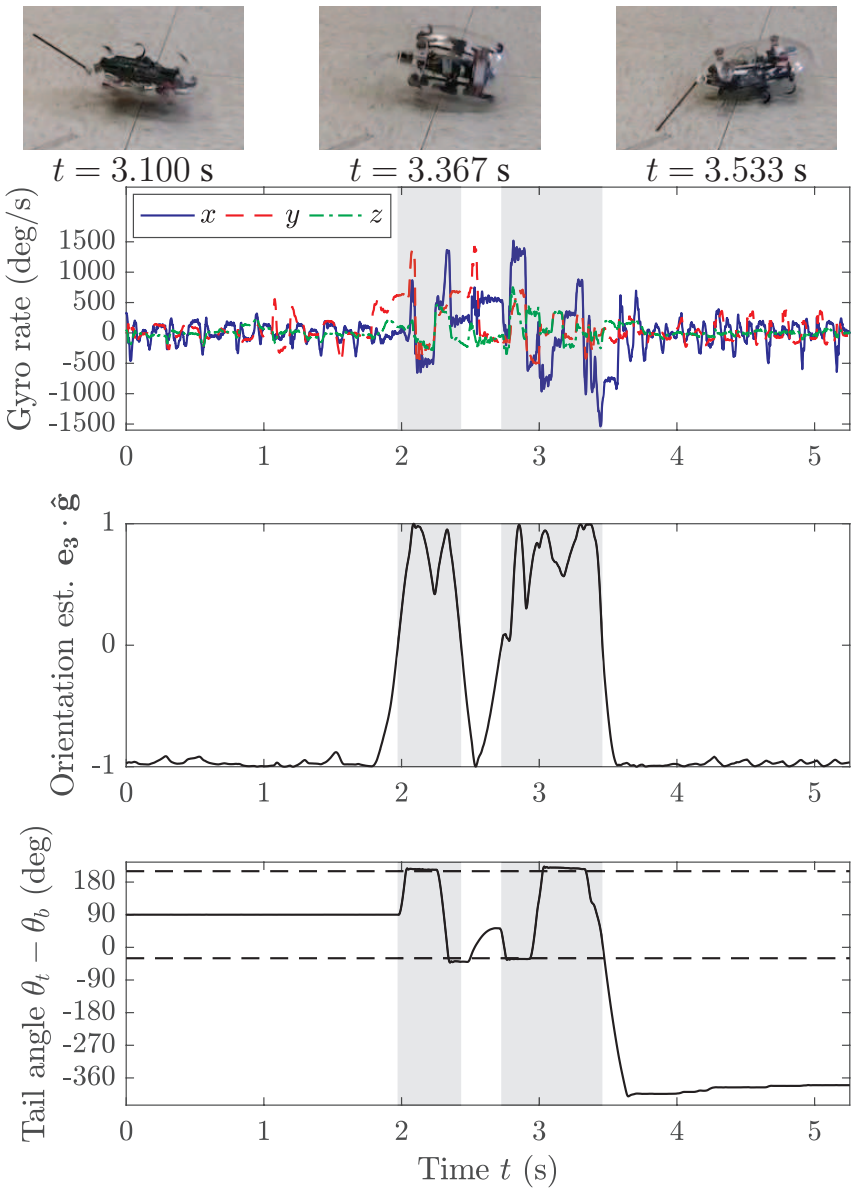


Figure 5.11: VelociRoACH robot telemetry for an autonomous tailed self-righting reflex while walking down a step obstacle with a stride frequency of 4 Hz. The shaded time intervals are when the robot detects that it is inverted. In the tail angle plot, the dashed lines at $-30°$ and $210°$ indicate the target tail angles.

Figure 5.12. With the robot's legs following a bounding gait with a stride frequency of 4 Hz, a pre-programmed tail righting trajectory is activated during inversion. The trajectory p_{ref} periodically swings the tail over the top of the robot and is parameterized by the swing period $T = 0.4$ s and the swing amplitude $p_{amp} = 120°$ relative to the vertical tail position $\theta_t - \theta_b = 90°$. Using an onboard orientation estimator giving roll-pitch-yaw Euler

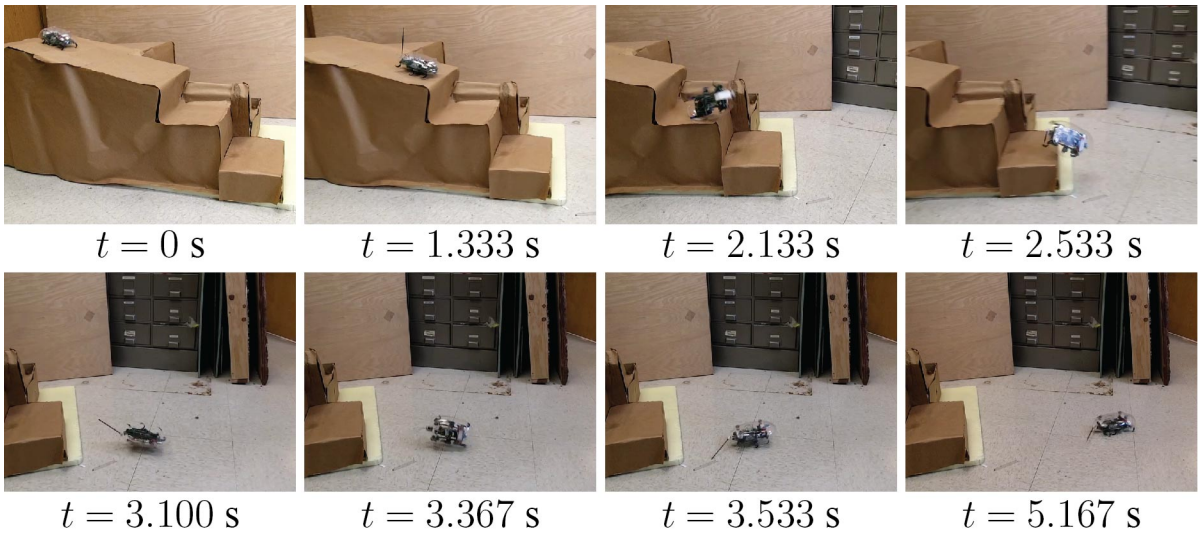


Figure 5.12: Camera frame sequence of an autonomous tailed self-righting reflex after VelociRoACH walks off an obstacle with steep drop-offs.

angles (initialized with the accelerometer, then propagated forward in time with integrated gyroscope measurements), the tail PID controller is activated when the robot's body-fixed vertical vector $\mathbf{e_3}$ is aligned with the normalized gravity vector $\hat{\mathbf{g}}$. Using feedback on the tail position p_{meas}, the tail PID controller applies the motor control signal u_{tail} until the robot is upright.

As shown in Figures 5.11 and 5.12, the autonomous self-righting reflex engages during locomotion whenever the robot's tumbling motion causes it to invert. In the second shaded time interval of inversion, the robot successfully self-rights at the bottom of the obstacle and walks forward.

5.3 Self-Righting Performance Comparison

The dynamic reorientation performance of VelociRoACH with tail is compared to other robot platforms with tail-like appendages in Table 5.3. This table shows the reorientation axis, method of reorientation, reorientation condition, reorientation time (average ± standard deviation), reorientation angle, and number of trials for the reorientation time statistics. The mass moment of inertia about the reorientation axis and the peak mechanical power of motors used for tail-assisted reorientation are also included as a means of comparison.

Tailbot and RHex with tail both perform aerial self-righting by swinging inertial tails with offset mass in the pitch plane to rotate their bodies by 90°. RHex with tail takes 2.5x longer to self-right compared to Tailbot even with 12.5x the available motor power and similar tail effectiveness, due to its 1000x greater body inertia. TAYLRoACH performs 90° turns by swinging an inertial yaw tail while running forward on low-friction tile. Because

Table 5.3: Comparison of robots with tail-like appendages that can rapidly reorient

	Tailbot [22]	RHex w/ tail [93]	TAYL-RoACH [82]	Cockroach-inspired robot [90]	Horseshoe crab robot [87]	Veloci-RoACH w/ tail [17]
Reorientation axis, method	Pitch, inertial	Pitch, inertial	Yaw, inertial	Pitch, contact	Roll, contact	Roll, contact
Condition	Aerial	Aerial	Low-friction tile	Flat surface	Surf zone	Carpet, loose rocks
Body inertia (kg-m^2)	154×10^{-6}	0.15	39.6×10^{-6}	110×10^{-6}	–	58.3×10^{-6}
Peak motor power (W)	4	50	2.5	0.88	0.5	0.57
Reorientation time (ms)	138 ± 1.09	350	225 ± 64.3	672 ± 41.7	2000	256 ± 35.0, 358 ± 138
Angle (deg)	90	90	90	180	180	180
Number of trials	5	1	10	3	1	10, 8

of the frictional energy dissipation of its legs sliding against the ground during the turn, TAYLRoACH takes 87 ms longer on average to reorient compared to Tailbot, with similar tail effectiveness, 62.5% of the motor power, and 25.7% of the body inertia. In addition, TAYLRoACH turns with significantly more variability in reorientation time compared to the aerial self-righting maneuver of Tailbot because of the stochastic nature of its leg-ground interactions.

The cockroach-inspired robot self-rights about its pitch axis on a flat surface using the outward unfolding of two wings driven by independent servo motors. The horseshoe crab robot self-rights about its roll axis in a surf zone with wet sand and rock terrain using a tail driven by two servo motors. VelociRoACH with tail performs terrestrial self-righting using a single tail motor substantially faster than the cockroach-inspired and horseshoe crab robots, on terrain types ranging from carpet to loose rocks. Compared to Tailbot (which performs the fastest reorientation maneuver among the other robots), VelociRoACH with tail self-rights slightly faster on carpet (with 14.3% of the motor power and 37.9% of the body inertia of Tailbot), but has more variability in righting time due to differences in tail-ground engagement from trial to trial. VelociRoACH with tail can also self-right on loose rock terrain, with a 102 ms increase in average righting time and a 3.9x increase in the standard deviation of righting times compared to self-righting on carpet.

Overall, the presented robot performs a 180° roll reorientation faster than the other platforms that use inertial tails or tail contact to reorient about pitch, roll, or yaw axes.

Chapter 6

Tailed Turning with Terrain Contact

Two approaches are applied to the newly-developed tail contact turning strategies. First, an equilibrium analysis is performed on a simplified model of a legged robot turning in the yaw plane to determine the forward speed and angular velocity of steady-state tail drag turns. Next, experimental time trajectories of forward velocity and angular motion resulting from LoadRoACH impacting its tail against the ground are presented to qualitatively explain this turn method.

Measured parameters of the LoadRoACH robot used in the turning experiments in Section 6.3 are shown in Table 6.1.

6.1 Tail Drag Turning Analysis

6.1.1 Formulation of Steady-State Turning Equilibria

Free body diagrams of a legged robot performing a steady-state tail drag turn are shown in Figure 6.1. The legs of the robot are assumed to drive the robot directly forward in the $\mathbf{e_1}$ direction at a speed of v_{Gx}, while it turns about its local vertical axis $\mathbf{e_3}$ at an angular rate of $\dot{\psi}$. In this steady-state analysis, the forces that act on the robot are assumed to cancel out so that the robot undergoes zero acceleration in translation and rotation about its body axes $\{\mathbf{e_1}, \mathbf{e_2}, \mathbf{e_3}\}$ fixed to its center of mass (C.o.M.), except for the centripetal turning acceleration $\dot{\psi}^2 r\mathbf{e_2}$, where $r = \frac{v_{Gx}}{\dot{\psi}}$ is the turning radius. Gravitational force $m\mathbf{g}$ acts vertically downward, the compliant tail drags against the ground with force $\mathbf{F_t}$ satisfying Coulomb friction, and the legs produce a net force $\mathbf{F_b}$ within the robot's base of leg support. The body and tail forces act at contact locations of $\mathbf{r_{P,b}}$ and $\mathbf{r_{P,t}}$ respectively. The legs must produce enough force along the forward direction of travel to counteract the tail dragging force, and the legs and tail must produce a net cornering force towards the center of the turn ($\mathbf{e_2}$) to counteract the centripetal inertial force $m\dot{\psi}^2 r$ acting in the $-\mathbf{e_2}$ direction.

The force balance equations of the system are given below for the $\mathbf{e_1}$ (6.1), $\mathbf{e_2}$ (6.2), and

Table 6.1: LoadRoACH with shell and tail parameters.

Parameter name	Symbol	Value
Mass	m	82.0 g
Mass moments of inertia	J_x	398 g-cm^2
	J_y	1424 g-cm^2
	J_z	1739 g-cm^2
Body C.o.M. displacement from back	x_G	4.5 cm
Body C.o.M. height from ground	z_G	3.5 cm
Tail length	l_t	9 cm
Tail stiffness	k_t	6.6 N/m
Tail cone angle	β_t	20°
Motor mounting angle	α_m	20°
Tail base displacement from C.o.M.	x_m	−6.8 cm
Tail base height above ground	z_m	4.2 cm
Tail angle for ground contact	θ_{t0}	131°
Drive no-load speed on carpet	v_{nl}	70 cm/s
Drive stall force on carpet	F_s	30% body weight
Leg C.o.F. on carpet	μ_b	1.25
Tail C.o.F. on carpet	μ_t	0.7

$\mathbf{e_3}$ (6.3) directions.

$$m\dot{v}_{Gx} = 0 = F_{bx} + F_{tx} \tag{6.1}$$

$$m\dot{\psi}^2 r = F_{by} + F_{ty} \tag{6.2}$$

$$mg = F_{bz} + F_{tz}, \tag{6.3}$$

where the subscripts (x, y, z) denote $(\mathbf{e_1}, \mathbf{e_2}, \mathbf{e_3})$ components of $\mathbf{F_b}$ and $\mathbf{F_t}$. The moment balance equations are given below for the $\mathbf{e_1}$ (6.4), $\mathbf{e_2}$ (6.5), and $\mathbf{e_3}$ (6.6) directions:

$$m\dot{\psi}^2 r z_{P,t} = F_{bz} y_{P,b} + F_{tz} y_{P,t} \tag{6.4}$$

$$0 = F_{bz} x_{P,b} + F_{tz} x_{P,t} \tag{6.5}$$

$$0 = F_{by} x_{P,b} - F_{bx} y_{P,b} + F_{ty} x_{P,t} - F_{tx} y_{P,t}, \tag{6.6}$$

where $(x_{P,b}, y_{P,b}, z_{P,b})$ and $(x_{P,t}, y_{P,t}, z_{P,t})$ denote $(\mathbf{e_1}, \mathbf{e_2}, \mathbf{e_3})$ components of $\mathbf{r_{P,b}}$ and $\mathbf{r_{P,t}}$. Note that in these equations, (6.1) and (6.2) were applied. Also note that $z_{P,t} = z_{P,b}$ because the tail and legs are both contacting the horizontal ground plane.

To determine the possible velocities $(v_{Gx}, \dot{\psi})$ of steady-state turns depending on robot system parameters, the 6 force/moment balance equations of the system must be solved by reducing the system unknowns to 6. First, the tail contact location can be determined from

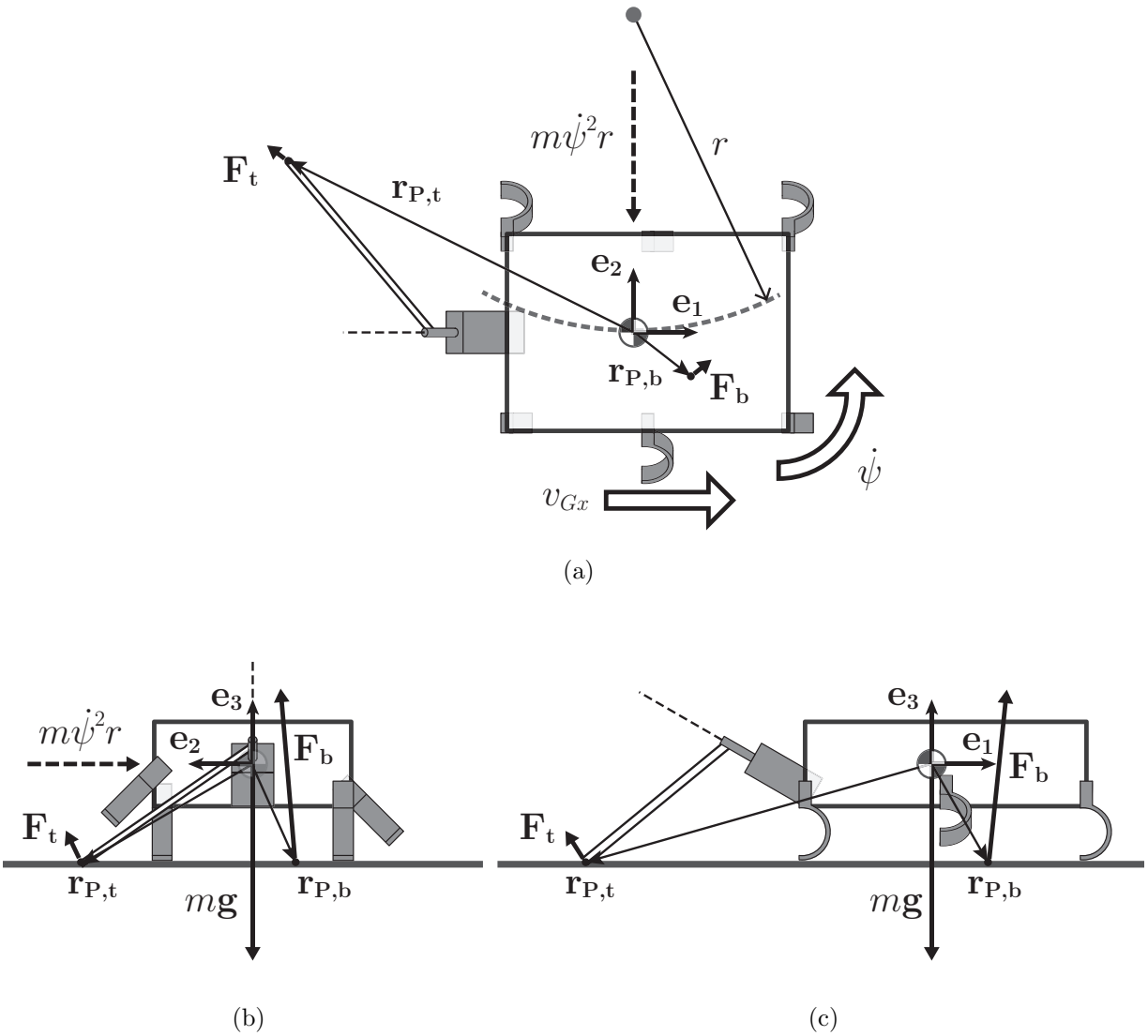


Figure 6.1: Free body diagrams of (a) overhead, (b) back, and (c) side views of a legged robot performing a sustained turn while dragging a tail.

the geometric parameters shown in Figure 6.2. The tail motor is mounted at an angle α_m about $\mathbf{e_2}$. The tail has length l_t, and is mounted so that it sweeps out a cone with angle β_t directed along the $-\mathbf{e_1^m}$ axis in the motor frame $\{\mathbf{e_1^m}, \mathbf{e_2^m}, \mathbf{e_3^m}\}$. The tail motor rotates the tail with counterclockwise rotation angle θ_t. To determine the tail contact location, the tail angle to contact the ground θ_{t0} is computed from the tail geometry. Below, (6.7), (6.8), and (6.9) are the components of the tail contact location relative to the tail base in the motor frame. Because the tail base height z_m is known from the robot geometry, (6.10) can be solved to determine θ_{t0} according to (6.11).

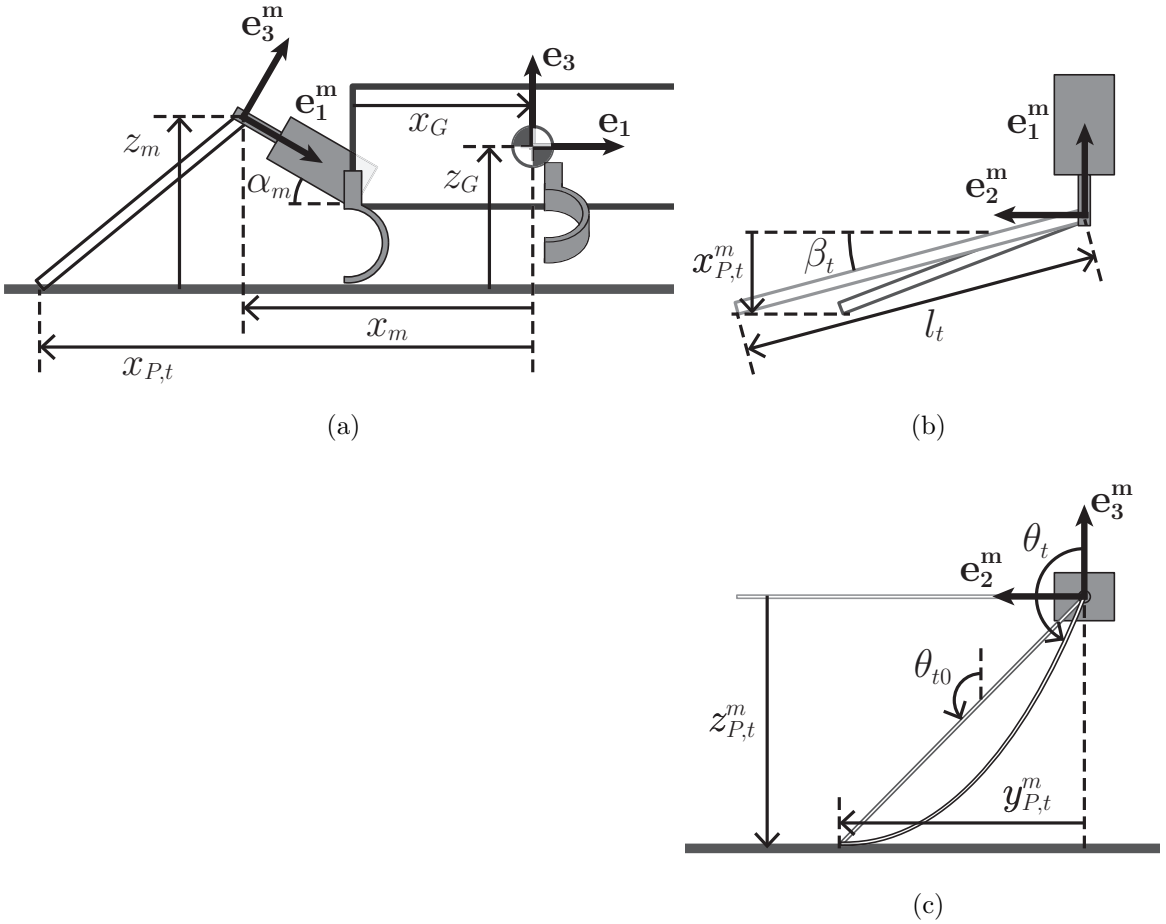


Figure 6.2: Geometric parameters for tail drag turning with (a) side, (b) overhead motor frame, and (c) back motor frame views.

$$x_{P,t}^m = -l_t \sin\beta_t \tag{6.7}$$

$$y_{P,t}^m = l_t \cos\beta_t \sin\theta_{t0} \tag{6.8}$$

$$z_{P,t}^m = l_t \cos\beta_t \cos\theta_{t0} \tag{6.9}$$

$$z_m = x_{P,t}^m \sin\alpha_m - z_{P,t}^m \cos\alpha_m \tag{6.10}$$

$$\sin\left(\theta_{t0} - \frac{\pi}{2}\right) = \frac{z_m \sec\alpha_m + l_t \sin\beta_t \tan\alpha_m}{l_t \cos\beta_t}. \tag{6.11}$$

From these tail geometry calculations, the contact locations have been determined and can be transformed to the body frame, with the exception of the $\mathbf{e_1}$, and $\mathbf{e_2}$ components of $\mathbf{r_{P,b}}$, which depend on moment balances. The tail force can be determined from the assumed

relations below:

$$\mathbf{F_t} = -\frac{\mu_t F_{tz}}{||\mathbf{v_{P,t}}||}\mathbf{v_{P,t}} + F_{tz}\mathbf{e_3} \tag{6.12}$$

$$\mathbf{v_{P,t}} = (v_{Gx} - y_{P,t}\dot{\psi})\mathbf{e_1} + x_{P,t}\dot{\psi}\mathbf{e_2} \tag{6.13}$$

$$F_{tz} = k_t l_t \sin\Delta\theta_t, \Delta\theta_t = \theta_t - \theta_{t0}. \tag{6.14}$$

The components of $\mathbf{F_t}$ in the ground plane satisfy the Coulomb friction relation (6.12), which states that the magnitude of this planar force is the tail sliding coefficient of friction μ_t multiplied by the vertical tail force F_{tz} and its direction opposes $\mathbf{v_{P,t}}$ (6.13). The tail is compliant in bending about the motor rotation axis, which results in an applied spring force against the ground as θ_t increases past θ_{t0}. The magnitude of the vertical contact force is controlled according to the force-deflection relation in (6.14), with linear tail stiffness k_t multiplying $l_t \sin\Delta\theta_t$, where $\Delta\theta_t$ is positive as the tail deflects against the ground as shown in Figure 6.2c.

Finally, an assumption is made on the robot's leg drive capabilities under loading. For a given gait and surface, the robot is assumed to run at a forward speed of v_{nl} under zero tail drag loading, which then linearly decreases to zero as the backward tail drag load decreases to $F_{tx} = -F_s$. Because $F_{bx} = -F_{tx}$ from (6.1), this results in the force-speed relation for the drive actuation below:

$$F_{bx} = F_s\left(1 - \frac{v_{Gx}}{v_{nl}}\right). \tag{6.15}$$

Applying the above constraints on forces and displacements, the force and moment balances (6.1)–(6.6) can be solved for the 6 unknowns $(x_{P,b}, y_{P,b}, F_{by}, F_{bz}, v_{Gx}, \dot{\psi})$. Because of the Coulomb friction relation (6.12), this solution reduces to solving a nonlinear system of two equations to determine v_{Gx} and $\dot{\psi}$ of the steady-state turn, which is done using `vpasolve` in MATLAB.

6.1.2 Steady-State Turning Performance

Using the formulation of steady-state turning equilibria and the parameters in Table 6.1, the forward speed v_{Gx} and yaw angular velocity $\dot{\psi}$ were determined as a function of tail deflection against the ground $\Delta\theta_t$. The results are shown in Figure 6.3a and Figure 6.3b. Stability analysis of the two determined solution branches revealed that the branch with higher turn velocities (marked by red X's) represents unstable equilibria, and the lower branch (marked by blue circles) represents stable equilbria. The stable branch represents physically achievable steady-state turns, in which the tail dragging force rejects perturbations from the turning equilibrium. As $\Delta\theta_t$ increases, the forward velocity of the steady-state turn decreases from the unloaded value of $v_{nl} = 70$ cm/s as the tail drag force increases according to the force-deflection relation of the tail and the tail-ground coefficient of friction $\mu_t = 0.7$. If $\Delta\theta_t$ exceeds 25°, the curves terminate. Although steady-state turns still exist past this tail deflection, the applied vertical tail force would cause the body to tip (with $|y_{P,b}| > 3.5$ cm),

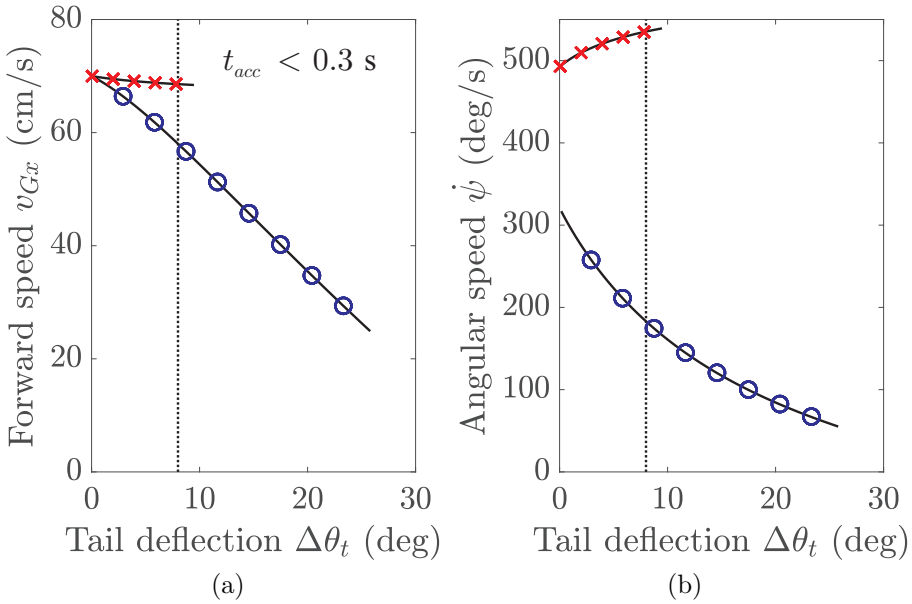


Figure 6.3: Steady-state turning equilibria from the dynamic analysis of dragging a tail with frictional contact. For each tail angle deflection $\Delta\theta_t$, there exists either a stable steady-state turn (blue circles), an unstable steady-state turn (red X's), or no steady-state turn. (a) Forward velocity and (b) angular velocity for each turn.

which violates an assumption of the steady-state turning model. As a physical check on the model, the minimum required leg-ground coefficient of friction to prevent slipping during the turn was determined to be 0.4, which is exceeded by the measured value of $\mu_b = 1.25$ for movement on carpet.

To apply the results of this steady-state tail drag turn analysis to an actual robot, dynamic conditions have to be applied to select a turn that is fast enough for rapid steering. To initiate turning, the robot runs straight forward and then touches its tail to the ground with a set tail deflection. The time to accelerate into the turn can be determined from an impulse-momentum calculation about the $\mathbf{e_3}$ axis:

$$J_z\dot{\psi} = \int_0^{t_{acc}} M_z dt. \tag{6.16}$$

Assuming the yaw moment M_z linearly decays from a maximum value of $M_{z,max} = \mu_t F_{tz} y_{P,t}$ to zero as the robot enters the turn, the time to accelerate t_{acc} can be approximated as $\frac{2J_z\dot{\psi}}{M_{z,max}}$. If the robot is required to turn quickly, then there is a lower threshold on $\Delta\theta_t$ for tail drag turning that meets this acceleration constraint. In Figure 6.3, the vertical dotted line at $\Delta\theta_t = 8°$ marks the threshold past which the robot can initiate a tail drag turn faster than $t_{acc} = 0.3$ s. With a measured maximum tail motor rotation rate of 10 Hz during free run, the robot requires $t_{switch} = 0.073$ s to swing its tail through an angle $2\theta_{t0} = 262°$ to switch tail drag turn direction. These physical limitations of the robot system impose a time

delay of $t_{acc} + t_{switch} = 0.373$ s before tail drag turning at the maximum projected speed can be achieved in the desired direction.

With a reasonable constraint on turning acceleration time Figure 6.3 predicts that the maximum tail drag turning performance of the robot system is bounded by an upper threshold of $v_{Gx} = 58$ cm/s and $\dot{\psi} = 180$ deg/s. However, this steady-state model does not consider that leg-ground interaction forces can impede yaw rotation of the robot. Therefore, a more realistic prediction of tail drag turn performance can be determined by assuming that the dragging tail only has a maximum turning effect when the robot's legs are off the ground or exerting small forces on the ground. Then, a better prediction of the achievable $\dot{\psi}$ for tail drag turning is the value in Figure 6.3 multiplied by an aerial duty factor $D_{aerial} \in [0, 1]$. As a baseline comparison, DASH runs with an aerial phase $D_{aerial} = 0.3$ [9], which results in a predicted tail drag turn rate of 54 deg/s.

6.2 Tail Impact Turning Analysis

6.2.1 Impulse-Momentum Applied to Maneuver

A free body diagram of a legged robot performing a transient tail impact turn is shown in Figure 6.4. As is qualitatively represented in the diagram, controlling to a commanded tail velocity $\dot{\theta}_{t,des}$ swings the tail into the ground, which generates large tail contact forces that act to rotate the robot with an angular velocity profile $\boldsymbol{\omega}(t) = \omega_x(t)\mathbf{e_1} + \omega_y(t)\mathbf{e_2} + \omega_z(t)\mathbf{e_3}$.

To analyze the net impulse applied by the combination of the tail and leg contact forces from collected experimental data, impulse-momentum theory is applied to the 3D rotational

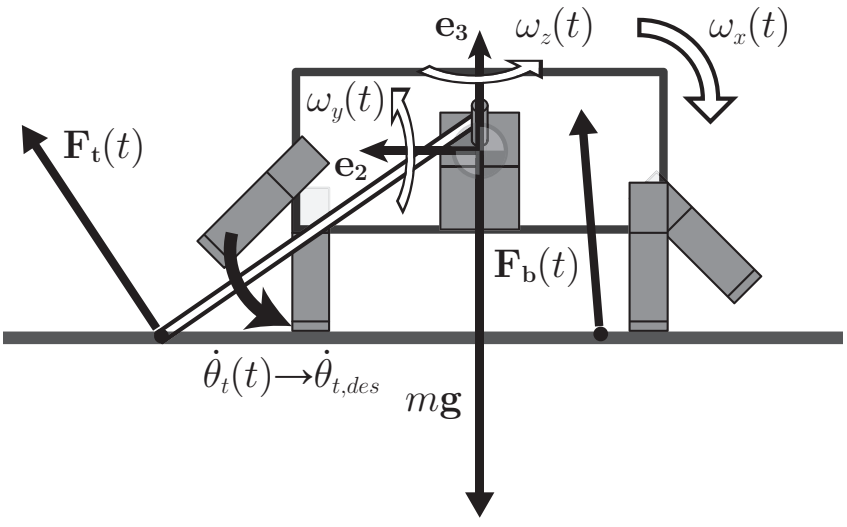


Figure 6.4: Free body diagram of a transient tail impact maneuver causing 3D rigid body rotation of a legged robot.

dynamics of the system:

$$\Delta L_x(t) = \int_0^t \left(J_x \dot{\omega}_x(\tau) + (J_z - J_y)\omega_y(\tau)\omega_z(\tau)\right) d\tau \tag{6.17}$$

$$\Delta L_y(t) = \int_0^t \left(J_y \dot{\omega}_y(\tau) + (J_x - J_z)\omega_x(\tau)\omega_z(\tau)\right) d\tau \tag{6.18}$$

$$\Delta L_z(t) = \int_0^t \left(J_z \dot{\omega}_z(\tau) + (J_y - J_x)\omega_x(\tau)\omega_y(\tau)\right) d\tau, \tag{6.19}$$

where (J_x, J_y, J_z) are the mass moments of inertia of the robot about its body-fixed axes (given in Table 6.1) and the integrand expressions on the right hand sides of (6.17), (6.18), and (6.19) are the net moments acting on the robot in the $\mathbf{e_1}$, $\mathbf{e_2}$, and $\mathbf{e_3}$ directions. The result is the cumulative angular impulse during the maneuver $(\Delta L_x(t), \Delta L_y(t), \Delta L_z(t))$, which helps to visualize the effect of the impulsive moment that the tail applies to rotate the robot.

6.2.2 Experimental Analysis

Robot telemetry from an experiment in which the robot impacted its tail against the ground while running forward on carpet is shown in Figure 6.5. In this maneuver, the robot swung its tail counterclockwise to impact the ground at a commanded rotation rate of 8 Hz. The telemetry data show that a 0.1 s duration negative step in the yaw impulse (ΔL_z) begins at a time of 0.55 s within the tail impact window (between the dotted vertical lines), which acts to rotate the robot about $-\mathbf{e_3}$ with decreasing yaw angle ψ. Because the tail impacts the ground at a contact point that is offset from the robot C.o.M. in the $-\mathbf{e_1}$ and $\mathbf{e_2}$ directions, it produces pitch (ΔL_y) and roll (ΔL_x) impulses that aggressively pitch the robot forward and roll the robot to the right. After the tail impact, gravity restores the robot back to a level posture and it resumes a periodic running gait. The collected motion tracking data of the robot's forward velocity shows that the robot almost slows to a stop after the tail impact, and returns to its nominal running speed 0.55 s after the tail impact maneuver started. The net effect of the tail impact is a $\Delta\psi = -90°$ turn clockwise after $\Delta t = 0.55$ s. The experimentally determined value of Δt gives the delay before the tail impact fully turns the robot and provides a reasonable constraint on the minimum feasible time interval between tail impact events. The effect of tail rotation rate on $\Delta\psi$ and Δt while running on different surfaces is characterized in Section 6.3.

6.3 Comparative Turning Experiments

6.3.1 Open-Loop Turning Performance

LoadRoACH carrying an active tail and shell with reflective markers for motion tracking was used to characterize the open-loop performance of the tailed turning strategies. Image

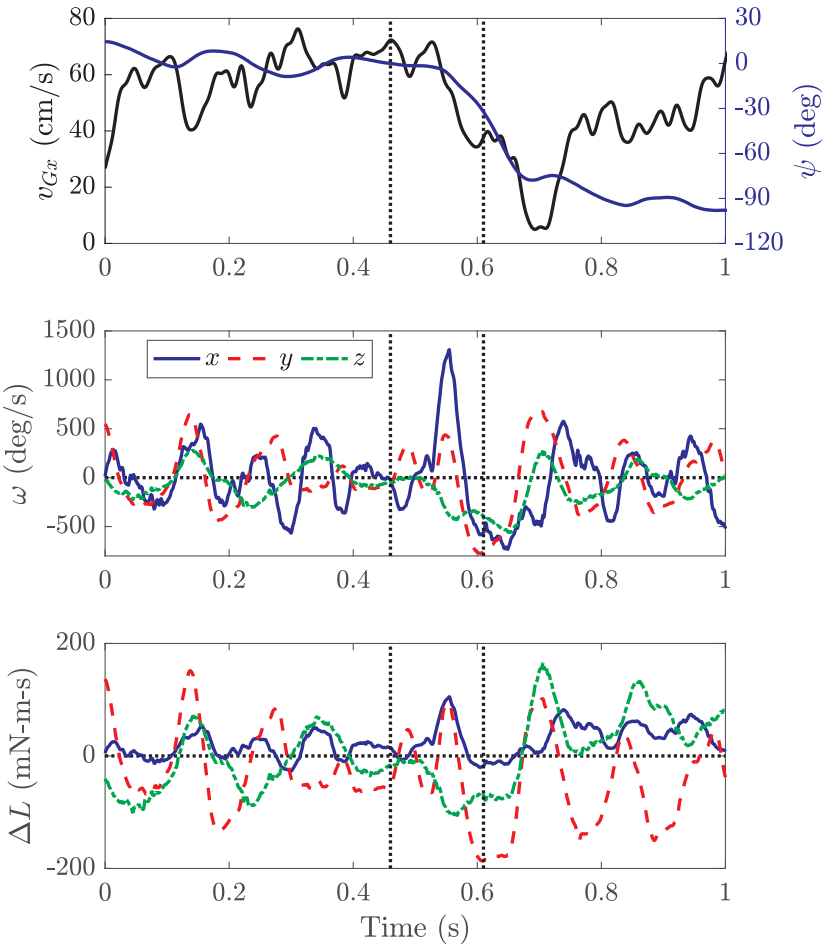


Figure 6.5: Motion tracking and robot telemetry data during a transient tail impact turn on carpet. In this maneuver, the robot swung its tail counterclockwise at a commanded rotation rate of 8 Hz. Top: Forward velocity v_{Gx} measured from the motion tracking system (left axis, black line) and yaw angle ψ from Euler angle updates using the robot's gyroscope measurements (right axis, blue line). Middle: body-fixed angular velocity (ω_x, ω_y, ω_z) measured by the robot's gyroscope. Bottom: Cumulative body-fixed angular impulse (ΔL_x, ΔL_y, ΔL_z) calculated from the gyroscope time series data. The dotted vertical lines mark the start of the tail swing in the air and the moment when the tail completes a full rotation.

sequences of representative trials of differential drive, tail drag, and tail impact turning on carpet are shown in Figure 6.6. Experimental open-loop turning performance results for LoadRoACH implementing differential drive, tail drag, and tail impact turning methods are shown in Figures 6.7a, 6.7b, and 6.9a. In each of these plots, the horizontal axis is the control parameter modulating the effect of the turning strategy. For differential drive, either the right or left leg side runs at a stride frequency of 10 Hz while the other leg side is decreased to $\{8, 5, 2, 0\}$ Hz. For tail drag, the robot runs using an alternating tripod gait with a stride

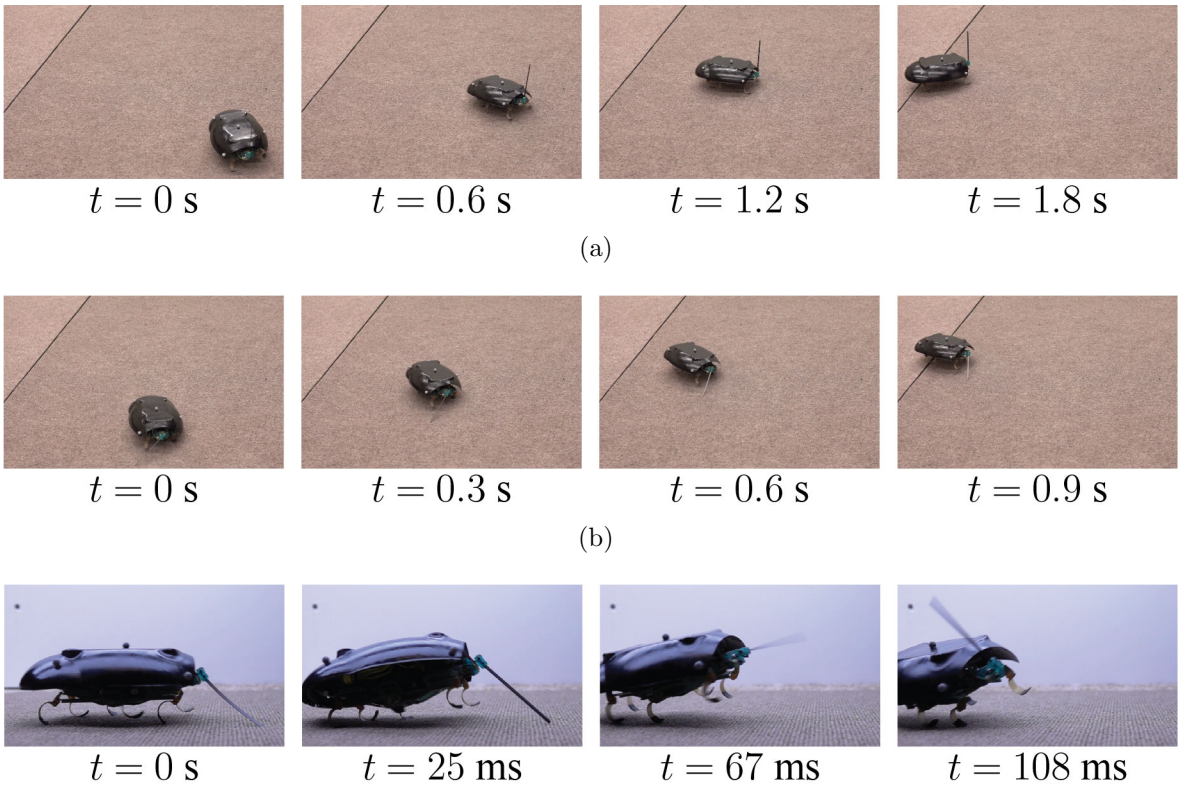


Figure 6.6: Video frame sequences of LoadRoACH implementing different turn methods while running on carpet. (a) Differential drive turning with a left stride frequency of 5 Hz and a right stride frequency of 10 Hz. (b) Tail drag turning with a counterclockwise tail deflection of 7°. (c) Tail impact turning with a counterclockwise tail rotation rate of 8 Hz.

frequency of 10 Hz and controls the position of its tail to apply up to a 40° tail deflection, where a negative value of $\Delta\theta_t$ indicates that the tail touches down clockwise on the ground (opposite to Figure 6.1). For the actual robot standing with left and right transmission cranks set to bottom dead center ($\varphi = 0°$, outer legs in mid stance), the value of the tail angle θ_{t0} at initial contact with the ground was determined to be 130° for counterclockwise tail rotation and $-125°$ for clockwise tail rotation. Tail deflection calibration tests with the tail contacting a load cell (*ATI* Nano43) were used to determine tail stiffness values k_t of 6.6 N/m for counterclockwise tail rotation and 8.0 N/m for clockwise tail rotation, which are valid for tail deflections $\Delta\theta_t$ of up to 20° in magnitude. For tail impact turning, the robot runs using a 10 Hz alternating tripod gait and then impacts its tail against the ground once, with a controlled tail rotation rate varying from 1 Hz to 8 Hz (a positive value indicates counterclockwise rotation).

The differential drive (Figure 6.7a) and tail drag (Figure 6.7b) turning strategies produce sustained turns. As expected, a positive stride frequency difference and a positive tail

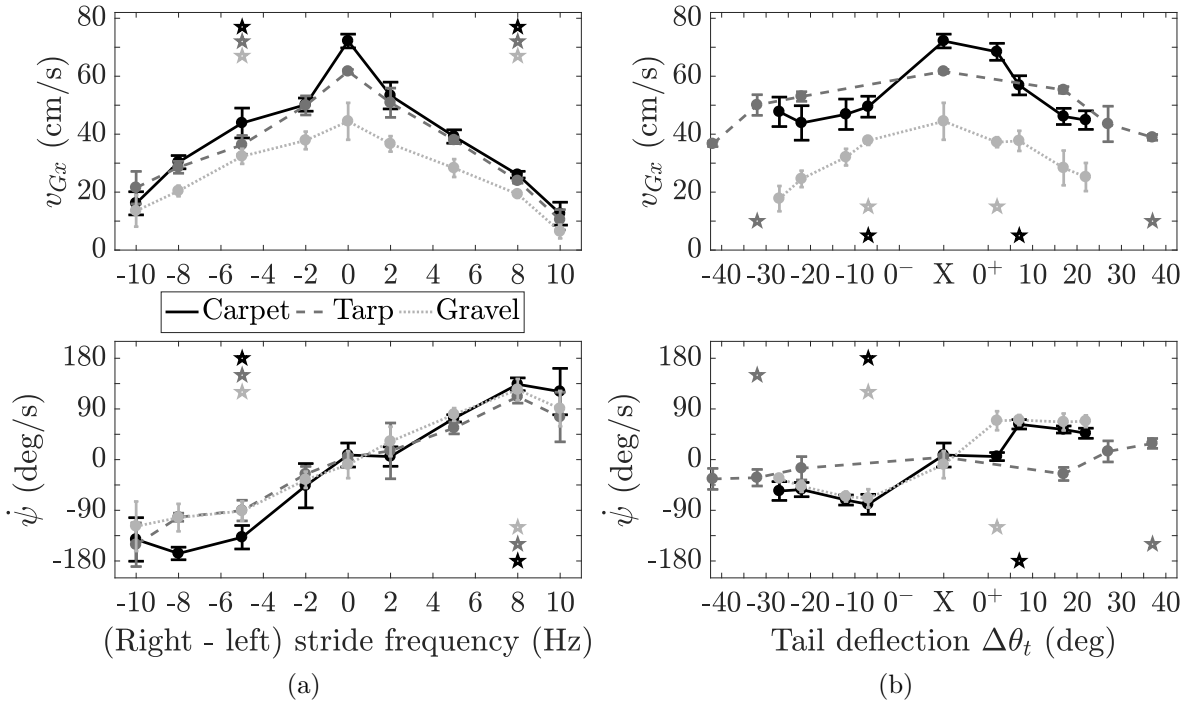


Figure 6.7: Forward speed v_{Gx} (measured from motion tracking) and angular rate $\dot{\psi}$ (measured from the robot's gyroscope) of LoadRoACH turning with sustained control effort through (a) differential drive and (b) tail drag turning methods. Each data point gives the experimental mean over at least 4 trials with error bars showing the sample standard deviation. Results are shown for carpet, tarp, and gravel surfaces. The stars mark the highest performance turn with regard to average maneuverability $v_{Gx}\dot{\psi}$.

deflection produce counterclockwise turns (positive $\dot{\psi}$), and the direction of the turn can be changed by switching the sign of the control action. In comparison to the analysis, the fastest experimental tail drag turn condition ($\Delta\theta_t = -7°$ on carpet) had an average forward velocity of 49 cm/s (84% of the analytical value) and an average angular velocity of -79 deg/s, which corresponds to the analytical projection scaled by an aerial duty factor of $D_{aerial} = 0.44$. In addition, increasing the tail deflection causes the forward velocity and angular velocity of the robot to decrease, but turning behavior for tail deflections past 25° is not modeled accurately by the analysis.

A relevant turning performance metric is maneuverability $\Gamma = v_{Gx}\dot{\psi}$. Turns with higher Γ allow the robot to redirect its heading quickly while maintaining a high forward speed. The starred test conditions in Figure 6.7 produced the highest maneuverability turns, and the resulting turn trajectories are shown in Figure 6.8. Table 6.2 shows the maximum sustained turning maneuverability for clockwise and counterclockwise turns (negative indicates clockwise, positive indicates counterclockwise). The values in this table are computed using the average velocities of the starred experiment conditions in Figure 6.7. For the carpet

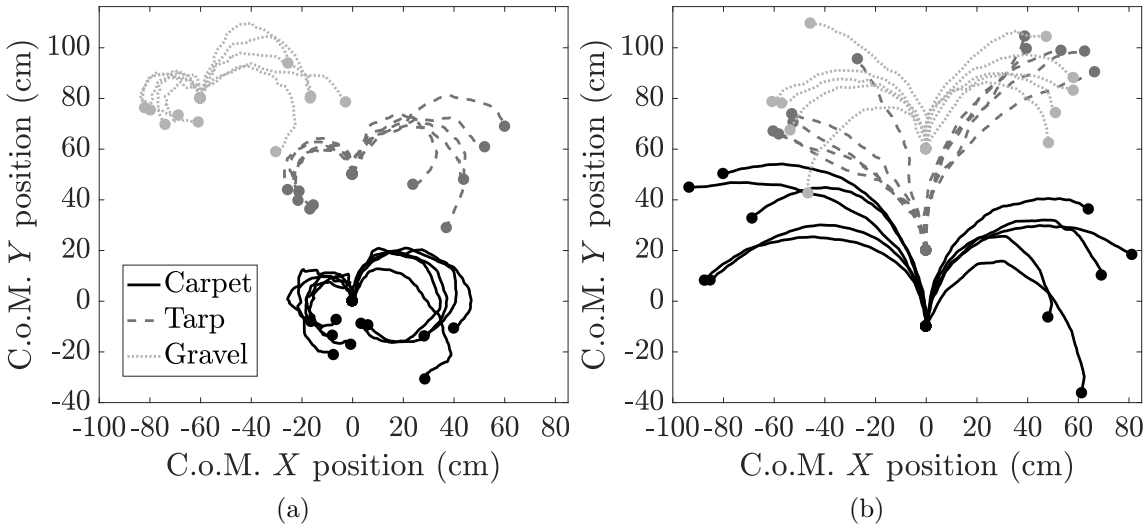


Figure 6.8: Experimental center of mass trajectories (measured from motion tracking) for sustained turns with the highest average maneuverability. Individual trials on different surfaces are shown for (a) differential drive and (b) tail drag turning methods.

Table 6.2: Maximum sustained turning maneuverability

Γ (deg m/s^2)	Carpet	Tarp	Gravel
Differential drive	$(-60, 35)$	$(-33, 27)$	$(-29, 24)$
Tail drag	$(-39, 36)$	$(-13, 11)$	$(-26, 26)$

and gravel surfaces, tail drag and differential drive turns have similar maneuverability, with the exception of clockwise differential drive producing turns with almost 50% higher maneuverability than clockwise tail drag. This asymmetric turning behavior can be explained by construction differences in the left and right sides of the robot's legs and transmission. Tail drag turning on tarp produces far less maneuverable turns than differential drive, which is due to the tail's limited friction (measured C.o.F. of 0.35 compared to the measured value of 0.7 on carpet) producing smaller yaw moments.

While the differential drive and tail drag turns have a similar value of Γ on carpet, they produce significantly different turns, as shown by the trajectories in Figure 6.8a and Figure 6.8b. Differential drive produces tighter turns with lower forward velocity, and tail drag produces lower curvature turns with higher forward velocity. These two different types of turning could be combined to enable the robot to select a strategy for different types of trajectory following tasks.

The tail impact turning performance is determined by the net yaw heading change $\Delta\psi$ that the turn produces and the elapsed time Δt for the robot to reach its nominal average forward running velocity after the start of the tail impact. These two quantities are plotted

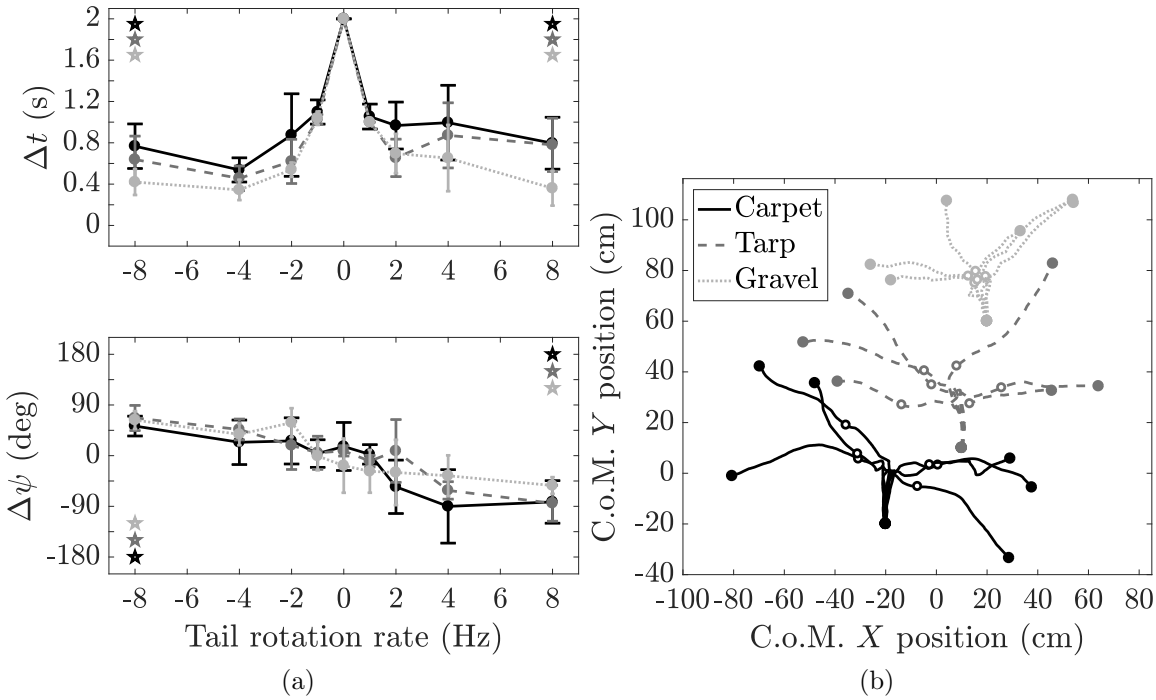


Figure 6.9: (a) Turn time Δt and turn angle $\Delta\psi$ over a single impact of the tail against the ground with varying tail rotation rate. The stars mark the highest performance turn with regard to average angular velocity over the turn event $\Delta\psi/\Delta t$. (b) Center of mass trajectories for select tail impact turn trials with the highest performance.

for varying tail rotation rate in Figure 6.9a. Overall, faster tail rotation rates produce faster average angular velocities $\Delta\psi/\Delta t$. Counterclockwise tail impacts produce clockwise turns and vice versa, which is consistent with the time series data in Figure 6.5. Figure 6.9b shows a selection of the fastest clockwise and counterclockwise tail impact turns (the filled white circles indicate the robot's C.o.M. position at which it reached its nominal average forward velocity after the tail impact). Note that some trajectories were omitted in this plot (but not from the net statistics in Figure 6.9a) because the robot did not turn in the intended direction. The achievable reorientation angles are similar across carpet, tarp, and gravel surfaces, and the robot takes a shorter average time to reorient on gravel, in which the robot is traveling at lower forward velocities. There is large variability in $\Delta\psi$ and Δt, because the magnitude of the rotation effect of the tail impact and the interaction of the legs with the ground depends heavily on the state of the robot at the instant of tail impact. In order to produce faster and more consistent turns with tail impacts, the tail motion needs to be more precisely coordinated with the leg and body motion of the robot (in these experiments, the instance of tail impact in the gait cycle is not strictly controlled).

Tail impact turning provides a rapid yaw reorientation capability with a smaller turn radius than differential drive or tail drag turning. The average and peak angular velocities

Table 6.3: Angular velocities achieved with tail impact turning

Yaw angular velocity (deg/s)	Carpet	Tarp	Gravel
Average—$\Delta\psi/\Delta t$	$(-106, 70)$	$(-113, 113)$	$(-164, 167)$
Peak—$\max \dot{\psi}(t)$	$(-589, 532)$	$(-624, 571)$	$(-600, 662)$

of the highest performance tail impact turns are shown in Table 6.3. The average angular velocities are computed with the mean values of $\Delta\psi$ and Δt for the starred experiment conditions in Figure 6.9a. The peak angular velocities are computed by taking the maximum of the instantaneous yaw angular velocity $\dot{\psi}(t)$ over the time interval of a full tail swing and then taking the mean across the trials for each surface. The peak angular velocity values for all surfaces exceed the reported maximum average turn rate of 400 deg/s for TAYLRoACH [82] turning on low-friction surfaces with an inertial tail. However, the achieved average angular velocity of LoadRoACH turning with a tail impact is significantly lower because LoadRoACH requires 0.4–0.8 s (4–8 strides) to recover from the transient disturbance to its alternating tripod running gait. The robot has the lowest tail impact turning velocities on carpet, which is likely due to the tendency of the legs to catch on the loops of the carpet under high loading. In addition, the robot achieves significantly faster average angular velocities $\Delta\psi/\Delta t$ on gravel. The average recovery times Δt are much shorter on gravel, which can be attributed to a combination of the slower forward speed of the robot on gravel and the tendency of the gravel to fluidize under high loading.

6.3.2 Closed-Loop Steering

The three turning methods characterized in the previous subsection were implemented with LoadRoACH to steer about a desired trajectory, with feedback on the robot's gyroscope state giving yaw heading ψ_{meas}. Differential drive steering (with the block diagram shown in Figure 6.10) applies proportional, integral, and derivative corrections based on the error ψ_{err} between the measured heading ψ_{meas} and the desired heading ψ_{ref}, with gains K_P, K_I, and K_D. An anti-windup term with gain K_{aw} prevents buildup of the integral term for cases in which there is a significant delay between applying the steering action and correcting the robot's heading. The correction terms sum to a differential leg frequency Δf, which is saturated to a value Δf_{sat} bounded by $\pm\Delta f_{max} = \pm 8$ Hz. Based on this differential leg frequency, the left and right leg frequencies f_L and f_R are set, which are inputs into the PID leg controller. If $\Delta f_{sat} < 0$, then $f_L = f_{nom}$ and $f_R = f_{nom} + \Delta f_{sat}$. If $\Delta f_{sat} \geq 0$, then $f_L = f_{nom} - \Delta f_{sat}$. In the following experiments f_{nom} is set to a value of 10 Hz.

Tail drag steering (with the block diagram shown in Figure 6.11) has the same controller structure as the differential drive steering controller. The controller adjusts the tail motion to steer the robot while running with a 10 Hz stride frequency alternating tripod gait. The correction terms sum to a differential switching time ΔT, which is saturated to a value ΔT_{sat} bounded by $\pm\Delta T_{max} = \pm 512$ ms. Based on this differential switching time, the tail

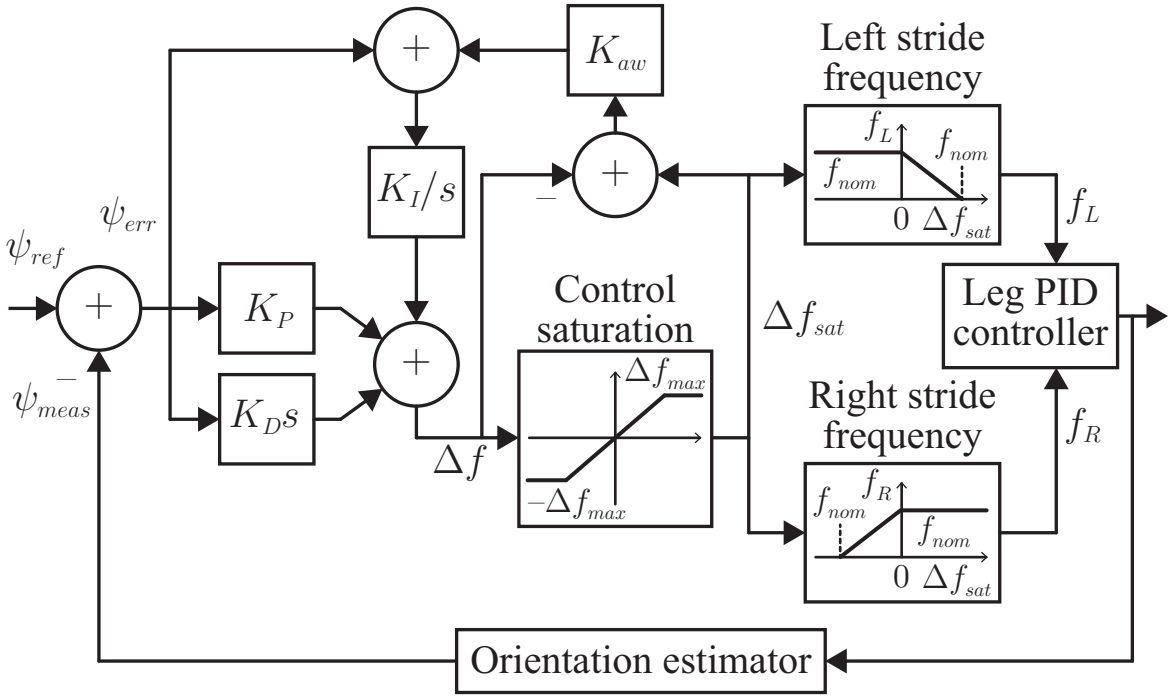


Figure 6.10: Closed-loop steering block diagram for differential drive leg control.

either swings counterclockwise or clockwise to apply a tail position input p_{in} that alternates between contacting the ground and lifting up off the ground. If $\Delta T_{sat} \geq 0$, then the tail switches between a dragging position of $p_{max} = 137°$ (corresponding to $\Delta\theta_t = 7°$) and a lifted off position of $p_{max} - \Delta p$, with $\Delta p = 20°$. If $\Delta T_{sat} < 0$, then the tail switches between a dragging position of $p_{min} = -132°$ (corresponding to $\Delta\theta_t = -7°$) and a lifted off position of $p_{min} + \Delta p$. The dragging time interval is $T_1 = T_{min} + |\Delta T_{sat}|$ and the lifted off time interval is $T_2 = T_{max} - |\Delta T_{sat}|$, with $T_{min} = 25$ ms and $T_{max} = 527$ ms. This controller causes the tail to drag for a longer time interval relative to the lift off interval as the control signal ΔT_{sat} increases in magnitude.

Tail impact steering (with the block diagram shown in Figure 6.12) is implemented with a simple bang-bang controller. If the yaw error is within a threshold $-\psi_{lim} \leq \psi_{err} \leq \psi_{lim}$ then the tail remains stationary, with $\psi_{lim} = 70°$. If $\psi_{err} > \psi_{lim}$, then the tail is controlled to impact the ground with input velocity $v_{in} = -v_{imp}$. If $\psi_{err} < \psi_{lim}$, then $v_{in} = v_{imp}$. In the following experiments, the impact velocity v_{imp} is set to a value of 4 Hz. The tail impact steering controller is intended to rapidly correct large errors in heading. The bang-bang tail impact steering control is combined with the continuously varying differential drive and tail drag steering controllers in the following closed-loop experiments. The robot switches its tail control to a constant velocity if ψ_{err} falls outside the bounds $\pm\psi_{lim}$.

In an aggressive closed-loop steering maneuver, LoadRoACH is commanded to go straight

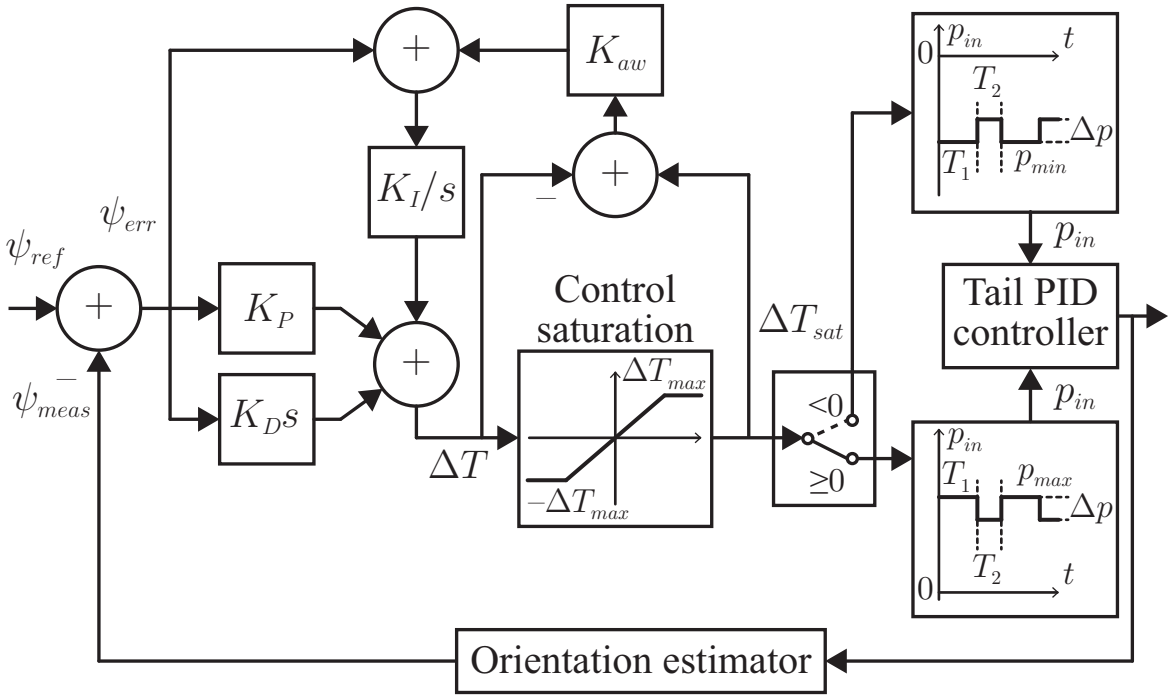


Figure 6.11: Closed-loop steering block diagram for tail drag control.

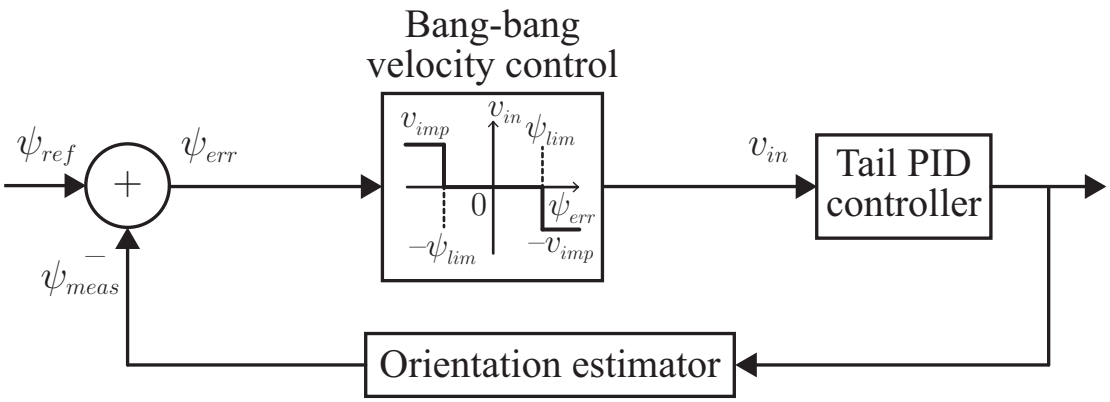


Figure 6.12: Closed-loop steering block diagram for tail impact control.

for 2.25 seconds, then turn counterclockwise 90° after 2.5 seconds, then turn clockwise 90° and continue running for 2.25 seconds. This is an aggressive maneuver because the robot is making rapid corner transitions in heading while its legs are driving it forward at maximum velocity. Note that the robot is not using information from the motion tracking system to follow absolute position trajectories. Figure 6.13 compares three steering strategies—

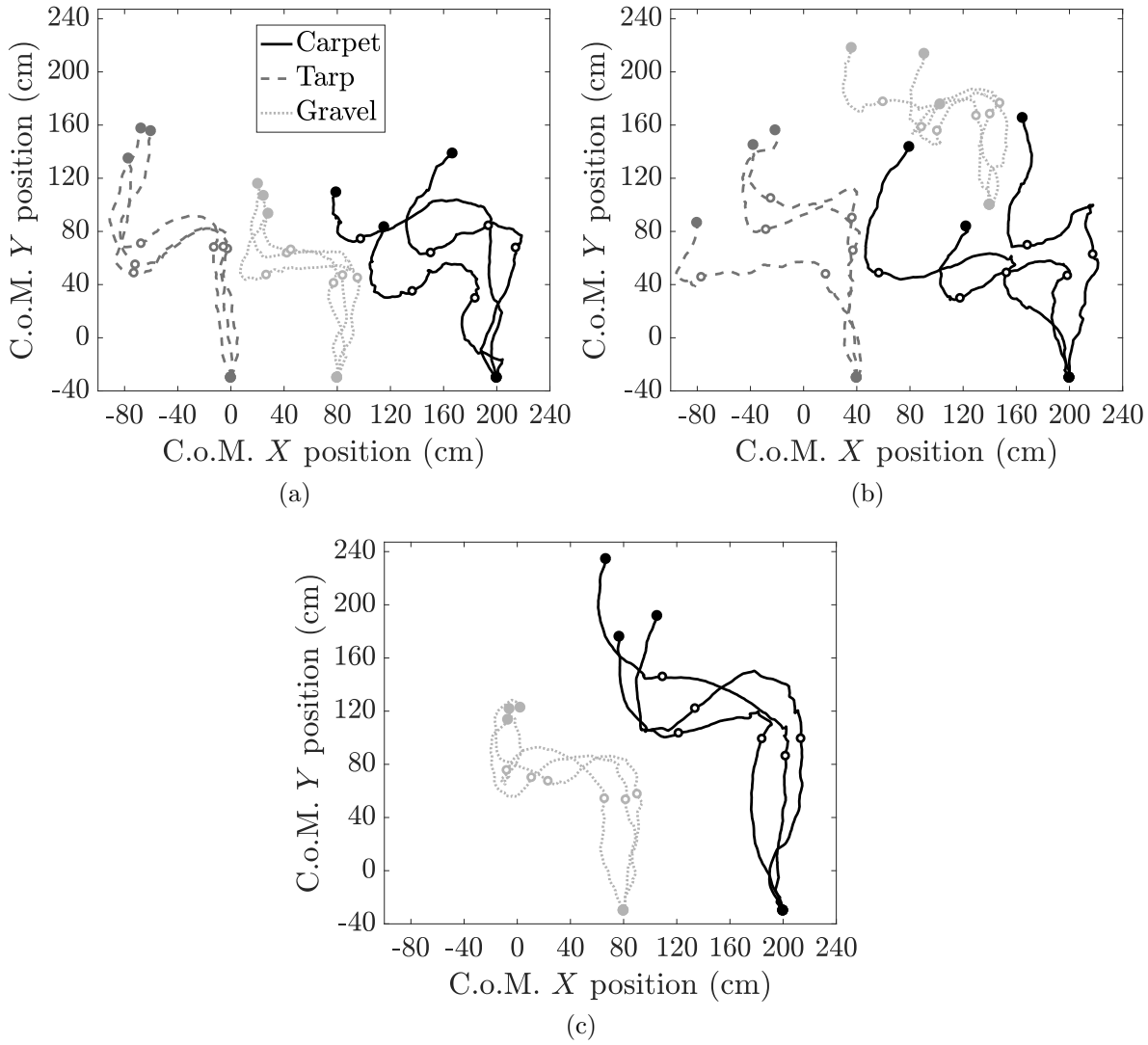


Figure 6.13: Closed-loop corner turn steering trajectories using gyroscope feedback. The reference yaw trajectory is 0 degrees from the start, then 90 degrees counterclockwise, then 0 degrees until the end. The filled white circles indicate a step change in reference heading. (a) Differential drive, (b) differential drive with tail impact switching, and (c) tail drag with tail impact switching steering methods.

differential drive, differential drive with tail impact past an angular error threshold, and tail drag turning with tail impact. The steering performance during the aggressive corner turn maneuver for each closed-loop strategy is shown in Figure 6.14. The two metrics are the root mean square yaw error in tracking the trajectory and the average velocity of the robot along the desired direction over the course of steering. All test conditions produced large RMS yaw errors ranging from 30° to 45°. The one noticeable improvement in steering

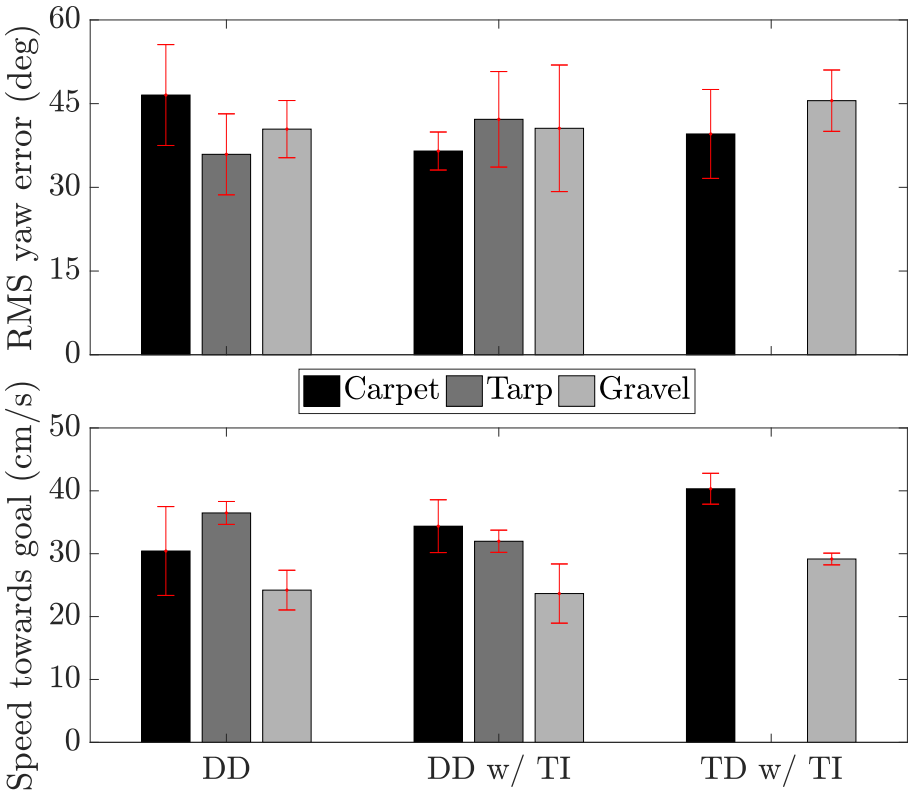


Figure 6.14: Closed-loop steering performance for an aggressive corner turn maneuver. The mean and standard deviation of 3 trials are shown for each condition. Differential drive (DD), differential drive with tail impact (DD w/ TI), and tail drag with tail impact (TD w/ TI) control strategies are compared for carpet, tarp, and gravel surfaces.

is that the tail drag with tail impact control strategy implemented on carpet produces a 30% higher speed towards goal (40 cm/s) compared to differential drive (30 cm/s). As seen in the trajectory plots in Figure 6.13, differential drive produces large over-steering swings on carpet, which can be explained the continuously varying phasing of the legs as the robot changes leg velocity. Because the robot is not strictly following a periodic gait during differential drive steering, there are more instances of leg stubbing against the carpet that can cause the robot to fail to turn in the desired direction even though its legs are attempting to turn. In contrast, tail drag turning produces more gradual heading adjustments during straight segments, while tail impacts rapidly change heading during the corner transitions.

Chapter 7

Conclusions

7.1 Discussion

In conclusion, this dissertation contributes physical analysis and experimental validation of added components and tailed maneuvers that improve the mobility and robustness of folded legged millirobots in challenging environments. The contributions include a protective shell manufacturing process, a high-payload folded legged millirobot design, insights into terrestrial self-righting with a minimal tail, and the development of two novel tailed turning strategies that enhance legged maneuverability.

The developed shell manufacturing process leverages laser cutting and 3D printing processes with inexpensive materials to create molds for structural and flexible shell layers. Through the use of multi-layer molds and heat sealing, snap-fit interlocks and polyethylene zippers can be integrated into the structural and flexible shells, respectively. These design features add little cost and complexity to the molds, and enable easy, reversible assembly of the fabricated exoskeleton around the chassis of a folded legged millirobot, which is ideal for both laboratory experimentation and deployment in the field. The stiffness of the polycarbonate structural shell can be tuned to absorb impact energy. With the structural shell, a VelociRoACH robot can withstand collisions from a four story drop. The polyethylene flexible shell provides full protection of the robot from granular particles as small as poppy seeds, which could potentially jam the gears or mechanisms. The flexible shell also provides partial protection against water. The electronics and SCM mechanisms of the robot survived 3 min of running through shallow water, although some water was admitted into the resealable flexible shell. The shell manufacturing process can be scaled to produce lightweight protective exoskeletons for robot platforms of different morphologies and size scales.

LoadRoACH, the novel robot platform developed in this dissertation, is a 54.8 g folded legged millirobot that can dynamically run while carrying significantly larger payloads (totaling 27.2 g) than prior folded robots of comparable size scale. In the scaled Smart Composite Microstructures manufacturing process used to fabricate the folded chassis of LoadRoACH, PET plastic replaces cardboard structures, PET flexures are strengthened with ripstop ny-

lon, and the layers of the composite are bonded with increased temperature and pressure. These process changes to SCM manufacturing improve the delamination strength and load transmission of folded mechanisms, which enable them to support higher payloads than the mechanisms of previous palm-sized folded robots. In addition, a novel transmission module with two synchronized crank outputs driving each leg side eliminate the SCM planarizing four-bar linkage of previous designs, providing more robust load transmission from the motor to the legs of the robot. At a stride frequency of 10 Hz, LoadROACH can run as fast as VelociRoACH (the prior state of the art folded robot platform) running at the same frequency, while carrying shell and tail payloads that provide tailed self-righting and turning mobility.

For tailed self-righting with terrain contact, the analysis gives quasi-static torque requirements for sizing a tail and a tail motor for self-righting a ground robot. The dynamic simulation of tailed self-righting on flat terrain gives a reasonable prediction for the time required to self-right on uniform surfaces. Compared to aerial self-righting with an inertial tail of the same length and end mass ranging from 2.6% to 10.3% robot mass, terrestrial self-righting on wood (simulation righting time of 235 ms) is predicted to be 12–89 ms slower, while in experiments the robot took an additional 39 ms to self-right. An advantage of this self-righting strategy is that it can be performed with a tail that is only 1% of the robot's mass. Experiments using a 77.5 g tailed VelociRoACH robot show that tailed terrestrial self-righting can be consistently achieved with righting times as fast as 256 ms (with at least an 80% success rate after a single open-loop tail swing). This self-righting method is fast and repeatable on flat surfaces of varying friction and moderately rough rock terrain, and the tested robot performs a 180° roll reorientation on carpet faster than other platforms that use inertial tails or tail contact to reorient about pitch, roll, or yaw axes. The demonstration of the autonomous tailed self-righting reflex shows that VelociRoACH with tail is capable of detecting and recovering from inversion as it moves on terrain with step drops on the order of the robot's body length.

The two novel turning strategies developed in this dissertation leverage the contact of an active tail against terrain to enhance the maneuverability of underactuated legged robots. In an analysis of the steady-state turns that can be sustained by a dragging tail, a bound on the forward and angular velocity of tail drag turning on carpet was determined and experimentally validated. In open-loop turning experiments using LoadRoACH, the tail drag turning method exhibited comparable turning maneuverability relative to the baseline of differential drive on carpet and gravel surfaces, and was not able to produce significant turns on a tarp surface with low friction. Tail impact turning can produce rapid point turns on carpet, tarp, and gravel with a heading change of up to 90° in 0.8 s, but has a large variability in turn angle and time to recover from the transient tail disturbance. In a closed-loop steering test of the robot tracking an aggressive corner turn, tail contact turning demonstrated an improvement in steering performance on carpet compared to differential drive. By combining tail drag modulated steering with transient tail impacts to correct large heading errors, the robot was able to complete the corner turn maneuver while progressing faster towards the instantaneous goal heading.

7.2 Future Directions

7.2.1 Shell Manufacturing

In the developed shell manufacturing process, thermoforming is easily scalable to form large batches of shells in parallel, but the processing of the formed plastic sheets to create the final shells could be further streamlined. Currently, a laser cutter makes cutouts in structural shells, but cannot cut sections with significant curvature. Also, the heat-sealing of the flexible shell layers is currently performed by hand. Specialized jigs and tooling with cutting edges or heated elements could be developed to lower onto a sheet of formed shells, making all required shell cuts and heat welds. Furthermore, design software could be developed to automatically generate structural shells with sufficient clearance for moving parts and flexible shells that attach to a robot with minimal restriction to mechanisms, while considering the effectiveness and manufacturability of different shell geometries based on the structural properties, thermoforming properties, and thickness of available materials. This automated design software would enable easy adaptation of the shell manufacturing process to robot platforms of different scales and morphologies, including robots with different drive mechanisms and appendage counts.

7.2.2 Tailed Self-Righting with Terrain Contact

The roll-plane dynamic simulation of tailed self-righting with terrain contact was unable to fully model the conditions of the experiments. In future work, the simulation could be improved through a 3D dynamics formulation that accounts for the pitch and yaw body motions that the tail causes. In addition, a terradynamics model such as resistive force theory by Li et al. [92] could be included to better model self-righting on granular terrain, which would help develop more robust tail control strategies on dirt, sand, and gravel. Self-righting through tail contact was demonstrated on flat terrain, but large obstacles compared to the robot could prevent successful self-righting, such as channels that are too narrow for the body to fully rotate and ledges that cause the tail to lose contact with the ground. Planned vibrational or contacting leg motions coordinated with tail motion would potentially self-right the robot from these challenging conditions.

In the autonomous self-righting reflex experiments, switching to a prescribed righting strategy during inversion produced self-righting that was no faster than open-loop self-righting. In a continuation of this work, a control strategy could be developed to position the tail and produce torque in response to a measured disturbance, which would prevent inversion while running on rough terrain with varying slope. This feedback control strategy would exert a control effort that scales with disturbance magnitude and would make decisions such as rolling downhill instead of uphill to speed up righting.

7.2.3 Tailed Turning with Terrain Contact

The tail drag equilibrium analysis could be applied in a sensitivity study to determine the space of possible turns with different tail geometries, robot drive capabilities, and environment friction conditions. In addition, tail impact control strategies other than following a fixed velocity trajectory could be explored. More consistent tail impact turning effects could be achieved by modulating the tail effort according to feedback controllers that consider the estimated torque exerted by the tail and the measured state information from the robot's IMU. The closed-loop steering capabilities of the developed tail contact turning methods combined with various legged gaits could be further characterized in gradual to aggressive turning trajectories. A more systematic study of closed-loop steering control with a combination of differential drive gaits and tail drag or tail impact turning could reveal gait sequences and control strategies that are tailored for sustained turning, rapid obstacle avoidance, or straight-line steering tasks, while providing minimal disturbance to the robot's forward velocity along desired trajectories.

Outside of the framework of differential drive, tail drag, and tail impact turning methods, there may exist a larger class of periodic gaits involving coordinated leg and tail contact sequences that result in more rapid turning, significant jumps to overcome obstacles, or pitching behavior that aids in transitions between surfaces of different inclinations. Machine learning driven experimental exploration of periodic gaits with intermittent tail pushing could rapidly accelerate the discovery of control methods for novel dynamic maneuvers.

Based on the results of the tailed turning experiments, using a single leg motor to drive an alternating tripod gait and a single tail motor to contact terrain can achieve similar turning maneuverability compared to a robot with two leg drive motors on each side. This finding provides justification for designing a robot that dedicates a single high-power motor to legged running while using a tail to turn.

7.2.4 Deploying LoadRoACH in Search and Rescue Applications

This dissertation presented the novel high-payload folded legged robot design LoadRoACH, which has the potential to provide distributed sensing with enhanced mobility in a variety of applications. These applications include the inspection of bridges and buildings for structural damage, the monitoring of natural environments with diverse terrain such as grass, branches, mud, loose rocks, and streams, and the detection of explosives in advance of a group of soldiers. A particularly suitable application for LoadRoACH is searching for survivors in a collapsed building after an earthquake, which is a challenging environment featuring loose rubble, terrain with steep drop-offs, and low-clearance voids. A grand challenge to address over the next decade is deploying many LoadRoACH robots as part of an intelligent, heterogeneous team of robots and humans working together to save lives in a collapsed building disaster site.

To deploy many LoadRoACH robots in a search and rescue scenario, the overall capability of the team of robots needs to be optimized. In addition to the shell and tail pay-

loads carried by LoadRoACH for the experiments in this dissertation, this robot platform could carry payloads such as higher capacity batteries, processors with increased computing power, additional sensors, and additional actuators. Potentially useful sensor payloads include cameras or range sensors to detect obstacles and map the environment, chemical sensors or microphones to localize survivors, and force sensors to control locomotion through rubble. Potentially useful actuator payloads include motors that add degrees of freedom or power to leg and tail motions, driven connections between robots for cooperative adaptation to rough terrain, and mechanisms that rapidly release energy to jump. After enumerating the potential payloads, simulation and experimental studies could be used to select a combination of payloads that optimize the performance of a group of deployed robots, with potential performance metrics including operation time, mobility over terrain of varying difficulty, and useful sensory information collected. These findings would need to be validated in a recreated collapsed building site.

Ultimately, an approach using LoadRoACH for search and rescue would involve developing a planning, communication, and control framework for the agents in a distributed heterogeneous team. This team may include 100 LoadRoACH robots moving through rubble and creating crude maps, 1–10 larger legged robots and rotorcraft with higher fidelity cameras and laser range finders mapping the outside of the collapsed building, and 10–20 human first responders monitoring the information gathered by the robots, selecting potential ingress points, moving rubble, and rescuing survivors.

Appendix A

LoadRoACH Transmission Details

This appendix provides details of the custom fabricated and commercial off the shelf components used for the LoadRoACH transmission module presented in Subsection 4.2.3. Table A.1 shows the component number, name, description, vendor, catalog number, and quantity of each component used to build the transmission. Daggers indicate that a component is custom fabricated, and in these cases the vendor and catalog number are given for the material used to make the part. Figure A.1 shows an engineering drawing of the LoadRoACH transmission module, with annotations corresponding to the component numbers in Table A.1.

Table A.1: Bill of materials for LoadRoACH transmission module

#	Name	Description	Vendor	Catalog #	Quantity
1	Pager motor	6 mm diameter 3.6 Ω pager motor	DASH Robotics	N/A	2
2	Pinion gear	9T, 0.3 mm module	Solarbotics	51602	2
3	Compound gear†	Cast urethane 12T/48T, 0.3 mm module	Innovative Polymers	IE-3075	4
4	Gear pin	Stainless steel 1 mm diameter	McMaster	91585A093	4
5	Gear spacer†	Laser cut acrylic	McMaster	8589K31	4
6	Output gear†	Cast urethane 48T with shaft key	Innovative Polymers	IE-3075	4
7	Output shaft†	Form 2 3D printed grey material	Formlabs	RS-F2-GPGR-04	4
8	Output plate bearing	R144-2RS bearing	Amazon	B00NKS74SU	4
9	Output spacer†	Laser cut acrylic	McMaster	8589K31	4
10	Output crank†	Cast urethane	Innovative Polymers	IE-3075	4
11	Output hex nut	Stainless steel 2-56 thread	McMaster	90730A003	4
12	Output shoulder screw	Stainless steel 2-56 thread	McMaster	94035A112	4
13	Output shim†	Laser cut Delrin	McMaster	8738K61	4
14	Output coupler bearing	R133-2Z flange bearing	McMaster	57155K327	4
15	Output coupler†	Cast urethane	Innovative Polymers	IE-3075	4
16	Outer plate†	Cast urethane	Innovative Polymers	IE-3075	2
17	Clamp bolt	Nylon 2-56 thread	McMaster	93135A019	2
18	Plate spacer	Nylon	McMaster	94639A464	4
19	Clamp nut	Nylon 2-56 thread	McMaster	94812A100	2
20	Encoder plate†	Cast urethane	Innovative Polymers	IE-3075	1
21	Encoder pin	Alloy steel 1.5 mm diameter	McMaster	91595A002	4
22	Encoder IC	AMS rotary encoder	Digikey	AS5048B-HTSP-500CT-ND	2
23	Encoder magnet	Diametrically polarized	SuperMag-netMan	D1021D	2

† Custom fabricated in the Biomimetic Millisystems Laboratory

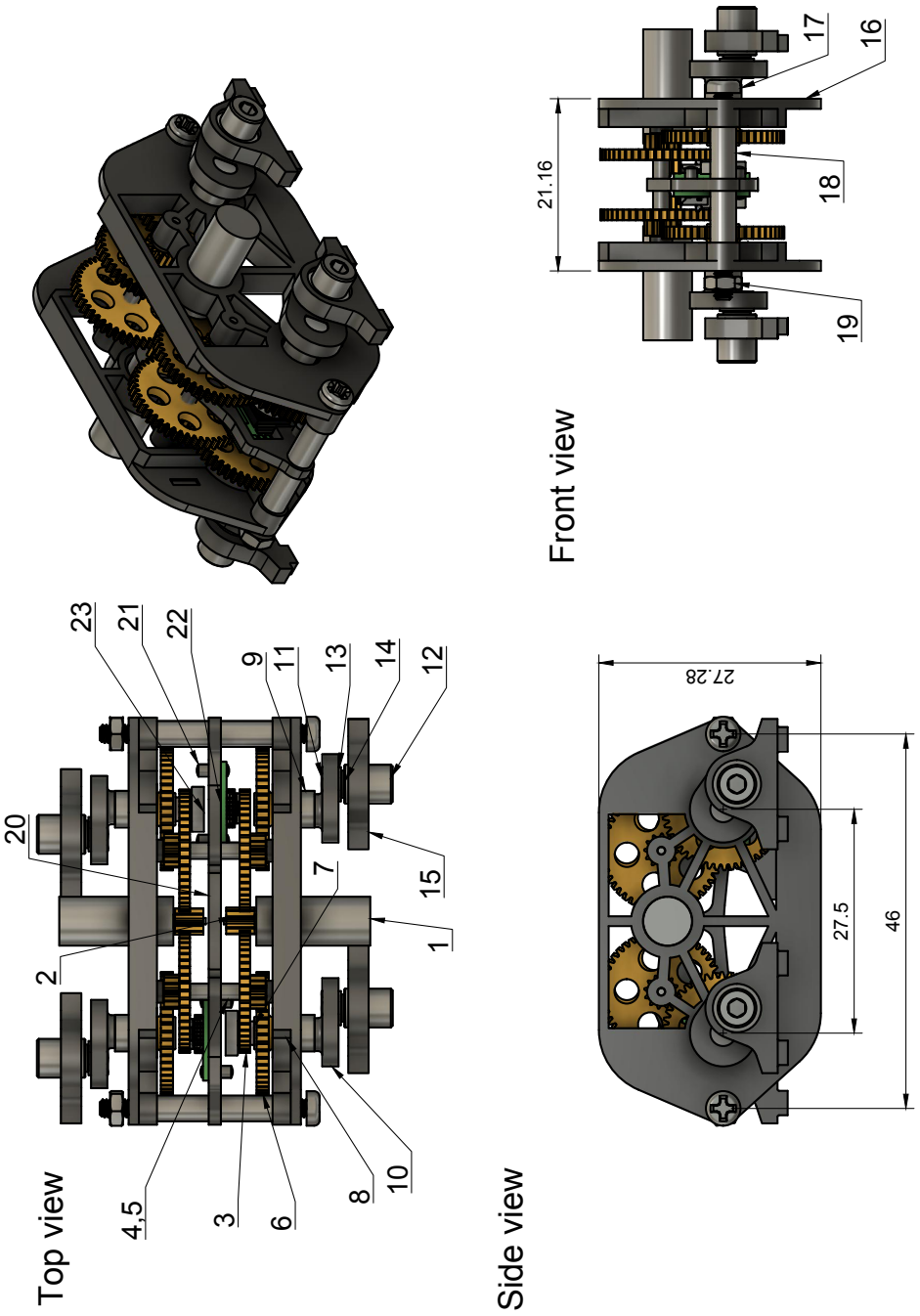


Figure A.1: Engineering drawing of the LoadRoACH transmission module with annotations of components from the bill of materials. Dimension units are millimeters.

Bibliography

[1] Shinya Aoi, Takahiro Tanaka, Soichiro Fujiki, Tetsuro Funato, Kei Senda, and Kazuo Tsuchiya. "Advantage of straight walk instability in turning maneuver of multilegged locomotion: A robotics approach". In: *Sci. Rep.* 6 (2016), p. 30199. DOI: 10.1038/srep30199.

[2] Rhodri Armour, Keith Paskins, Adrian Bowyer, Julian Vincent, and William Megill. "Jumping robots: A biomimetic solution to locomotion across rough terrain". In: *Bioinspir. Biomim.* 2.3 (2007), S65. DOI: 10.1088/1748-3182/2/3/S01.

[3] Stanley S. Baek, Fernando L. Garcia Bermudez, and Ronald S. Fearing. "Flight control for target seeking by 13 gram ornithopter". In: *IEEE/RSJ Int. Conf. on Intelligent Robots and Systems*. 2011, pp. 2674–2681. DOI: 10.1109/IROS.2011.6094581.

[4] Andrew T. Baisch, Christian Heimlich, Michael Karpelson, and Robert J. Wood. "HAMR3: An autonomous 1.7 g ambulatory robot". In: *IEEE/RSJ Int. Conf. on Intelligent Robots and Systems*. 2011, pp. 5073–5079. DOI: 10.1109/IROS.2011.6095063.

[5] Andrew T. Baisch, Onur Ozcan, Benjamin Goldberg, Daniel Ithier, and Robert J. Wood. "High speed locomotion for a quadrupedal microrobot". In: *Int. J. Robot. Res.* 33.8 (2014), pp. 1063–1082. DOI: 10.1177/0278364914521473.

[6] Eric Beyer and Mark Costello. "Performance of a hopping rotochute". In: *International Journal of Micro Air Vehicles* 1.2 (2009), pp. 121–137. DOI: 10.1260/175682909789498242.

[7] Paul Birkmeyer, Andrew G. Gillies, and Ronald S. Fearing. "CLASH: Climbing vertical loose cloth". In: *IEEE/RSJ Int. Conf. on Intelligent Robots and Systems*. 2011, pp. 5087–5093. DOI: 10.1109/IROS.2011.6094905.

[8] Paul Birkmeyer, Andrew G. Gillies, and Ronald S. Fearing. "Dynamic climbing of near-vertical smooth surfaces". In: *IEEE/RSJ Int. Conf. on Intelligent Robots and Systems*. 2012, pp. 286–292. DOI: 10.1109/IROS.2012.6385775.

[9] Paul Birkmeyer, Kevin Peterson, and Ronald S. Fearing. "DASH: A dynamic 16g hexapedal robot". In: *IEEE/RSJ Int. Conf. on Intelligent Robots and Systems*. 2009, pp. 2683–2689. DOI: 10.1109/IROS.2009.5354561.

[10] Reinhard Blickhan and Robert J. Full. "Similarity in multilegged locomotion: Bouncing like a monopode". In: *J. Comp. Physiol. A* 173.5 (1993), pp. 509–517. DOI: 10.1007/BF00197760.

[11] Randall Briggs, Jongwoo Lee, Matt Haberland, and Sangbae Kim. "Tails in biomimetic design: Analysis, simulation, and experiment". In: *IEEE/RSJ Int. Conf. on Intelligent Robots and Systems*. 2012, pp. 1473–1480. DOI: 10.1109/IROS.2012.6386240.

[12] Anna L. Brill, Avik De, Aaron M. Johnson, and Daniel E. Koditschek. "Tail-assisted rigid and compliant legged leaping". In: *IEEE/RSJ Int. Conf. on Intelligent Robots and Systems*. 2015, pp. 6304–6311. DOI: 10.1109/IROS.2015.7354277.

[13] Adrien Briod, Przemyslaw Kornatowski, Jean-Christophe Zufferey, and Dario Floreano. "A collision-resilient flying robot". In: *J. Field Robot.* 31.4 (2014), pp. 496–509. DOI: 10.1002/rob.21495.

[14] Martin Buehler, R. Battaglia, A. Cocosco, Geoff Hawker, J. Sarkis, and K. Yamazaki. "SCOUT: A simple quadruped that walks, climbs, and runs". In: *IEEE Int. Conf. on Robotics and Automation*. Vol. 2. 1998, pp. 1707–1712. DOI: 10.1109/ROBOT.1998.677408.

[15] Joel Burdick and Paolo Fiorini. "Minimalist jumping robots for celestial exploration". In: *Int. J. Robot. Res.* 22.7–8 (2003), pp. 653–674. DOI: 10.1177/02783649030227013.

[16] Jeffrey M. Camhi and Aharon Levy. "Organization of a complex movement: Fixed and variable components of the cockroach escape behavior". In: *J. Comp. Physiol. A* 163.3 (1988), pp. 317–328. DOI: 10.1007/BF00604007.

[17] Carlos S. Casarez and Ronald S. Fearing. "Dynamic terrestrial self-righting with a minimal tail". In: *IEEE/RSJ Int. Conf. on Intelligent Robots and Systems*. 2017, pp. 314–321. DOI: 10.1109/IROS.2017.8202174.

[18] Carlos S. Casarez and Ronald S. Fearing. "Steering of an underactuated legged robot through terrain contact with an active tail". In: *IEEE/RSJ Int. Conf. on Intelligent Robots and Systems (accepted)*. Oct. 2018.

[19] Carlos S. Casarez and Ronald S. Fearing. "Step climbing cooperation primitives for legged robots with a reversible connection". In: *IEEE Int. Conf. on Robotics and Automation*. 2016, pp. 3791–3798. DOI: 10.1109/ICRA.2016.7487567.

[20] Jorge G. Cham, Sean A. Bailey, Jonathan E. Clark, Robert J. Full, and Mark R. Cutkosky. "Fast and robust: Hexapedal robots via shape deposition manufacturing". In: *International Journal of Robotics Research* 21.10-11 (2002), pp. 869–882. DOI: 10.1177/027836490202101083 7.

[21] Evan Chang-Siu, Thomas Libby, Matthew Brown, Robert J. Full, and Masayoshi Tomizuka. "A nonlinear feedback controller for aerial self-righting by a tailed robot". In: *IEEE Int. Conf. on Robotics and Automation*. 2013, pp. 32–39. DOI: 10.1109/ICRA.2013.6630553.

[22] Evan Chang-Siu, Thomas Libby, Masayoshi Tomizuka, and Robert J. Full. "A lizard-inspired active tail enables rapid maneuvers and dynamic stabilization in a terrestrial robot". In: *IEEE/RSJ Int. Conf. on Intelligent Robots and Systems*. 2011, pp. 1887–1894. DOI: 10.1109/IROS.2011.6094658.

[23] Teeranoot Chanthasopeephan, Arnas Jarakorn, Pongsakorn Polchankajorn, and Thavida Maneewarn. "Impact reduction mobile robot and the design of the compliant legs". In: *Robot. Auton. Syst.* 62.1 (2014), pp. 38–45. DOI: 10.1016/j.robot.2012.07.017.

[24] Kewei Chen, Diansheng Chen, Ziqiang Zhang, and Min Wang. "Jumping robot with initial body posture adjustment and a self-righting mechanism". In: *Int. J. Adv. Robot. Syst.* 13.3 (2016), p. 127. DOI: 10.5772/64200.

[25] Holk Cruse and Manuel G. Silva Saavedra. "Curve walking in crayfish". In: *J. Exp. Biol.* 199.7 (1996), pp. 1477–1482. URL: http://jeb.biologists.org/content/jexbio/199/7/1477.full.pdf.

[26] Jonas Degrave, Michaël Burm, Tim Waegeman, Francis Wyffels, and B. Schrauwen. "Comparing trotting and turning strategies on the quadrupedal oncilla robot". In: *IEEE Int. Conf. on Robotics and Biomimetics*. 2013, pp. 228–233. DOI: 10.1109/ROBIO.2013.6739463.

[27] Alican Demir, Mustafa Mert Ankarali, Jonathan P. Dyhr, Kristi A. Morgansen, Thomas L. Daniel, and Noah J. Cowan. "Inertial redirection of thrust forces for flight stabilization". In: *International Conference on Climbing and Walking Robots*. World Scientific, 2012, pp. 239–245. URL: https://limbs.lcsr.jhu.edu/wp-content/uploads/2013/05/Demirinertial2012.pdf.

[28] Gábor Domokos and Péter L. Várkonyi. "Geometry and self-righting of turtles". In: *Proceedings of the Royal Society of London B: Biological Sciences* 275.1630 (2008), pp. 11–17. DOI: 10.1098/rspb.2007.1188.

[29] Jonathan P. Dyhr, Kristi A. Morgansen, Thomas L. Daniel, and Noah J. Cowan. "Flexible strategies for flight control: An active role for the abdomen". In: *J. Exp. Biol.* 216.9 (2013), pp. 1523–1536. DOI: 10.1242/jeb.077644.

[30] A. A. Faisal and T. Matheson. "Coordinated righting behaviour in locusts". In: *J. Exp. Biol.* 204.4 (2001), pp. 637–648. URL: http://jeb.biologists.org/content/jexbio/204/4/637.full.pdf.

[31] Ian Fitzner, Yue Sun, Vikram Sachdeva, and Shai Revzen. "Rapidly prototyping robots: Using plates and reinforced flexures". In: *IEEE Robotics & Automation Magazine* 24.1 (2017), pp. 41–47. DOI: 10.1109/MRA.2016.2639058.

[32] Leonid Frantsevich. "Righting kinematics in beetles (Insecta: Coleoptera)". In: *Arthropod Struct. Dev.* 33.3 (2004), pp. 221–235. DOI: 10.1016/j.asd.2004.05.007.

[33] Amitabha Ghosh. "Scaling laws". In: *Mechanics Over Micro and Nano Scales*. Ed. by Suman Chakraborty. Springer, 2011. DOI: 10.1007/978-1-4419-9601-5.

[34] Benjamin Goldberg, Raphael Zufferey, Neel Doshi, Elizabeth Farrell Helbling, Griffin Whittredge, Mirko Kovac, and Robert J. Wood. "Power and control autonomy for high speed locomotion with an insect-scale legged robot". In: *IEEE Robot. Autom. Lett.* 3.2 (2018), pp. 987–993. DOI: 10.1109/LRA.2018.2793355.

[35] Joshua D. Goldberg and Ronald S. Fearing. "Force sensing shell using a planar sensor for miniature legged robots". In: *IEEE/RSJ Int. Conf. on Intelligent Robots and Systems*. 2015, pp. 1494–1500. DOI: 10.1109/IROS.2015.7353565.

[36] D. Graham. "A behavioural analysis of the temporal organisation of walking movements in the 1st instar and adult stick insect (Carausius morosus)". In: *J. Comp. Physiol.* 81.1 (1972), pp. 23–52. DOI: 10.1007/BF00693548.

[37] Zong Guanghua, Deng Zhicheng, and Wang Wei. "Realization of a modular reconfigurable robot for rough terrain". In: *IEEE Int. Conf. on Mechatronics and Automation*. 2006, pp. 289–294. DOI: 10.1109/ICMA.2006.257529.

[38] Michele Guarnieri, Paulo Debenest, Takao Inoh, Kensuke Takita, Hiroshi Masuda, Ryo Kurazume, Edwardo Fukushima, and Shigeo Hirose. "HELIOS carrier: Tail-like mechanism and control algorithm for stable motion in unknown environments". In: *IEEE Int. Conf. on Robotics and Automation*. 2009, pp. 1851–1856. DOI: 10.1109/ROBOT.2009.5152513.

[39] Axel Hackbarth, Edwin Kreuzer, and Eugen Solowjow. "HippoCampus: A micro underwater vehicle for swarm applications". In: *IEEE/RSJ Int. Conf. on Intelligent Robots and Systems*. 2015, pp. 2258–2263. DOI: 10.1109/IROS.2015.7353680.

[40] Duncan W. Haldane, Carlos S. Casarez, Jaakko T. Karras, Jessica Lee, Chen Li, Andrew O. Pullin, Ethan W. Schaler, Dongwon Yun, Hiroki Ota, Ali Javey, and Ronald S. Fearing. "Integrated manufacture of exoskeletons and sensing structures for folded millirobots". In: *J. Mech. Robot.* 7.2 (2015), p. 021011. DOI: 10.1115/1.4029495.

[41] Duncan W. Haldane and Ronald S. Fearing. "Roll oscillation modulated turning in dynamic millirobots". In: *IEEE Int. Conf. on Robotics and Automation*. 2014, pp. 4569–4575. DOI: 10.1109/ICRA.2014.6907526.

[42] Duncan W. Haldane and Ronald S. Fearing. "Running beyond the bio-inspired regime". In: *IEEE Int. Conf. on Robotics and Automation*. 2015, pp. 4539–4546. DOI: 10.1109/ICRA.2015.7139828.

[43] Duncan W. Haldane, Kevin C. Peterson, Fernando L. Garcia Bermudez, and Ronald S. Fearing. "Animal-inspired design and aerodynamic stabilization of a hexapedal millirobot". In: *IEEE Int. Conf. on Robotics and Automation*. 2013, pp. 3279–3286. DOI: 10.1109/ICRA.2013.6631034.

[44] Duncan W. Haldane, Mark M. Plecnik, Justin K. Yim, and Ronald S. Fearing. "Robotic vertical jumping agility via series-elastic power modulation". In: *Science Robotics* 1.1 (2016). DOI: 10.1126/scirobotics.aag2048.

[45] Hideki Hayashi, Toshiyuki Kondo, and Koji Ito. "Development of a hexapod robot focusing on leg compliance". In: *Proc. of the 2nd Int. Symposium on Adaptive Motion of Animals and Machines*. 2003, pp. 4–8. URL: http://adaptivemotion.org/AMAM2003/PAPERS/E31-hayashi.pdf.

[46] Brett Hemes and Nikolaos Papanikolopoulos. "Frictional step climbing analysis of tumbling locomotion". In: *IEEE International Conference on Robotics and Automation*. 2012, pp. 4142–4147. DOI: 10.1109/ICRA.2012.6224644.

[47] Bernhard Hengst, Darren Ibbotson, Son Bao Pham, and Claude Sammut. "Omnidirectional locomotion for quadruped robots". In: *RoboCup 2001: Robot Soccer World Cup V*. Lecture Notes in Computer Science. Springer. 2002, pp. 368–373. DOI: 10.1007/3-540-45603-1_45.

[48] Frank Hild. *Surface Energy of Plastics*. 2009. URL: https://www.tstar.com/blog/bid/33845/surface-energy-of-plastics (visited on 08/01/2018).

[49] Koichi Hirata. "Development of experimental fish robot". In: *Sixth International Symposium on Marine Engineering*. 2000, pp. 235–240.

[50] Thanhtam Ho and Sangyoon Lee. "A novel design of a robot that can jump and roll with a single actuator". In: *IEEE/RSJ Int. Conf. on Intelligent Robots and Systems*. 2012, pp. 908–913. DOI: 10.1109/IROS.2012.6385500.

[51] Benjamin J. Hockman, Andreas Frick, Robert G. Reid, Issa A. D. Nesnas, and Marco Pavone. "Design, control, and experimentation of internally-actuated rovers for the exploration of low-gravity planetary bodies". In: *J. Field Robot.* 34.1 (2017), pp. 5–24. DOI: 10.1002/rob.21656.

[52] Katie L. Hoffman and Robert J. Wood. "Myriapod-like ambulation of a segmented microrobot". In: *Auton. Robot.* 31.1 (2011), pp. 103–114. DOI: 10.1007/s10514-011-9233-4.

[53] Katie L. Hoffman and Robert J. Wood. "Turning gaits and optimal undulatory gaits for a modular centipede-inspired millirobot". In: *IEEE/RAS-EMBS Int. Conf. on Biomedical Robotics and Biomechatronics*. 2012, pp. 1052–1059. DOI: 10.1109/BioRob.2012.6290288.

[54] Aaron M. Hoover, Samuel Burden, Xiao-Yu Fu, S. Shankar Sastry, and Ronald S. Fearing. "Bio-inspired design and dynamic maneuverability of a minimally actuated six-legged robot". In: *IEEE/RAS-EMBS Int. Conf. on Biomedical Robotics and Biomechatronics*. 2010, pp. 869–876. DOI: 10.1109/BIOROB.2010.5626034.

[55] Aaron M. Hoover and Ronald S. Fearing. "Analysis of off-axis performance of compliant mechanisms with applications to mobile millirobot design". In: *IEEE/RSJ Int. Conf. on Intelligent Robots and Systems*. 2009, pp. 2770–2776. DOI: 10.1109/IROS.2009.5354374.

[56] Aaron M. Hoover and Ronald S. Fearing. "Fast scale prototyping for folded millirobots". In: *IEEE Int. Conf. on Robotics and Automation*. 2008, pp. 886–892. DOI: 10.1109/ROBOT.2008.4543317.

[57] Aaron M. Hoover, Erik Steltz, and Ronald S. Fearing. "RoACH: An autonomous 2.4g crawling hexapod robot". In: *IEEE/RSJ Int. Conf. on Intelligent Robots and Systems*. 2008, pp. 26–33. DOI: 10.1109/IROS.2008.4651149.

[58] Tomislav Horvat, Kamilo Melo, and Auke J. Ijspeert. "Spine controller for a sprawling posture robot". In: *IEEE Robot. Autom. Lett.* 2.2 (2017), pp. 1195–1202. DOI: 10.1109/LRA.2017.2664898.

[59] R. N. Hughes. "Essential involvement of specific legs in turn alternation of the woodlouse, Porcellio scaber". In: *Comp. Biochem. Physiol.* 93A.2 (1989), pp. 493–497. DOI: 10.1016/0300-9629(89)90073-X.

[60] Marco Hutter, Christian Gehring, Andreas Lauber, F. Gunther, Carmine D. Bellicoso, Vassilios Tsounis, Péter Fankhauser, Remo Diethelm, Samuel Bachmann, Michael Blösch, et al. "ANYmal–Toward legged robots for harsh environments". In: *Advanced Robotics* 31.17 (2017), pp. 918–931. DOI: 10.1080/01691864.2017.1378591.

[61] Kaushik Jayaram and Robert J. Full. "Cockroaches traverse crevices, crawl rapidly in confined spaces, and inspire a soft, legged robot". In: *Proceedings of the National Academy of Sciences* 113.8 (2016), E950–E957. DOI: 10.1073/pnas.1514591113.

[62] Kaushik Jayaram, Jean-Michel Mongeau, Anand Mohapatra, Paul Birkmeyer, Ronald S. Fearing, and Robert J. Full. "Transition by head-on collision: Mechanically mediated manoeuvres in cockroaches and small robots". In: *J. R. Soc. Interface* 15.139 (2018), p. 20170664. DOI: 10.1098/rsif.2017.0664.

[63] Devin L. Jindrich and Robert J. Full. "Many-legged maneuverability: Dynamics of turning in hexapods". In: *J. Exp. Biol.* 202.12 (1999), pp. 1603–1623. URL: http://jeb.biologists.org/content/jexbio/202/12/1603.full.pdf.

[64] Devin L. Jindrich, Nicola C. Smith, Karin Jespers, and Alan M. Wilson. "Mechanics of cutting maneuvers by ostriches (Struthio camelus)". In: *J. Exp. Biol.* 210.8 (2007), pp. 1378–1390. DOI: 10.1242/jeb.001545.

[65] Gwang-Pil Jung, Carlos S. Casarez, Sun-Pill Jung, Ronald S. Fearing, and Kyu-Jin Cho. "An integrated jumping-crawling robot using height-adjustable jumping module". In: *IEEE Int. Conf. on Robotics and Automation*. 2016, pp. 4680–4685. DOI: 10.1109/ICRA.2016.7487668.

[66] Ardian Jusufi, Daniel I. Goldman, Shai Revzen, and Robert J. Full. "Active tails enhance arboreal acrobatics in geckos". In: *Proceedings of the National Academy of Sciences* 105.11 (2008), pp. 4215–4219. DOI: 10.1073/pnas.0711944105.

[67] Ardian Jusufi, Daniel T. Kawano, Thomas Libby, and Robert J. Full. "Righting and turning in mid-air using appendage inertia: Reptile tails, analytical models and bio-inspired robots". In: *Bioinspir. Biomim.* 5.4 (2010), p. 045001. DOI: 10.1088/1748-3182/5/4/045001.

[68] T. R. Kane and M. P. Scher. "A dynamical explanation of the falling cat phenomenon". In: *Int. J. Solids Structures* 5.7 (1969), pp. 663–670. DOI: 10.1016/0020-7683(69)90086-9.

[69] Konstantinos Karakasiliotis, Robin Thandiackal, Kamilo Melo, Tomislav Horvat, Navid K. Mahabadi, Stanislav Tsitkov, Jean-Marie Cabelguen, and Auke J. Ijspeert. "From cineradiography to biorobots: An approach for designing robots to emulate and study animal locomotion". In: *J. R. Soc. Interface* 13.119 (2016), p. 20151089. DOI: 10.1098/rsif.2015.1089.

[70] Jaakko T. Karras, Christine L. Fuller, Kalind C. Carpenter, Alessandro Buscicchio, Dale McKeeby, Christopher J. Norman, Carolyn E. Parcheta, Ivan Davydychev, and Ronald S. Fearing. "Pop-up mars rover with textile-enhanced rigid-flex PCB body". In: *IEEE Int. Conf. on Robotics and Automation*. 2017, pp. 5459–5466. DOI: 10.1109/ICRA.2017.7989642.

[71] Katherine Karwoski. *Quadrocopter Control Design and Flight Operation*. Tech. rep. M11-0980. NASA Marshall Space Flight Center, 2011. URL: https://ntrs.nasa.gov/archive/nasa/casi.ntrs.nasa.gov/20110015820.pdf.

[72] Chad C. Kessens, Craig T. Lennon, and Jason Collins. "A metric for self-rightability and understanding its relationship to simple morphologies". In: *IEEE/RSJ Int. Conf. on Intelligent Robots and Systems*. 2014, pp. 3699–3704. DOI: 10.1109/IROS.2014.6943081.

[73] Chad C. Kessens, Daniel C. Smith, and Philip R. Osteen. "A framework for autonomous self-righting of a generic robot on sloped planar surfaces". In: *IEEE Int. Conf. on Robotics and Automation*. 2012, pp. 4724–4729. DOI: 10.1109/ICRA.2012.6224770.

[74] HyunGyu Kim, Kyungmin Jeong, Metin Sitti, and TaeWon Seo. "Steering control of a water-running robot using an active tail". In: *IEEE/RSJ Int. Conf. on Intelligent Robots and Systems*. 2016, pp. 4945–4950. DOI: 10.1109/IROS.2016.7759726.

[75] HyunGyu Kim, DongGyu Lee, and TaeWon Seo. "Rolling stability enhancement via balancing tail for a water-running robot". In: *J. Bionic Eng.* 12.3 (2015), pp. 395–405. DOI: 10.1016/S1672-6529(14)60131-1.

[76] Sangbae Kim, Jonathan E. Clark, and Mark R. Cutkosky. "iSprawl: Design and tuning for high-speed autonomous open-loop running". In: *Int. J. Robot. Res.* 25.9 (2006), pp. 903–912. DOI: 10.1177/0278364906069150.

[77] Sangbae Kim, Matthew Spenko, Salomon Trujillo, Barrett Heyneman, Daniel Santos, and Mark R. Cutkosky. "Smooth vertical surface climbing with directional adhesion". In: *IEEE Trans. Robot.* 24.1 (2008), pp. 65–74. DOI: 10.1109/TRO.2007.909786.

[78] Adam Klaptocz, Adrien Briod, Ludovic Daler, Jean-Christophe Zufferey, and Dario Floreano. "Euler spring collision protection for flying robots". In: *IEEE/RSJ Int. Conf. on Intelligent Robots and Systems*. 2013, pp. 1886–1892. DOI: 10.1109/IROS.2013.6696606.

[79] Adam Klaptocz, Ludovic Daler, Adrien Briod, Jean-Christophe Zufferey, and Dario Floreano. "An active uprighting mechanism for flying robots". In: *IEEE Trans. Robot.* 28.5 (2012), pp. 1152–1157. DOI: 10.1109/TRO.2012.2201309.

[80] Matthew A. Klein, Alexander S. Boxerbaum, Roger D. Quinn, Richard Harkins, and Ravi Vaidyanathan. "SeaDog: A rugged mobile robot for surf-zone applications". In: *IEEE/RAS-EMBS Int. Conf. on Biomedical Robotics and Biomechatronics*. 2012, pp. 1335–1340. DOI: 10.1109/BioRob.2012.6290759.

[81] Nicholas J. Kohut, Aaron M. Hoover, Kevin Y. Ma, Stanley S. Baek, and Ronald S. Fearing. "MEDIC: A legged millirobot utilizing novel obstacle traversal". In: *IEEE Int. Conf. on Robotics and Automation*. 2011, pp. 802–808. DOI: 10.1109/ICRA.2011.5980360.

[82] Nicholas J. Kohut, Andrew O. Pullin, Duncan W. Haldane, David Zarrouk, and Ronald S. Fearing. "Precise dynamic turning of a 10 cm legged robot on a low friction surface using a tail". In: *IEEE Int. Conf. on Robotics and Automation*. 2013, pp. 3299–3306. DOI: 10.1109/ICRA.2013.6631037.

[83] Nicholas J. Kohut, David Zarrouk, Kevin C. Peterson, and Ronald S. Fearing. "Aerodynamic steering of a 10 cm high-speed running robot". In: *IEEE/RSJ Int. Conf. on Intelligent Robots and Systems*. 2013, pp. 5593–5599. DOI: 10.1109/IROS.2013.6697167.

[84] Mirko Kovač, Manuel Schlegel, Jean-Christophe Zufferey, and Dario Floreano. "A miniature jumping robot with self-recovery capabilities". In: *IEEE/RSJ Int. Conf. on Intelligent Robots and Systems*. 2009, pp. 583–588. DOI: 10.1109/IROS.2009.5354005.

[85] Mirko Kovač, Manuel Schlegel, Jean-Christophe Zufferey, and Dario Floreano. "Steerable miniature jumping robot". In: *Auton. Robot.* 28.3 (2010), pp. 295–306. DOI: 10.1007/s10514-009-9173-4.

[86] David J. Kriegman. "Let them fall where they may: Capture regions of curved objects and polyhedra". In: *Int. J. Robot. Res.* 16.4 (1997), pp. 448–472. DOI: 10.1177/027836499701600402.

[87] Gregory Krummel, Krishnanand N. Kaipa, and Satyandra K. Gupta. "A horseshoe crab inspired surf zone robot with righting capabilities". In: *ASME International Design Engineering Technical Conferences and Computers and Information in Engineering Conference*. 2014, V05AT08A010. DOI: 10.1115/DETC2014-34679.

[88] Bokeon Kwak and Joonbum Bae. "Design and analysis of a rotational leg-type miniature robot with an actuated middle joint and a tail (RoMiRAMT-II)". In: *J. Bionic Eng.* 15.2 (2018), pp. 356–367. DOI: 10.1007/s42235-018-0027-7.

[89] Daisy Lachat, Alessandro Crespi, and Auke Jan Ijspeert. "BoxyBot: A swimming and crawling fish robot controlled by a central pattern generator". In: *IEEE/RAS-EMBS Int. Conf. on Biomedical Robotics and Biomechatronics*. 2006, pp. 643–648. DOI: 10.1109/BIOROB.2006.1639162.

[90] Chen Li, Chad C. Kessens, Ronald S. Fearing, and Robert J. Full. "Mechanical principles of dynamic terrestrial self-righting using wings". In: *Advanced Robotics* 31.17 (2017), pp. 881–900. DOI: 10.1080/01691864.2017.1372213.

[91] Chen Li, Andrew O. Pullin, Duncan W. Haldane, Han K. Lam, Ronald S. Fearing, and Robert J. Full. "Terradynamically streamlined shapes in animals and robots enhance traversability through densely cluttered terrain". In: *Bioinspir. Biomim.* 10.4 (2015), p. 046003. DOI: 10.1088/1748-3190/10/4/046003.

[92] Chen Li, Tingnan Zhang, and Daniel I. Goldman. "A terradynamics of legged locomotion on granular media". In: *Science* 339.6126 (2013), pp. 1408–1412. DOI: 10.1126/science.1229163.

[93] Thomas Libby, Aaron M. Johnson, Evan Chang-Siu, Robert J. Full, and Daniel E. Koditschek. "Comparative design, scaling, and control of appendages for inertial reorientation". In: *IEEE Trans. Robot.* 32.6 (2016), pp. 1380–1398. DOI: 10.1109/TRO.2016.2597316.

[94] Thomas Libby, Talia Y. Moore, Evan Chang-Siu, Deborah Li, Daniel J. Cohen, Ardian Jusufi, and Robert J. Full. "Tail-assisted pitch control in lizards, robots and dinosaurs". In: *Nature* 481.7380 (2012), pp. 181–184. DOI: 10.1038/nature10710.

[95] Guan-Horng Liu, Hou-Yi Lin, Huai-Yu Lin, Shao-Tuan Chen, and Pei-Chun Lin. "A bio-inspired hopping kangaroo robot with an active tail". In: *J. Bionic Eng.* 11.4 (2014), pp. 541–555. DOI: 10.1016/S1672-6529(14)60066-4.

[96] Kevin Y. Ma, Pakpong Chirarattananon, Sawyer B. Fuller, and Robert J. Wood. "Controlled flight of a biologically inspired, insect-scale robot". In: *Science* 340.6132 (2013), pp. 603–607. DOI: 10.1126/science.1231806.

[97] Arthur Joseph McClung. "Techniques for dynamic maneuvering of hexapedal legged robots". PhD thesis. Stanford University, 2006.

[98] Benjamin McInroe, Henry C. Astley, Chaohui Gong, Sandy M. Kawano, Perrin E. Schiebel, Jennifer M. Rieser, Howie Choset, Richard W. Blob, and Daniel I. Goldman. "Tail use improves performance on soft substrates in models of early vertebrate land locomotors". In: *Science* 353.6295 (2016), pp. 154–158. DOI: 10.1126/science.aaf0984.

[99] Jeremy M. Morrey, Bram Lambrecht, Andrew D. Horchler, Roy E. Ritzmann, and Roger D. Quinn. "Highly mobile and robust small quadruped robots". In: *IEEE/RSJ Int. Conf. on Intelligent Robots and Systems*. Vol. 1. 2003, pp. 82–87. DOI: 10.1109/IROS.2003.1250609.

[100] Scott Morton and Nikolaos Papanikolopoulos. "A small hybrid ground-air vehicle concept". In: *IEEE/RSJ Int. Conf. on Intelligent Robots and Systems*. 2017, pp. 5149–5154. DOI: 10.1109/IROS.2017.8206402.

[101] Michael P. Murphy, Casey Kute, Yiğit Mengüç, and Metin Sitti. "Waalbot II: Adhesion recovery and improved performance of a climbing robot using fibrillar adhesives". In: *The International Journal of Robotics Research* 30.1 (2011), pp. 118–133. DOI: 10.1177/0278364910382862.

[102] Chenghui Nie, Simo Cusi Van Dooren, Jainam Shah, and Matthew Spenko. "Execution of dynamic maneuvers for unmanned ground vehicles using variable internal inertial properties". In: *IEEE/RSJ Int. Conf. on Intelligent Robots and Systems*. 2009, pp. 4226–4231. DOI: 10.1109/IROS.2009.5354033.

[103] Shawn M. O'Connor, Terence J. Dawson, Rodger Kram, and J. Maxwell Donelan. "The kangaroo's tail propels and powers pentapedal locomotion". In: *Biol. Lett.* 10.7 (2014), p. 20140381. DOI: 10.1098/rsbl.2014.0381.

[104] Daniel O'Halloran, Alon Wolf, and Howie Choset. "Design of a high-impact survivable robot". In: *Mech. Mach. Theory* 40.12 (2005), pp. 1345–1366. DOI: 10.1016/j.mechmachtheory.2005.02.004.

[105] Cagdas D. Onal, Michael T. Tolley, Robert J. Wood, and Daniela Rus. "Origami-inspired printed robots". In: *IEEE/ASME Trans. Mechatronics* 20.5 (2015), pp. 2214–2221. DOI: 10.1109/TMECH.2014.2369854.

[106] Didier Papadopoulos and Martin Buehler. "Stable running in a quadruped robot with compliant legs". In: *IEEE Int. Conf. on Robotics and Automation*. 2000, pp. 444–449. DOI: 10.1109/ROBOT.2000.844095.

[107] Hae-Won Park, Patrick M. Wensing, and Sangbae Kim. "High-speed bounding with the MIT Cheetah 2: Control design and experiments". In: *Int. J. Robot. Res.* 36.2 (2017), pp. 167–192. DOI: 10.1177/0278364917694244.

[108] Amir Patel and Martin Braae. "Rapid turning at high-speed: Inspirations from the cheetah's tail". In: *IEEE/RSJ Int. Conf. on Intelligent Robots and Systems*. 2013, pp. 5506–5511. DOI: 10.1109/IROS.2013.6697154.

[109] Saijin Peng, Xilun Ding, Fan Yang, and Kun Xu. "Motion planning and implementation for the self-recovery of an overturned multi-legged robot". In: *Robotica* 35.5 (2017), pp. 1107–1120. DOI: 10.1017/S0263574715001009.

[110] Kevin Peterson and Ronald S. Fearing. "Experimental dynamics of wing assisted running for a bipedal ornithopter". In: *IEEE/RSJ Int. Conf. on Intelligent Robots and Systems*. 2011, pp. 5080–5086. DOI: 10.1109/IROS.2011.6095041.

[111] *Plastic Materials Index*. URL: http://precisionpunch.com/plastic-materials-index (visited on 08/01/2018).

[112] Andrew O. Pullin, Nicholas J. Kohut, David Zarrouk, and Ronald S. Fearing. "Dynamic turning of 13 cm robot comparing tail and differential drive". In: *IEEE Int. Conf. on Robotics and Automation*. 2012, pp. 5086–5093. DOI: 10.1109/ICRA.2012.6225261.

[113] Marc Raibert, Kevin Blankespoor, Gabriel Nelson, and Rob Playter. "BigDog, the rough-terrain quadruped robot". In: *IFAC Proceedings Volumes* 41.2 (2008), pp. 10822–10825. DOI: 10.3182/20080706-5-KR-1001.01833.

[114] Cameron J. Rose, Parsa Mahmoudieh, and Ronald S. Fearing. "Coordinated launching of an ornithopter with a hexapedal robot". In: *IEEE Int. Conf. on Robotics and Automation*. 2015, pp. 4029–4035. DOI: 10.1109/ICRA.2015.7139762.

[115] Uluc Saranli, Martin Buehler, and Daniel E. Koditschek. "RHex: A simple and highly mobile hexapod robot". In: *Int. J. Robot. Res.* 20.7 (2001), pp. 616–631. DOI: 10.1177/02783640122067570.

[116] Uluc Saranli, Alfred A. Rizzi, and Daniel E. Koditschek. "Model-based dynamic self-righting maneuvers for a hexapedal robot". In: *Int. J. Robot. Res.* 23.9 (2004), pp. 903–918. DOI: 10.1177/0278364904045594.

[117] Daniel Schmitt, Michael D. Rose, Jean E. Turnquist, and Pierre Lemelin. "Role of the prehensile tail during ateline locomotion: Experimental and osteological evidence". In: *Am. J. Phys. Anthropol.* 126.4 (2005), pp. 435–446. DOI: 10.1002/ajpa.20075.

[118] John Schmitt and Philip Holmes. "Mechanical models for insect locomotion: Dynamics and stability in the horizontal plane–II. Application". In: *Biol. Cyber.* 83.6 (2000), pp. 517–527. DOI: 10.1007/s004220000180.

[119] Claudio Semini, Victor Barasuol, Jake Goldsmith, Marco Frigerio, Michele Focchi, Yifu Gao, and Darwin G. Caldwell. "Design of the hydraulically actuated, torque-controlled quadruped robot HyQ2Max". In: *IEEE/ASME Trans. Mechatronics* 22.2 (2017), pp. 635–646. DOI: 10.1109/TMECH.2016.2616284.

[120] TaeWon Seo, Carlos S. Casarez, and Ronald S. Fearing. "High-rate controlled turning with a pair of miniature legged robots". In: *IEEE Int. Conf. on Robotics and Automation*. 2017, pp. 5962–5968. DOI: 10.1109/ICRA.2017.7989703.

[121] TaeWon Seo and Metin Sitti. "Tank-like module-based climbing robot using passive compliant joints". In: *IEEE/ASME Trans. Mechatronics* 18.1 (2013), pp. 397–408. DOI: 10.1109/TMECH.2011.2182617.

[122] Matthew J. Spenko, Galen C. Haynes, J. A. Saunders, Mark R. Cutkosky, Alfred A. Rizzi, Robert J. Full, and Daniel E. Koditschek. "Biologically inspired climbing with a hexapedal robot". In: *J. Field Robot.* 25.2008 (2008), pp. 223–242. DOI: 10.1002/rob.20238.

[123] *SpotMini — Boston Dynamics*. URL: https://www.bostondynamics.com/spot-mini (visited on 08/01/2018).

[124] Pratheev S. Sreetharan, John P. Whitney, Mark D. Strauss, and Robert J. Wood. "Monolithic fabrication of millimeter-scale machines". In: *J. Micromech. Microeng.* 22.5 (2012), p. 055027. DOI: 10.1088/0960-1317/22/5/055027.

[125] Sascha A. Stoeter, Ian T. Burt, and Nikolaos Papanikolopoulos. "Scout robot motion model". In: *IEEE Int. Conf. on Robotics and Automation*. 2003, pp. 90–95. DOI: 10.1109/ROBOT.2003.1241578.

[126] R. Strauss and M. Heisenberg. "Coordination of legs during straight walking and turning in Drosophila melanogaster". In: *J. Comp. Physiol. A* 167.3 (1990), pp. 403–412. DOI: 10.1007/BF00192575.

[127] Yuuta Sugiyama and Shinichi Hirai. "Crawling and jumping by a deformable robot". In: *Int. J. Robot. Res.* 25.5–6 (2006), pp. 603–620. DOI: 10.1177/0278364906065386.

[128] Kensuke Takita, Toshio Katayama, and Shigeo Hirose. "The efficacy of the neck and tail of miniature dinosaur-like robot TITRUS-III". In: *IEEE/RSJ Int. Conf. on Intelligent Robots and Systems*. 2002, pp. 2593–2598. DOI: 10.1109/IRDS.2002.1041661.

[129] Ning Tan, Rajesh Elara Mohan, and Karthikeyan Elangovan. "A bio-inspired reconfigurable robot". In: *Advances in Reconfigurable Mechanisms and Robots II*. Mechanisms and Machine Science. Springer, 2016, pp. 483–493. DOI: 10.1007/978-3-319-23327-7_42.

[130] Michael T. Tolley, Robert F. Shepherd, Michael Karpelson, Nicholas W. Bartlett, Kevin C. Galloway, Michael Wehner, Rui Nunes, George M. Whitesides, and Robert J. Wood. "An untethered jumping soft robot". In: *IEEE/RSJ Int. Conf. on Intelligent Robots and Systems*. 2014, pp. 561–566. DOI: 10.1109/IROS.2014.6942615.

[131] Katsuyoshi Tsujita, Hiroomi Toui, and Kazuo Tsuchiya. "Dynamic turning control of a quadruped locomotion robot using oscillators". In: *Adv. Robotics* 19.10 (2005), pp. 1115–1133. DOI: 10.1163/156855305774662208.

[132] Hideyuki Tsukagoshi, Masashi Sasaki, Ato Kitagawa, and Takahiro Tanaka. "Design of a higher jumping rescue robot with the optimized pneumatic drive". In: *IEEE Int. Conf. on Robotics and Automation*. 2005, pp. 1276–1283. DOI: 10.1109/ROBOT.2005.1570291.

[133] Rebecca M. Walter. "Kinematics of 90° running turns in wild mice". In: *J. Exp. Biol.* 206.10 (2003), pp. 1739–1749. DOI: 10.1242/jeb.00349.

[134] Chen Wang, Meyer Nahon, and Mike Trentini. "Controller development and validation for a small quadrotor with compensation for model variation". In: *International Conference on Unmanned Aircraft Systems*. 2014, pp. 902–909. DOI: 10.1109/ICUAS.2014.6842339.

[135] Xin Wang, Mantian Li, Pengfei Wang, and Lining Sun. "Running and turning control of a quadruped robot with compliant legs in bounding gait". In: *IEEE Int. Conf. on Robotics and Automation*. 2011, pp. 511–518. DOI: 10.1109/ICRA.2011.5979619.

[136] Zhirong Wang, Erbao Dong, Min Xu, and Jie Yang. "Circling turning locomotion of a new multiple closed-chain-legs robot with hybrid-driven mechanism". In: *Adv. Robotics* 29.24 (2015), pp. 1637–1648. DOI: 10.1080/01691864.2015.1071682.

[137] John P. Whitney, Pratheev S. Sreetharan, Kevin Y. Ma, and Robert J. Wood. "Pop-up book MEMS". In: *J. Micromech. Microeng.* 21.11 (2011), p. 115021. DOI: 10.1088/0960-1317/21/11/115021.

[138] Jeffrey S. Willey, Audrone R. Biknevicius, Stephen M. Reilly, and Kathleen D. Earls. "The tale of the tail: Limb function and locomotor mechanics in Alligator mississippiensis". In: *J. Exp. Biol.* 207.3 (2004), pp. 553–563. DOI: 10.1242/jeb.00774.

[139] Robert J. Wood, Srinath Avadhanula, Manas Menon, and Ronald S. Fearing. "Microrobotics using composite materials: The micromechanical flying insect thorax". In: *IEEE Int. Conf. on Robotics and Automation*. 2003, pp. 1842–1849. DOI: 10.1109/ROBOT.2003.1241863.

[140] Robert J. Wood, Srinath Avadhanula, Ranjana Sahai, Erik Steltz, and Ronald S. Fearing. "Microrobot design using fiber reinforced composites". In: *J. Mech. Des.* 130.5 (2008), p. 052304. DOI: 10.1115/1.2885509.

[141] Kazuo Yamafuji, Tsuyoshi Kobayashi, and Takashi Kawamura. "Elucidation of twisting motion of a falling cat and its realization by a robot". In: *Journal of the Robotics Society of Japan* 10.5 (1992), pp. 648–654. DOI: 10.7210/jrsj.10.648.

[142] Dongwon Yun and Ronald S. Fearing. "VLR: Cockroach millirobot with load decoupling structure". In: *IEEE Int. Conf. on Advanced Intelligent Mechatronics*. 2015, pp. 127–132. DOI: 10.1109/AIM.2015.7222520.

[143] David Zarrouk and Ronald S. Fearing. "Controlled in-plane locomotion of a hexapod using a single actuator". In: *IEEE Trans. Robot.* 31.1 (2015), pp. 157–167. DOI: 10.1109/TRO.2014.2382981.

[144] Garth John Zeglin. "Uniroo—a one legged dynamic hopping robot". B.S. thesis. Massachusetts Institute of Technology, 1991.

[145] Jun Zhang, Guangming Song, Yuya Li, Guifang Qiao, Aiguo Song, and Aimin Wang. "A bio-inspired jumping robot: Modeling, simulation, design, and experimental results". In: *Mechatronics* 23.8 (2013), pp. 1123–1140. DOI: 10.1016/j.mechatronics.2013.09.005.

[146] Jianguo Zhao, Tianyu Zhao, Ning Xi, Matt W. Mutka, and Li Xiao. "MSU tailbot: Controlling aerial maneuver of a miniature-tailed jumping robot". In: *IEEE/ASME Trans. Mechatronics* 20.6 (2015), pp. 2903–2914. DOI: 10.1109/TMECH.2015.2411513.

[147] Christoph Zollikofer. "Stepping patterns in ants–Influence of speed and curvature". In: *J. Exp. Biol.* 192.1 (1994), pp. 95–106. URL: http://jeb.biologists.org/content/jexbio/192/1/95.full.pdf.